SANDIA REPORT SAND83—2572 • Unlimited Release • UC—28
Printed September 1985

Predicted Flash X-Ray Environments Using Standard Converter Configurations

John A. Halbleib, Thomas W. L. Sanford

Prepared by
Sandia National Laboratories
Albuquerque, New Mexico 87185 and Livermore, California 94550
for the United States Department of Energy
under Contract DE-AC04-76DP00789

Issued by Sandia National Laboratories, operated for the United States Department of Energy by Sandia Corporation.

Printed in the United States of America
Available from
National Technical Information Service
U.S. Department of Commerce
5285 Port Royal Road
Springfield, VA 22161

NTIS price codes
Printed copy: A04
Microfiche copy: A01

SAND83-2572
Unlimited Release
Printed September 1985

Distribution
Category UC-28

Predicted Flash X-Ray Environments Using Standard Converter Configurations

John A. Halbleib
Simulation Theory Division

Thomas W. L. Sanford
Simulation Technology Division

Sandia National Laboratories
Albuquerque, NM 87185

Abstract

Using a sophisticated Monte Carlo model, we have obtained predictions of the forward radiation fields generated by a series of monoenergetic electron sources, with kinetic energies ranging from 0.5 to 15.0 MeV, normally incident on standard converter configurations. The tantalum converter foil thickness that maximizes the total forward-going x-ray energy ranges from 0.3 times the continuous-slowing-down-approximation electron range at 0.5 MeV to 0.6 times that range at 15.0 MeV. This result is not very sensitive to the presence or absence of typical electron absorbers or debris shields. The forward extraction efficiency exhibits a slightly superlinear dependence on source electron kinetic energy. Electron backscatter and photon absorption are shown to be the chief transport phenomena that limit x-ray extraction. Dependence of x-ray spectra on emission angle results from the complicated interplay of cross-section kinematics, slant-thickness absorption, and slant-thickness buildup. The response of common dosimetry materials to the radiation fields was also studied. The systematics of energy deposition in high-Z and low-Z dosimetry materials as a function of source energy, converter geometry, and emission angle are presented in terms of an effective absorption coefficient. The utility of this coefficient for predicting the energy deposition in one material from the measured dose in another material is demonstrated. It is shown that the converter thickness that optimizes dose is less than the thickness that optimizes the forward extraction efficiency.

Contents

Figures

Figures (Continued)

Tables

Predicted Flash X-Ray Environments Using Standard Converter Configurations

1. Introduction

High-intensity pulsed relativistic electron beams are used extensively to generate intense FXR (flash x-ray) sources by injecting these beams into standard converter configurations where they generate continuous x rays via bremsstrahlung production and line radiation via fluorescence radiation from ionizing interactions. Although the simulation of weapon radiation effects is by far the most prominent application, such sources are also used for radiography, x-ray cinematography, and pseudoholography. Despite this wide usage, there is no convenient reference that provides systematic information on thick-target bremsstrahlung environments.

Reference 1 was an early attempt to provide such information along with the direct electron environments. However, the usefulness of that information was limited for several reasons. First, an attempt was made to define a canonical shape for the spectrum of beam electrons from pulsed high-current sources. Experience has shown the futility of this assumption. Indeed, we often find it difficult to achieve repeatability of the spectrum from shot to shot on a given machine, much less machine-to-machine repeatability. Second, the converter configurations in Ref. 1 were not carefully optimized. Of particular importance is the thickness of the high-Z converter, which can have a substantial effect on the extraction efficiency, the x-ray spectrum, and the angular distribution of the x rays. Third, the x-ray deposition data in Ref. 1 are not particularly useful because they are low-resolution depth profiles in thick targets of infrequently used materials. The profiles are one-dimensional and no information is given on the off-axis variation.

In contrast to Ref. 1, we concentrate in this paper almost exclusively on FXR environments. Recognizing that there is no "typical" spectral shape for the source electrons, we restrict ourselves to monoenergetic sources of normally incident pencil beams of electrons. Our results are directly useful in design studies. When applied to real sources, however, interpolation is required. Furthermore, the high-Z converter used in the present study is carefully optimized for maximum extraction of x-ray energy. Our deposition predictions focus on frequently used detector materials and on the dependence of dose on the angle with respect to the beam axis.

In Sec. 2, we discuss the standard converter configuration. In Sec. 3, we give a brief description of the theoretical model. Systematic predictions for the radiation field in the forward direction are presented in Sec. 4. In Sec. 5 we discuss various aspects of the energy deposition predicted by the model. The results are summarized in Sec. 6.

2. Standard FXR Converter Configuration

The standard scheme by which a high-intensity pulse of relativistic electrons is converted into a flash x-ray source is shown in Fig. 1. Because the bremsstrahlung production cross sections increase approximately as Z^2 (Fig. 2), the electrons are injected into a high-Z foil where the bulk of the x rays are produced. This converter foil may also be the accelerator anode, or the beam may be extracted before injection. Because the foil thickness that maximizes x-ray extraction is less than the range of the beam electrons, the converter foil is usually followed by an electron absorber, which prevents electrons transmitted by the foil from preheating a debris shield (DS). The electron absorber is made of a low-Z material in order to minimize the absorption of photons generated in the converter foil; photon attenuation coefficients increase with atomic number at both low and high photon energies where they are dominated by the photoelectric and pair-production interactions, respectively. The debris shield is usually necessary for nondestructive testing because the high-power density of the electron beam can shatter, melt, or vaporize the converter foil and electron absorber thus producing forward-traveling debris at the site being irradiated. When destructive testing is acceptable, the debris shield is not necessary. The electron absorber, however, is usually still necessary in order to prevent electrons from reaching the exposure area.

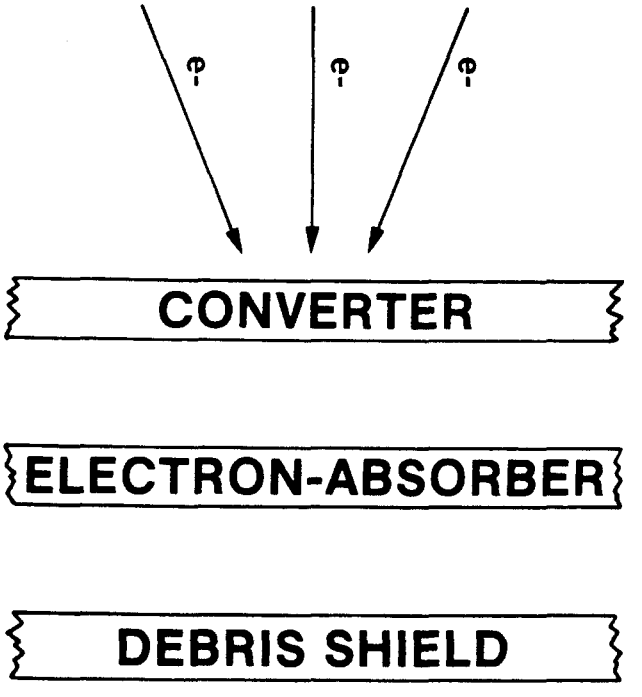

Figure 1. Schematic of a Standard Converter System

Essentially all of the x rays extracted in the forward 2π solid angle are available for experiments in the standard geometry. Certain loss mechanisms that limit the magnitude of the foward extraction efficiencies are discussed below. There are a number of "advanced" converter schemes that seek to overcome these losses. As yet, few of these schemes have enhanced the radiation environment sufficiently to justify their additional complexity. Consequently, standard configurations will continue to dominate the field in the near term, and therefore advanced configurations are not discussed in this report.

3. Theoretical Model

3.1 The TIGER Code

All results were obtained using a modified version of the one-dimensional coupled electron/photon Monte Carlo transport code, TIGER.[3] This code contains all the essential physics[4] for generating and transporting the complete electron/photon cascade until such time as these particles either are absorbed, escape from the system, or have their energies reduced below some user-defined cutoffs. Electron interactions include the production of knock-on electrons, bremsstrahlung, positron annihilation, and K-shell impact ionization. Photon interactions include photoionization, Compton scattering, and pair production. K-shell ionization is followed by the production of fluorescence photons or Auger electrons.

A standard output of the code is the photon energy transmission coefficient. This is equivalent to the forward extraction efficiency, the fraction of the incident electron beam energy that is extracted in the forward 2π solid angle in the form of photons. In addition, the code provides the energy distribution of the transmitted photons, the angular distribution of transmitted photons, and the coupled energy and angular distribution of the transmitted photons.

3.2 Code Modifications

A number of updates have been added to the basic code. Specifically, photon production is artificially increased by scaling the cross sections for the production of bremsstrahlung and K-shell impact ionization, enabling us to obtain statistically meaningful photon outputs without following an excessive number of source electrons. Electron tracking is expensive, and, in this way, it is only necessary to follow an adequate sample of electron trajectories. Adjusting the weights of the artificially high population of x rays insures that the predictions are unbiased.

Also, we have modified the code to generate distributions of the cumulative transmitted photon number and the cumulative transmitted photon energy. The distributions are the amounts of these quantities below a given photon energy as a function of that photon energy. They are useful because in many experiments the high energy component of the x-ray spectrum is of little interest.

An elaborate modification has been required in order to obtain dosimetry predictions. On the one hand, we have special techniques for obtaining efficient generation of x rays. On the other hand, we have special techniques for obtaining efficient Monte Carlo deposition from x rays. However, because the two techniques are not compatible, combining the calculation of x-ray production and x-ray dosimetry in a single Monte Carlo run is difficult. Our approach has been to concentrate on our interest in a particular kind of energy deposition. We are primarily interested in obtaining the kerma (kinetic energy released in material), or equilibrium dose, at depths for which the incident photon flux is neither appreciably attenuated nor appreciably augmented by the buildup of secondary photons. Under these conditions, a very good approximation to the dose is

$$D = \int_0^\infty h\nu\, \Phi(h\nu)\, \mu_a\,(h\nu)\, dh\nu \ , \tag{1}$$

where $h\nu$ is the photon energy in MeV, Φ is the photon flux at the detector position in units of number/(MeV-cm^2), and μ_a is the mass energy absorption coefficient for the particular detector material in cm^2/g.

We can obtain a very good estimate of this quantity *without including the detector in the Monte Carlo transport*. Each time a photon emerges from a collision in the configuration shown in the Fig. 1 heading in the direction of a detector, we score the quantity

$$\text{tally} = W \times \exp\left[-\sum_i \mu_i\,(h\nu)\, t_i\right] A^{-1} \times (\bar{\Omega} \cdot \bar{n})^{-1} \times h\nu \times \mu_a\,(h\nu) \ , \tag{2}$$

where W is the photon weight as it emerges from the collision, μ_i is the total attenuation coefficient for the ith material, t_i is the length of the extended trajectory through the ith material, the argument of the exponent is the optical pathlength from the collision point to the detector, A is the area of the detector in cm^2, $\overline{\Omega}$ is the unit vector of photon direction, and $\overline{n}$ is the unit normal to the detector surface at the point where the photon trajectory intersects that surface. The properly normalized sum of all such tallies is an excellent estimator of D in Eq. (1). This quantity is often called the uncollided surface-dose, but is actually more representative of the uncollided peak-dose which occurs just inside the surface where electron equilibrium is established. This approximation breaks down (a) when photon attenuation cannot be neglected, (b) when photon buildup cannot be neglected, (c) when the detector is so thin that electron equilibrium cannot be established, or (d) when the photon energy is so high that radiation loss of secondary electrons becomes important. The reader is referred to Ref. 5 for a more detailed discussion of mass-energy absorption coefficients and related quantities. Condition (a) can be accounted for by including the appropriate exponential attenuation factor in Eq. (1). Under any of the other three conditions, one has no choice but to carry out Monte Carlo transport in the detector itself. For the beam electron energies and detectors of interest here, Eq. (2) is a very good estimate of the dose.[6] The only quantity in Eq. (2) that is not available in the Monte Carlo code is the mass-energy absorption coefficient. Fortunately, the code used to generate the photon cross sections already contains the logic to calculate these coefficients. The appropriate coding was modified to ensure that these data were produced and properly transferred to the transport code.

From Eq. (1), we can define the effective mass-energy absorption coefficient, μ_{eff}, as[7]

$$\mu_{eff} = \frac{D}{F} , \tag{3}$$

where F, the energy fluence, is given by

$$F = \int_0^\infty h\nu \, \Phi \, (h\nu) \, dh\nu \ . \tag{4}$$

In other words, the same fluence of monenergetic photons for which the absorption coefficient is equal to μ_{eff} would result in the same dose. Because the energy fluence is independent of dosimetry material, a discussion of effective mass-energy absorption coefficients is equivalent to a discussion of relative doses. Of course, absolute doses require a knowledge of the fluence as well. Equation (2) without the factor μ_a ($h\nu$) is used in the Monte Carlo code to provide an estimator for the energy fluence.

4. Radiation Field

In this section, we discuss model predictions of the radiation field, and how the energy and angular distributions of these fields depend on the source-electron kinetic energy and converter configuration. We consider source-electron kinetic energies of 0.5, 1.0, 2.0, 5.0, 10.0, and 15.0 MeV. This set adequately covers the range of high-intensity FXR sources now in operation or planned for the near future. In all calculations the photons were followed until their energy dropped below 0.01 MeV, and all electrons and positrons were followed until their energy fell below 5% of the source energy.

4.1 Optimization and Efficiency

From a theoretical point of view, the most logical way to optimize an FXR source for a broad range of applications is to maximize the forward-extracted x-ray energy; However, this quantity is not directly measureable. From a practical point of view, optimization is most likely to take the form of maximizing the on-axis dose to some selected dosimeter. As we shall see in Sec. 5, this optimization does depend somewhat on the choice of detector. One would choose a detector that responds in a manner similar to that of the proposed experiment or, better still, one would maximize the experimental response itself. The latter is rarely done. Fortunately, in most cases optimization is not sensitive to which of these methods is selected. Here we use the forward-extracted x-ray energy to optimize the converter configuration.

The essential element of all converter systems is the high-Z foil in the converter itself. Because of the high beam intensities, this foil is almost always made from a refractory material like tantalum. A large fraction of the beam energy is also dissipated in the low-Z electron absorber. The most commonly used absorber is some form of graphite. Its thickness need be no greater than that which, when combined with the tantalum, equals the range of the most energetic source electrons. Any greater amount only absorbs x rays while serving no other purpose. The thickness of the debris shield depends on the beam intensity of any given machine.

In our optimization studies, we considered three configurations: (a) tantalum foil alone (Ta), (b) tantalum foil plus graphite absorber (Ta/C), and (c) tantalum foil plus graphite absorber plus debris shield (Ta/C/DS). In each case, we calculated the forward 2π extraction efficiency—the percent of the incident electron beam energy emitted from the transmission side of the converter configuration in the form of photons—as a function of the tantalum thickness. In all calculations with an electron absorber present, the graphite thickness was simultaneously adjusted so that the combined tantalum and graphite thicknesses were equal to one continuous-slowing-down-approximation (CSDA) range, r_o, of the source electrons. For debris shields, we have chosen an areal density of graphite equivalent to that of debris shields that have been used on machines having nominal energies close to our monoenergetic values. These machines typically generate tens of kilojoules of electron beam energy that is spread over areas of tens of square centimeters. The CSDA ranges and debris shields used in the calculations are given in Table 1.

The CSDA range is the integral of the reciprocal of the total stopping power from the given energy down to thermal energy. For low electron energies, the collisional stopping power dominates over radiation loss. As electron energy increases, the radiative stopping power becomes more and more important. At 11.5 MeV, the radiative and collisional stopping powers are about equal in Ta, while at 15.0 MeV the radiative stopping power is still only about 15% of the collisional stopping power in graphite. At 15.0 MeV the ranges in the two materials are about equal.

Table 1. Electron CSDA Ranges and Debris Shield Thicknesses for Each Source Electron Kinetic Energy Used in the Calculation

Electron Kinetic Energy (MeV)	CSDA Ranges (g/cm^2)		Thickness of Graphite Debris Shield (cm)
	Ta†	C††	
0.5	0.3254	0.1971	0.2915
1.0	0.7630	0.4891	0.2915
2.0	1.599	1.098	0.4286
5.0	3.667	2.862	0.4286
10.0	6.203	5.593	0.8573
15.0	8.106	8.136	0.8573

†Mass density of 16.6 g/cm^3
††Mass density of 2.00 g/cm^3

In Figs. 2a through 2f, we have plotted the efficiencies as a function of the thickness of the tantalum foil expressed in units of r_0 for all three configurations. The SD (statistical standard deviation) of the calculated values is 1% to 2%. The symbols are the actual calculated values, and spline interpolants have been drawn through these points. The waviness of some of these interpolants is caused by statistical uncertainties; we expect no inflection points in the true differential curves. Note that the uncertainties tend to be magnified by the narrow range of ordinate values.

There are some interesting effects that are not easily understood. The smallest differences in the three configurations is at 0.5 MeV, where the Ta/C results are slightly larger than the Ta results. As the source-electron kinetic energy increases, the continuous x-ray spectrum changes, along with the proportion of that spectrum to the line radiation and the filtering of both types by the elements of the converter system. Clearly, the Ta curve must eventually fall below the other two as the foil thickness is reduced because this curve goes to zero for zero thickness, while the other two become more and more dominated by x-ray production in graphite. The maximum difference in the three configurations near peak extraction is about 20%. These data are replotted on a single graph in Fig. 3 to emphasize the increase in optimum converter foil thickness with increasing source energy. Note also that the maxima are very broad so that experimentally one can be sloppy in the choice of foil thickness.

From the results in Figs. 2 and 3, we determine the optimum thicknesses of the Ta foil for the three configurations. In r_0 units, these are 0.3 for 0.5, 1.0, and 2.0 MeV; 0.5 for 5.0 MeV; and either 0.5 or 0.6 for 10.0 and 15.0 MeV. All results in the remainder of this section will be for these optima.

One of the important concerns for FXR designers is the dependence of the forward extraction efficiency on source-electron kinetic energy. This efficiency is plotted in Fig. 4. The efficiency is very slightly superlinear over this energy range. We emphasize that these data are given as percents of beam energy. This point is important. If an increase in accelerator voltage can only be achieved at a significant penalty in beam energy (e.g., by increasing the mismatch between the impedances of a diode and a transmission line), there may be no increase in the resulting extracted x-ray energy.

The continuous x-ray spectrum is always accompanied by line (characteristic) radiation. The most important line radiation is the flourescence radiation from the impact ionization and photoionization of the K-shell of the atoms of the high-Z foil. This radiation is especially important at low electron energies and can lead to significant effects in high-Z dosimetry.[8] The average K-fluorescent energy of tantalum is just under 59 keV.[9] The magnitude of this x-ray component is plotted in Fig. 5 as a function of source-electron kinetic energy for the Ta/C configuration. It is given as a percent of both the forward-extracted x-ray energy and the electron beam energy. The estimated SD's are 1 to 4%. Both quantities are a strong function of the kinetic energy of the source electrons. At 0.5 MeV, almost 10% of the extracted x-ray energy is line radiation, whereas at 3.0 MeV, the line radiation is less than 1% of the extracted x-ray energy.

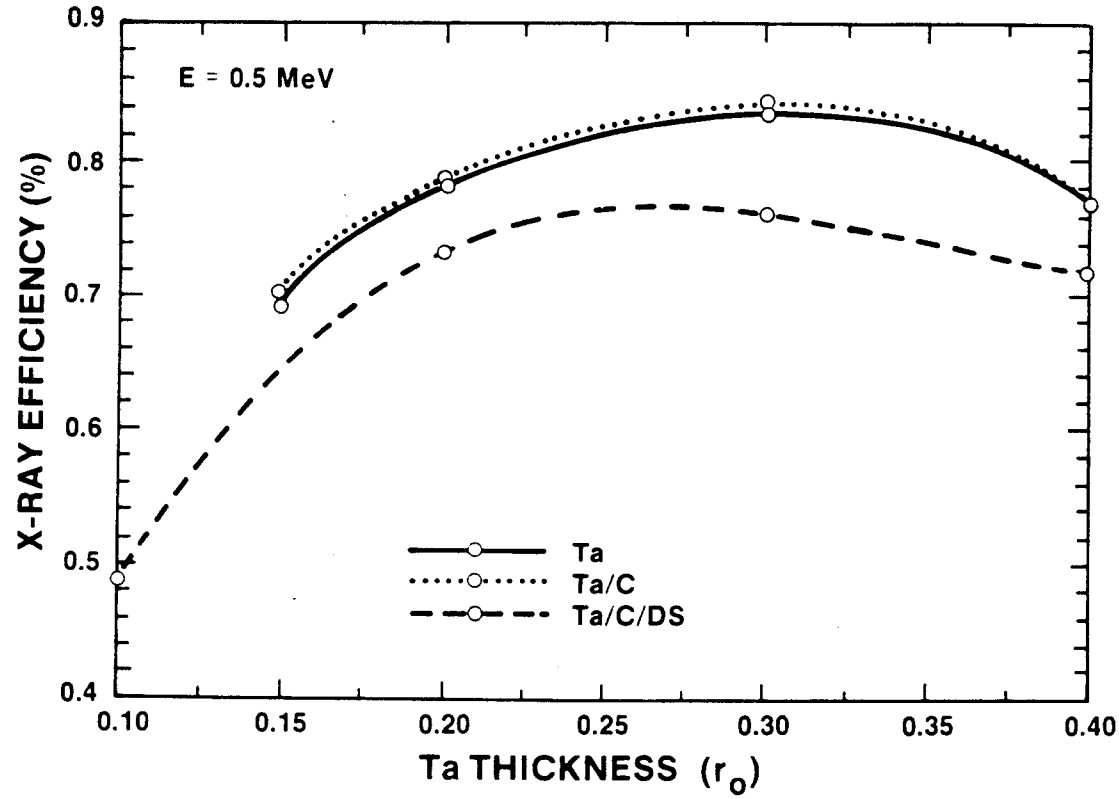

(a) 0.5 MeV

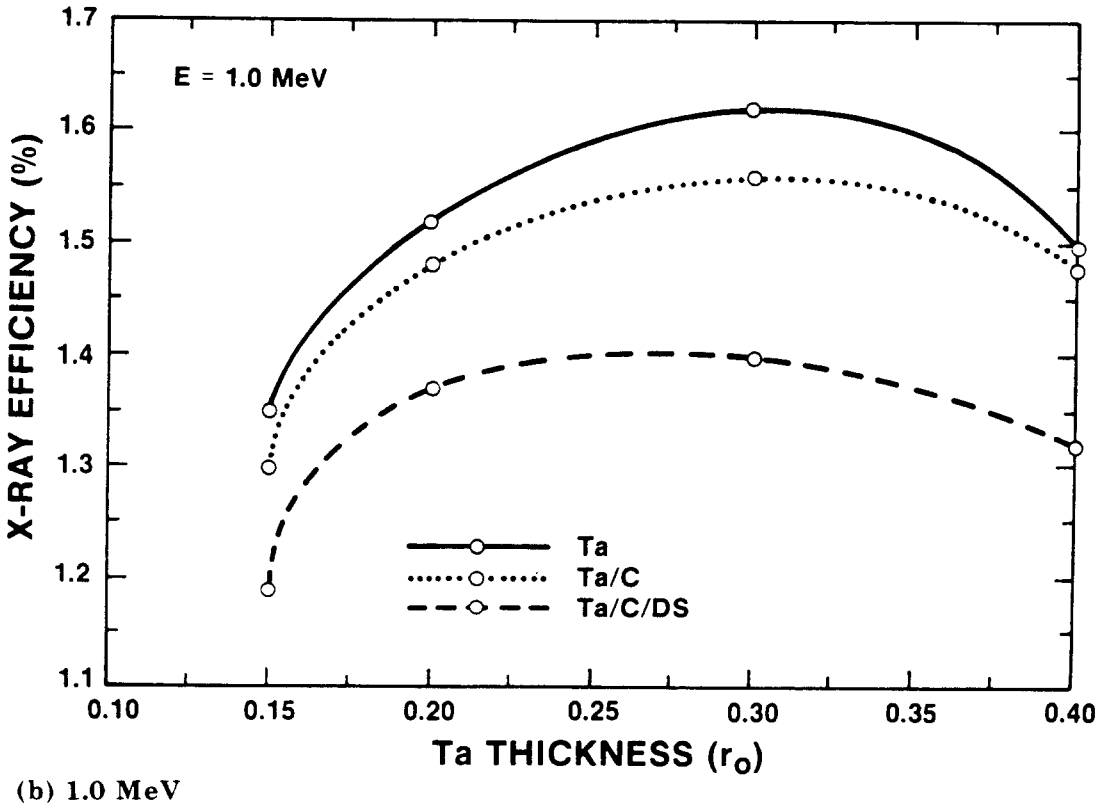

(b) 1.0 MeV

Figure 2. X-Ray Extraction Efficiency as a Function of the Thickness of the Tantalum Converter Foil for the Three Converter Configurations (a) 0.5 MeV, (b) 1.0 MeV, (c) 2.0 MeV, (d) 5.0 MeV, (e) 10.0 MeV, and (f) 15.0 MeV

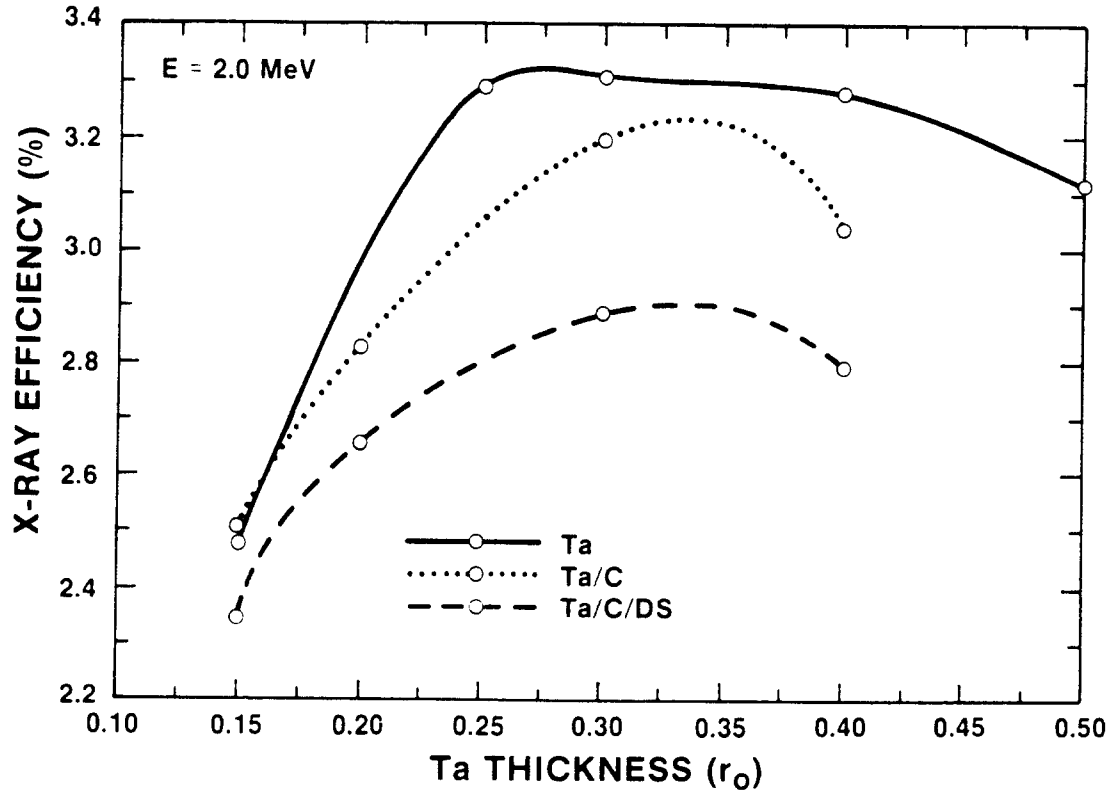

(c) 2.0 MeV

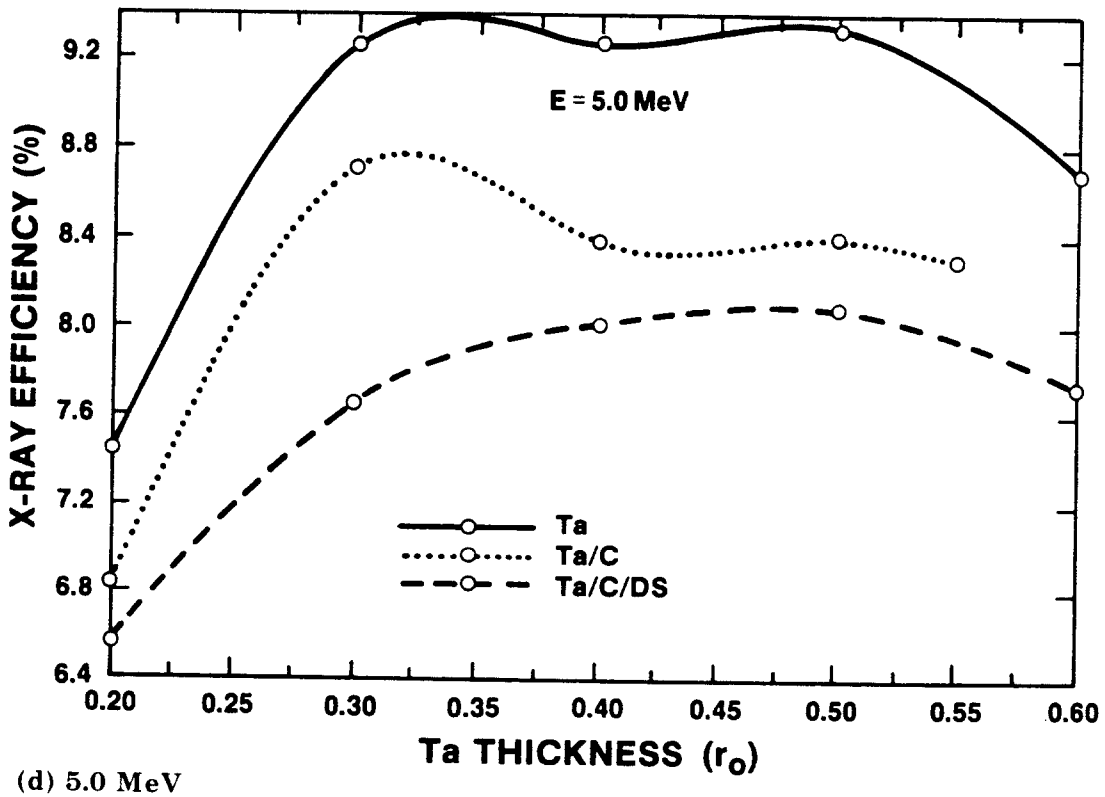

(d) 5.0 MeV

Figure 2. (Continued)

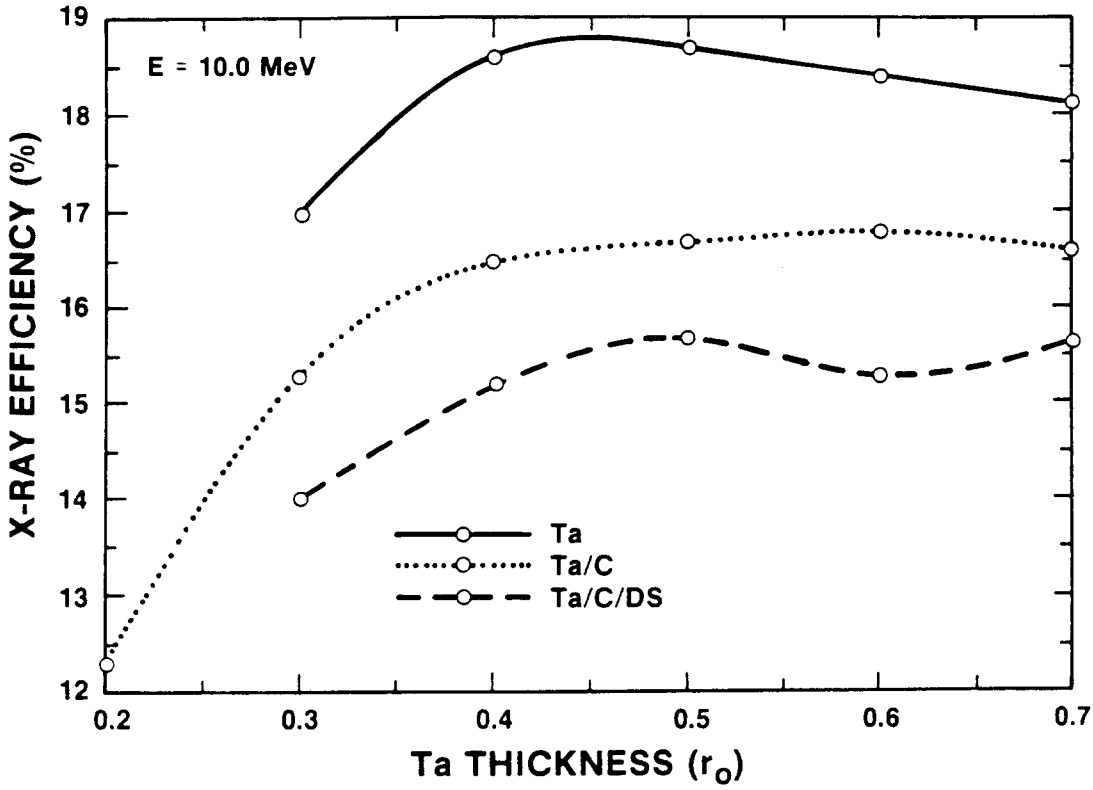

(e) 10.0 MeV

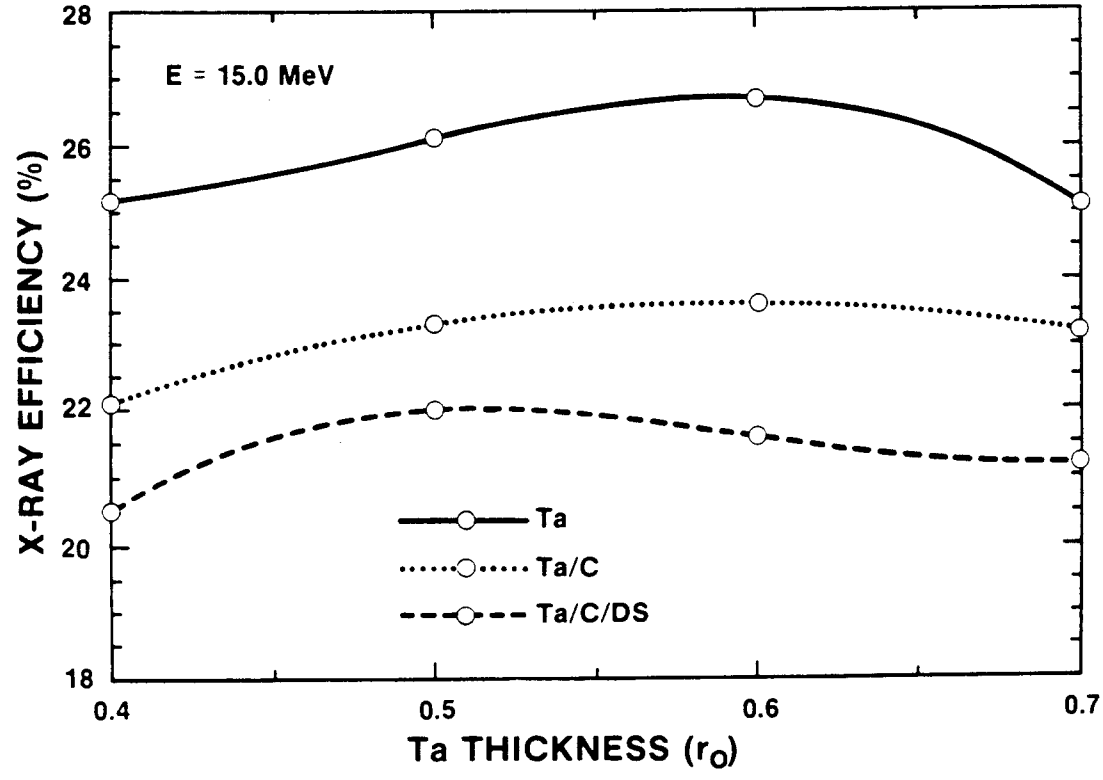

(f) 15.0 MeV

Figure 2. (Concluded)

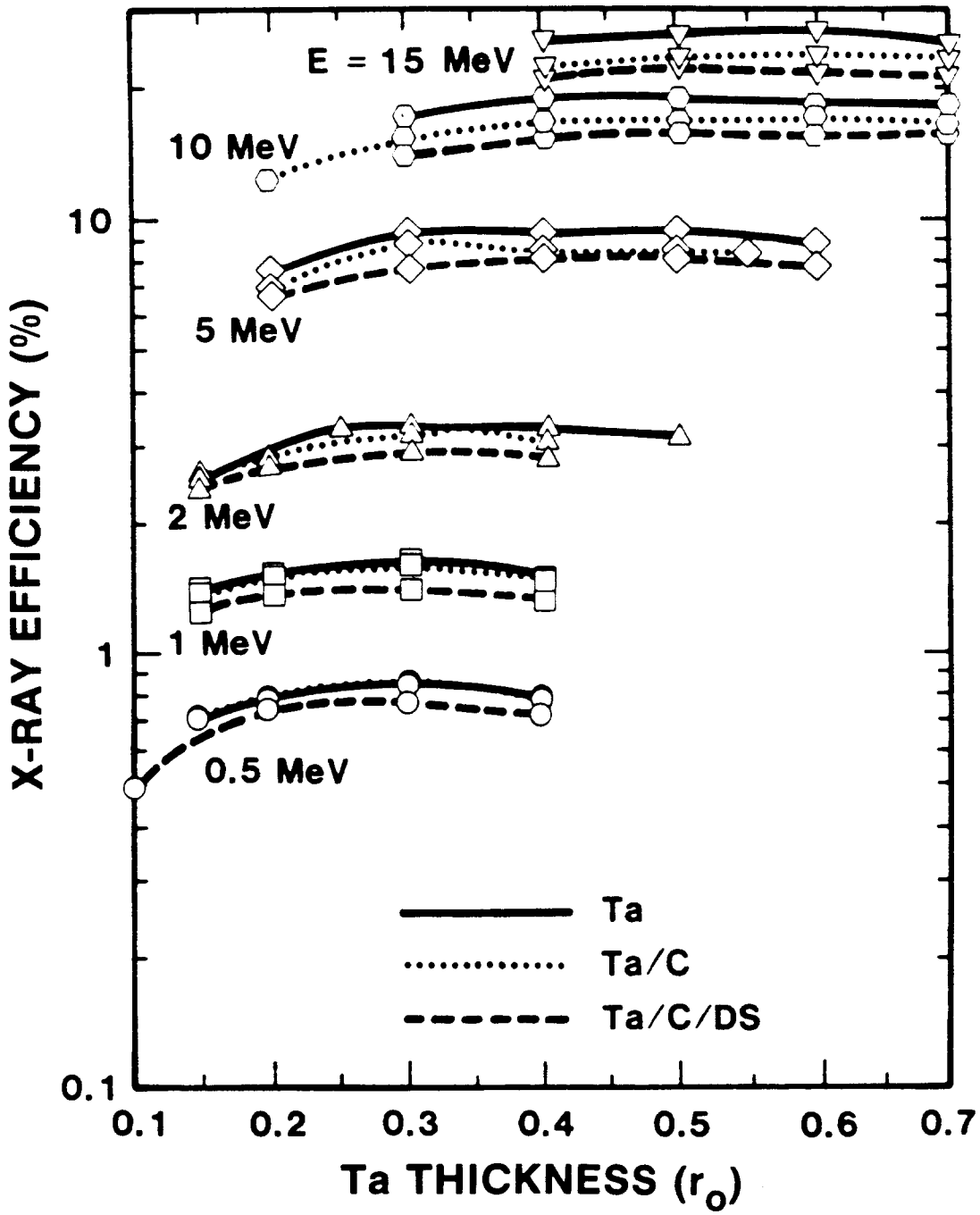

Figure 3. X-Ray Extraction Efficiency as a Function of the Thickness of the Tantalum Converter Foil for the Three Converter Configurations and for All Source Electron Energies

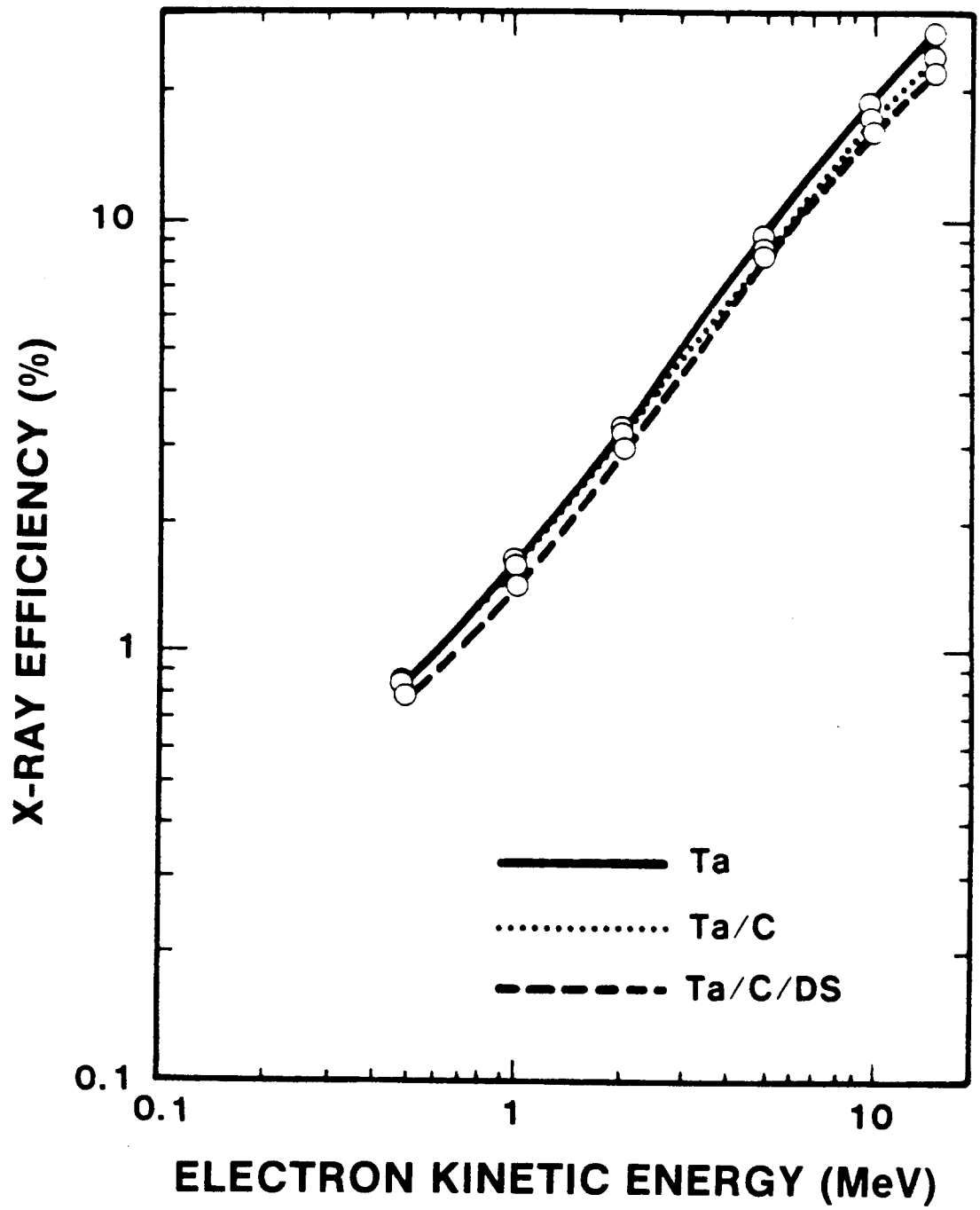

Figure 4. Optimized X-Ray Extraction Efficiency as a Function of Source Electron Energy for the Three Converter Configurations

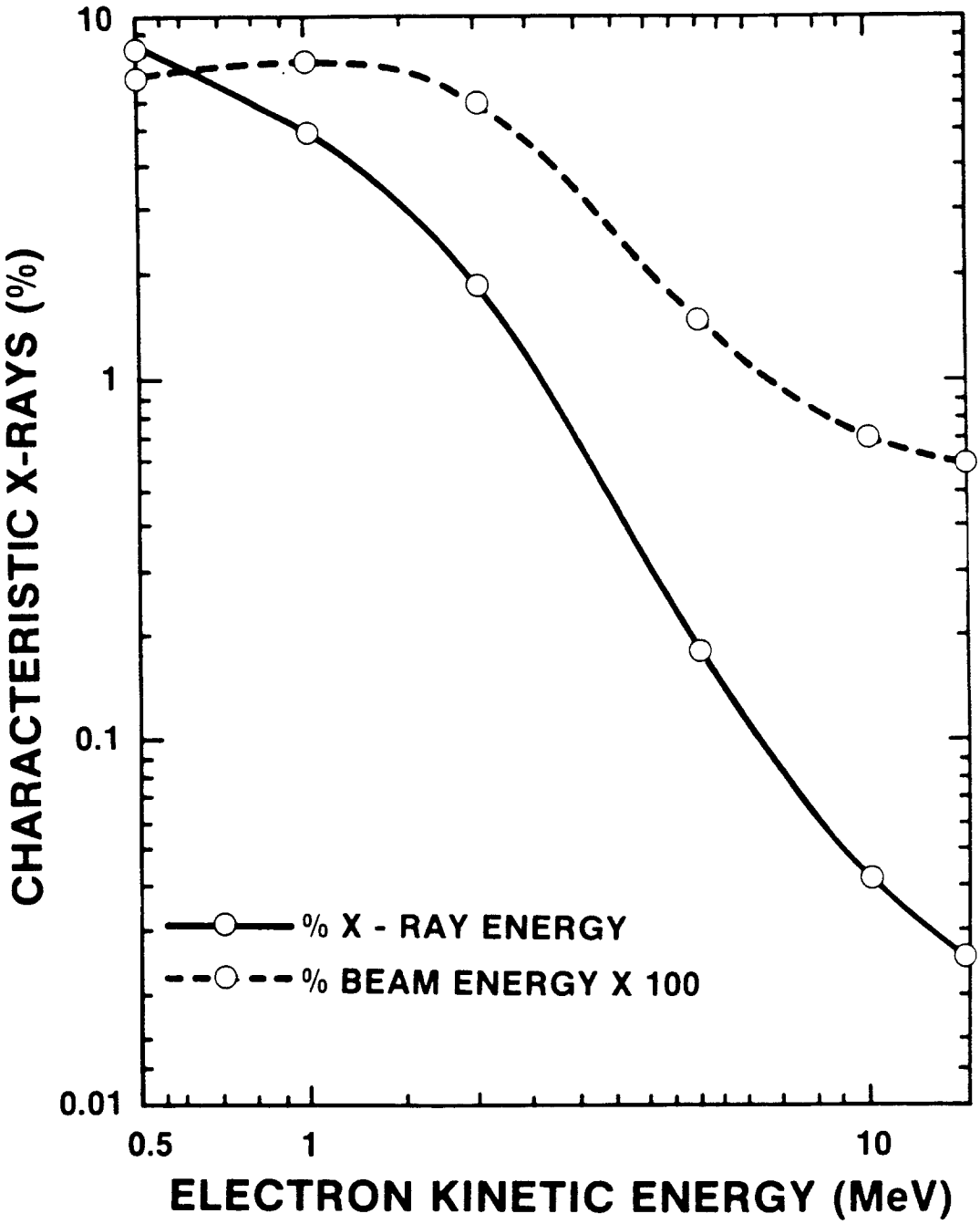

Figure 5. Forward Extracted K-X-Ray Energy as a Function of Source Electron Energy (Expressed both as a percent of the total forward extracted x-ray energy and the total beam energy)

The average energy of the forward-extracted photon spectrum is plotted in Fig. 6 as a function of the source-electron kinetic energy. The estimated SD's are no more than 1%. Expressed as a percent of the electron kinetic energy, the average photon energy decreases from just over 20% at 0.5 MeV to just over 10% at 15.0 MeV. However, because of the strong dependence of photon interaction cross sections on photon energy, the average photon energy is of little practical importance. We will have more to say about this in Sec. 5.

It is also instructive to look at the overall physics of the electron-to-photon conversion process. In Fig. 7, we have plotted several integral x-ray quantities as a function of source-electron kinetic energy for the Ta/C configuration. The estimated SD's are no more than 3%. The yield is an upper bound to the available x-ray energy. It is the percent of an electron's energy, on the average, that is converted into x rays as the electron thermalizes in an infinite medium of tantalum. Here, the yield is only approximate, however, because, for simplicity, it is calculated in CSDA and includes only x-ray production by the primary electron. The curve labelled "production" is the Monte Carlo prediction of the mean x-ray production per primary electron in the Ta/C configuration. It should always be less than the yield because it accounts for the possibility that electrons may escape from the finite geometry of the tantalum foil. In our model, most of the electron escape is in the backward direction (reflection—see below) because very few primaries can penetrate the converter configurations, and photoemission is negligible. Production exceeds the yield at 10.0 and 15.0 MeV because the yield is calculated in CSDA and does not include radiation or collisional straggling. Not shown here is the total production, which also includes production by secondary electrons. At these source energies, the differences are negligible. The difference between the "total-escape" and "production" curves represents that portion of the x-ray production that is absorbed within the converter configuration. Photons escaping in the backward direction also represent a loss mechanism for these standard converter configurations. These losses have their biggest effect at low source energies where the backward efficiency approaches the forward efficiency. The backward efficiency becomes a much smaller fraction of the total escape as the source energy increases because the angular distributions of all cross sections become more forward-peaked with increased energy. In fact, the backward efficiency appears to have reached a maximum at about 10.0 MeV. Thus, we see that the three primary effects that keep the forward extraction efficiency from approaching the radiation yield are (a) electron reflection, (b) photon reflection, and (c) photon absorption.

Electron backscattering is shown in Fig. 8 as a function of source-electron kinetic energy for the Ta/C configuration. The estimated SD's range from about 5% at 0.5 MeV to about 15% at 15.0 MeV. Electron backscattering can be an especially large loss mechanism at low kinetic energies, unless there is some mechanism (e.g., diode electric field) for returning backscattered electrons to the converter.

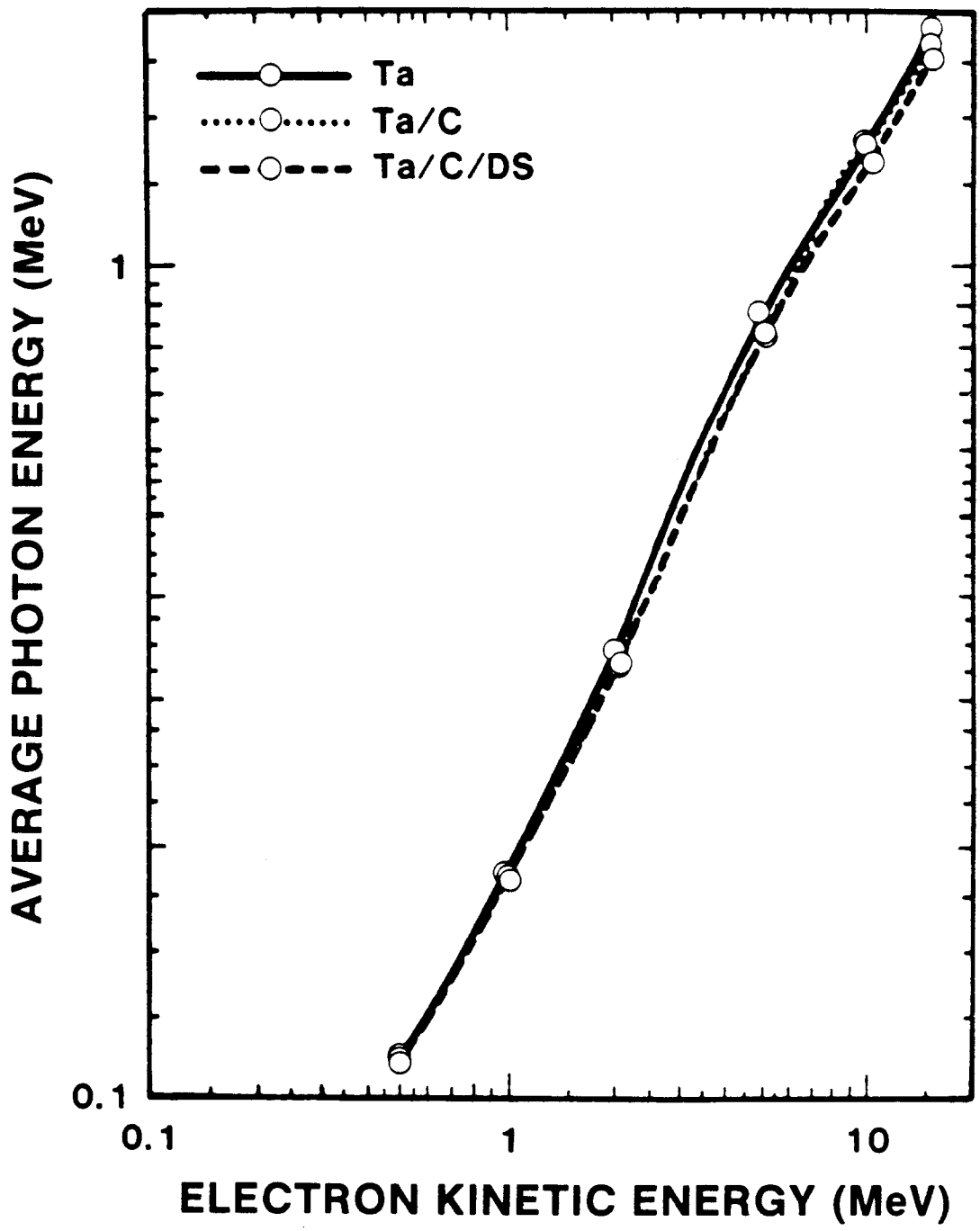

Figure 6. Average Energy of Forward-Directed Photons as a Function of Source Electron Energy for the Three Converter Configurations

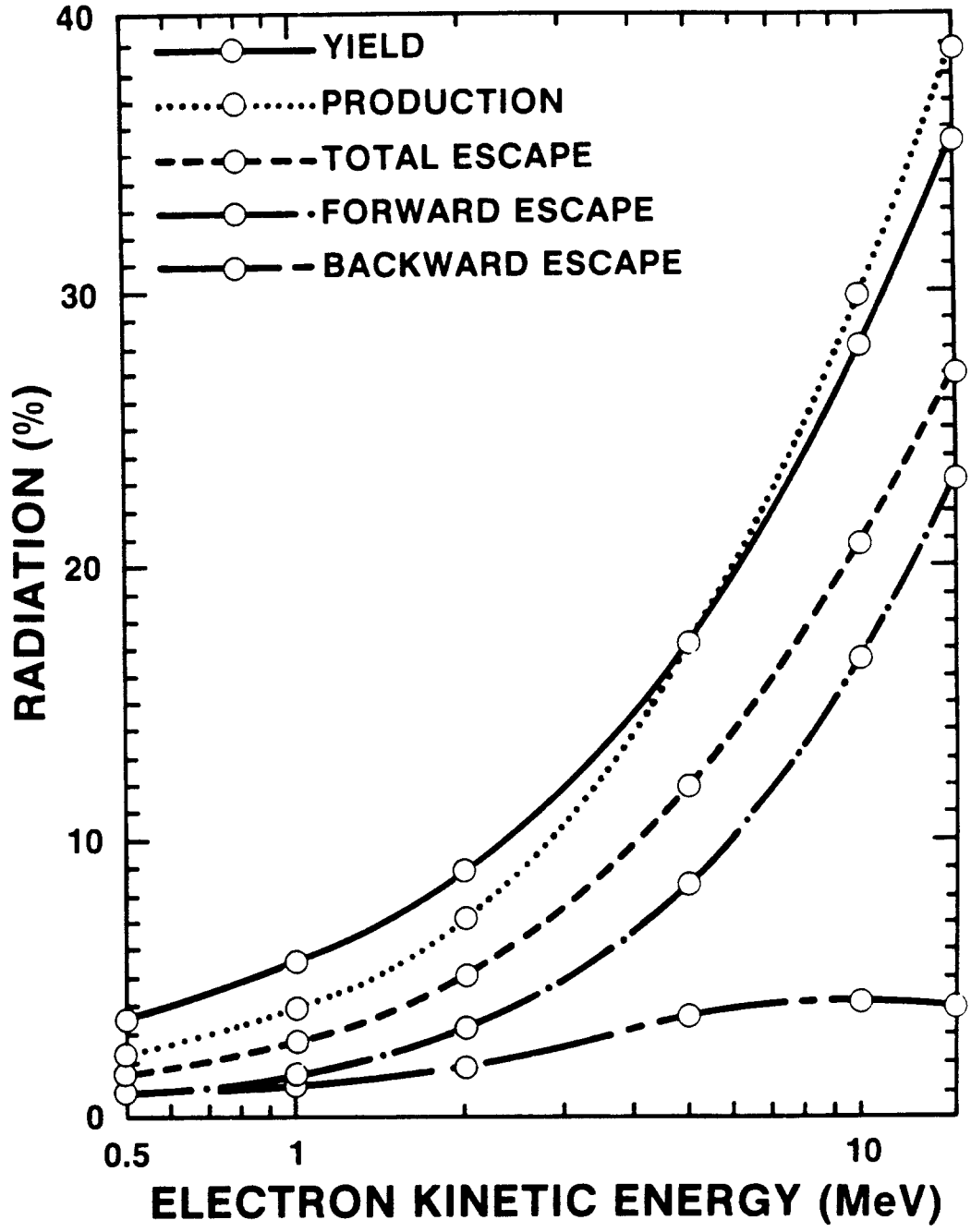

Figure 7. Comparison of Various Integral X-Ray Quantities as a Function of Source Electron Energy

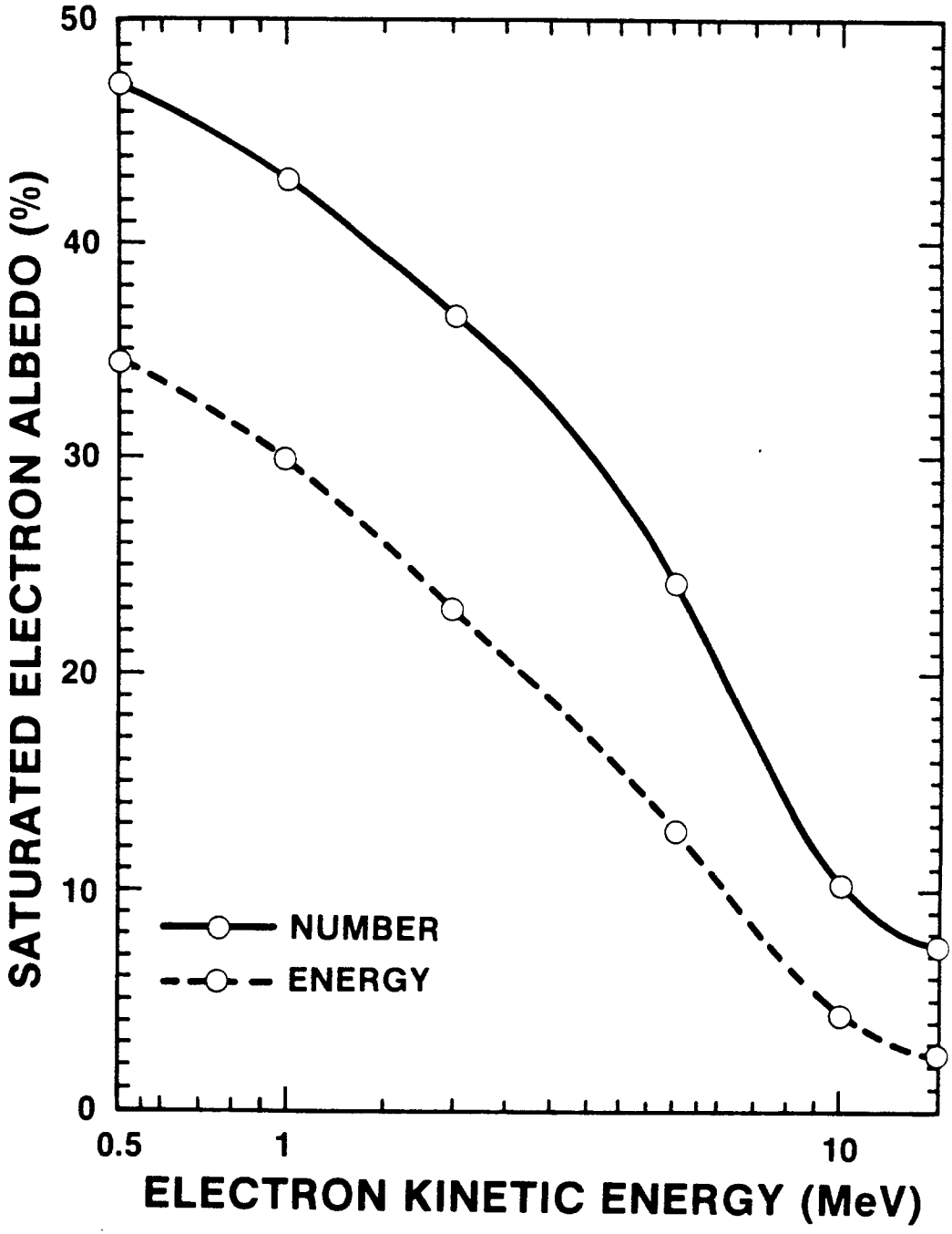

Figure 8. Saturated Electron Number and Energy Albedos as a Function of Source Electron Energy

4.2 X-Ray Spectra

In many applications the x-ray spectrum is more important than the conversion efficiency because the experiment may be primarily sensitive to a portion, usually the low energy portion, of the spectrum. The spectrum depends primarily on the electron energy and, especially at low electron energies, on the absorption properties of the high-Z converter foil. Usually of somewhat less importance is the angular dependence of the spectrum. However, this dependence must still be taken into account because different experiments subtend different solid angles at the x-ray source.

In Figs. 9a through 9f, we compare the forward 2π number spectrum with the number spectrum in the smallest polar-angle interval used in the calculation for each of the six electron source energies using Ta/C converters. The 2π spectra are normalized to one incident electron. The spectra for the forward angle bins are then normalized to give the same number of photons as the 2π spectra when integrated over photon energy. The normalization factors are 35.7, 31.7, 95.3, 340.0, 731.0, and 480.0 for source-electron energies of 0.5, 1.0, 2.0, 5.0, 10.0, and 15.0 MeV, respectively. The estimated SD's in the 2π spectra decrease from about 2% to 3% over most of the spectral range at a source energy of 0.5 MeV to about 1% at a source energy of 15.0 MeV. For the small forward-angle bins, the corresponding uncertainties increase from about 5% at a source energy of 0.5 MeV to about 10% to 20% at 15.0 MeV. The small-angle spectra are softer than the 2π spectra at low electron energies. This softness is due to the dominance of slant-thickness absorption of the relatively low-energy photons in the high-Z converter at the high emission angles of the 2π spectra. At high electron energies, the small-angle spectra are harder than the 2π spectra. This hardness is due to (1) the basic photon production cross section that favors high energy forward production over the lower energy large-angle production, and (2) the reduced effect of the slant-thickness absorption because absorption in general is reduced for the higher energy photons now being produced. These arguments are consistent with the angular distributions of the average photon energy discussed below. All of the 2π spectra are plotted together in Fig. 10.

In Figs. 11a through 11f, the forward 2π photon intensity spectra are plotted for each source-electron energy—again, for the Ta/C converters. Statistical uncertainties are comparable to those of the number spectra. Note that because of the energy weighting of these spectra relative to the number spectra, semilog plots are more appropriate. The shapes of these thick-target spectra are easy to understand. At high photon energies, where self-absorption by the converter is unimportant, the spectra decrease monotonically with increasing photon energy, reflecting the approximate $(h\nu)^{-1}$ dependence of the photon production cross section. At low photon energies, absorption by the high-Z converter foil determines the shape. In particular, a depression in the vicinity of the K-shell binding energy is clearly visible in all the spectra. Conversely, there are always peaks in the spectra just below this binding energy, corresponding to a depression in the attenuation coefficient for Ta. The energies of the K-shell fluorescent radiation also happen to fall near this peak, giving rise to significant line radiation at low source-electron energies. This K-shell structure is of less significance at high electron kinetic energies where the correspondingly greater optimum thicknesses of the converters suppress emission at these photon energies. At very low photon energies, self-absorption by the converter system effectively extinguishes emission.

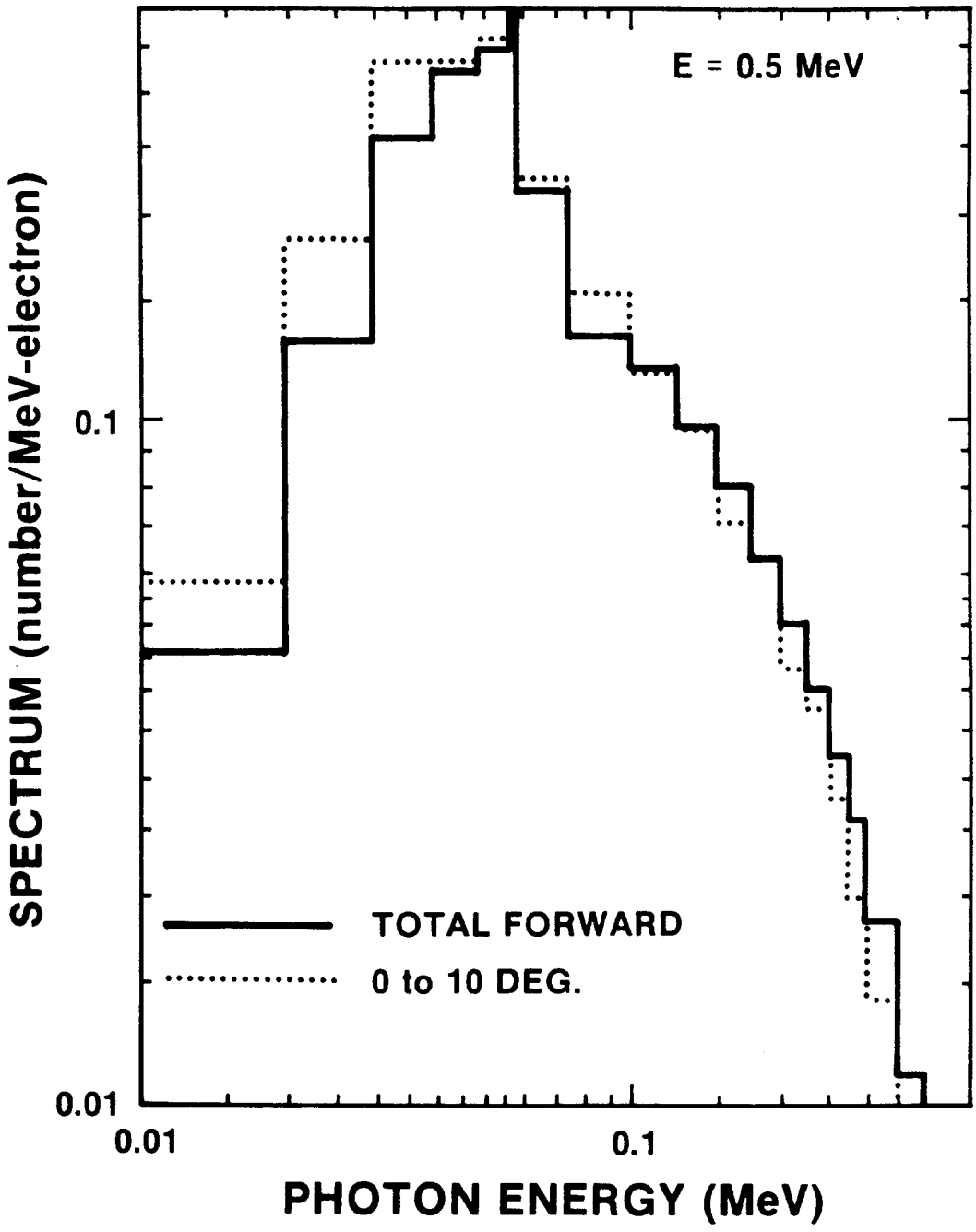

(a) 0.5 MeV

Figure 9. Comparison of the Total Forward Photon Spectrum With the Spectrum in the Forwardmost Angular Bin at Each Source Electron Energy (a) 0.5 MeV, (b) 1.0 MeV, (c) 2.0 MeV, (d) 5.0 MeV, (e) 10.0 MeV, and (f) 15.0 MeV

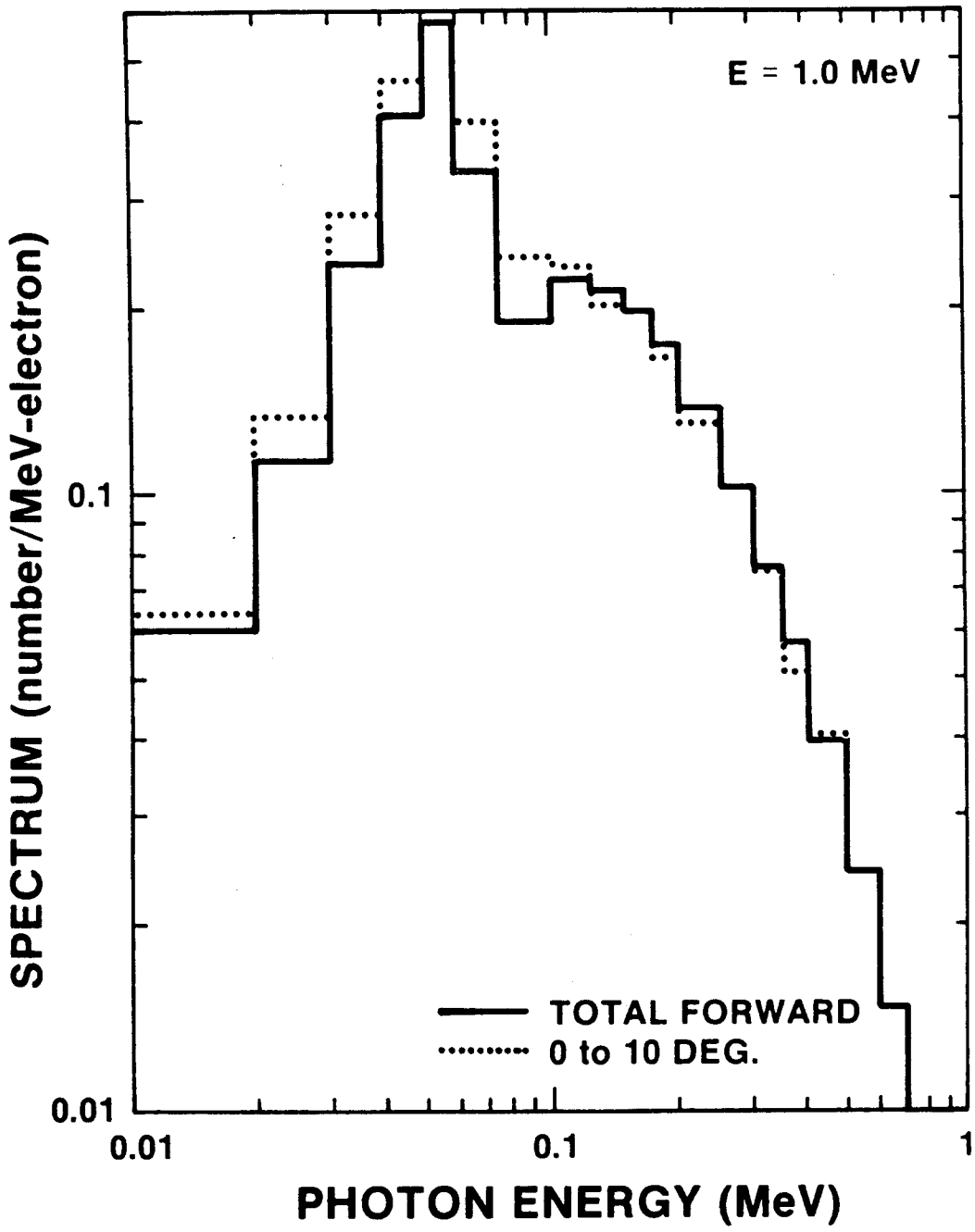

(b) 1.0 MeV

Figure 9. (Continued)

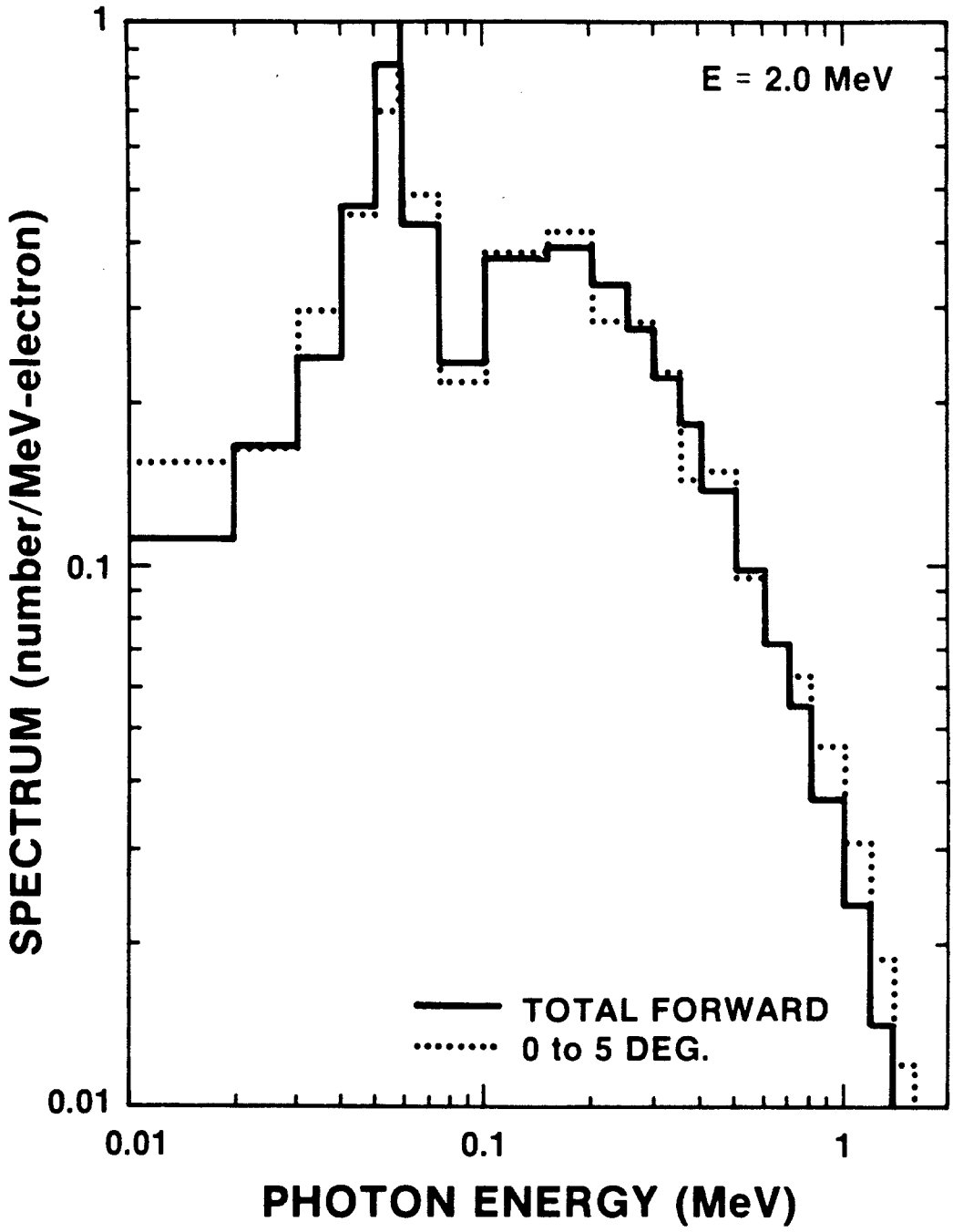

(c) 2.0 MeV

Figure 9. (Continued)

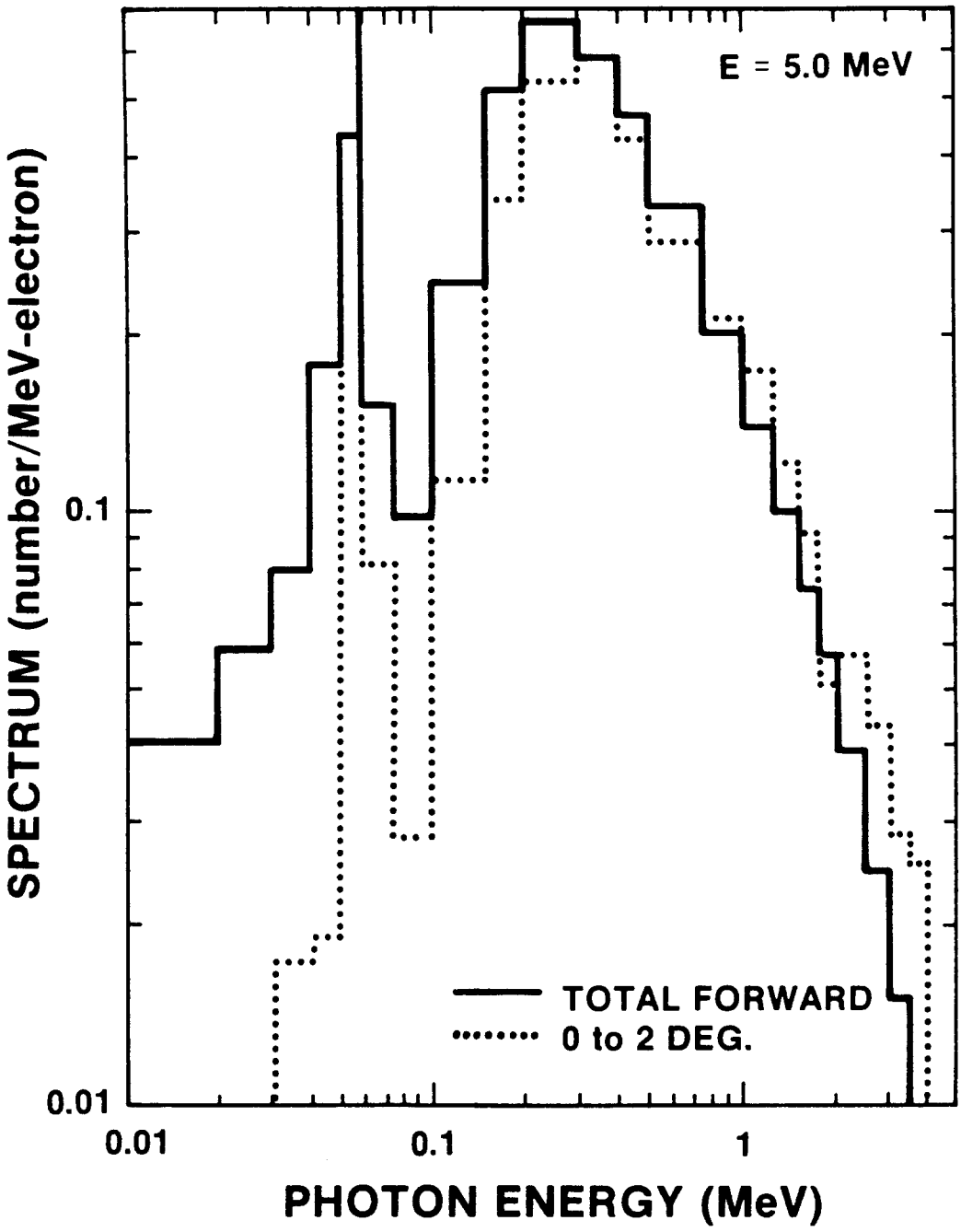

(d) 5.0 MeV

Figure 9. (Continued)

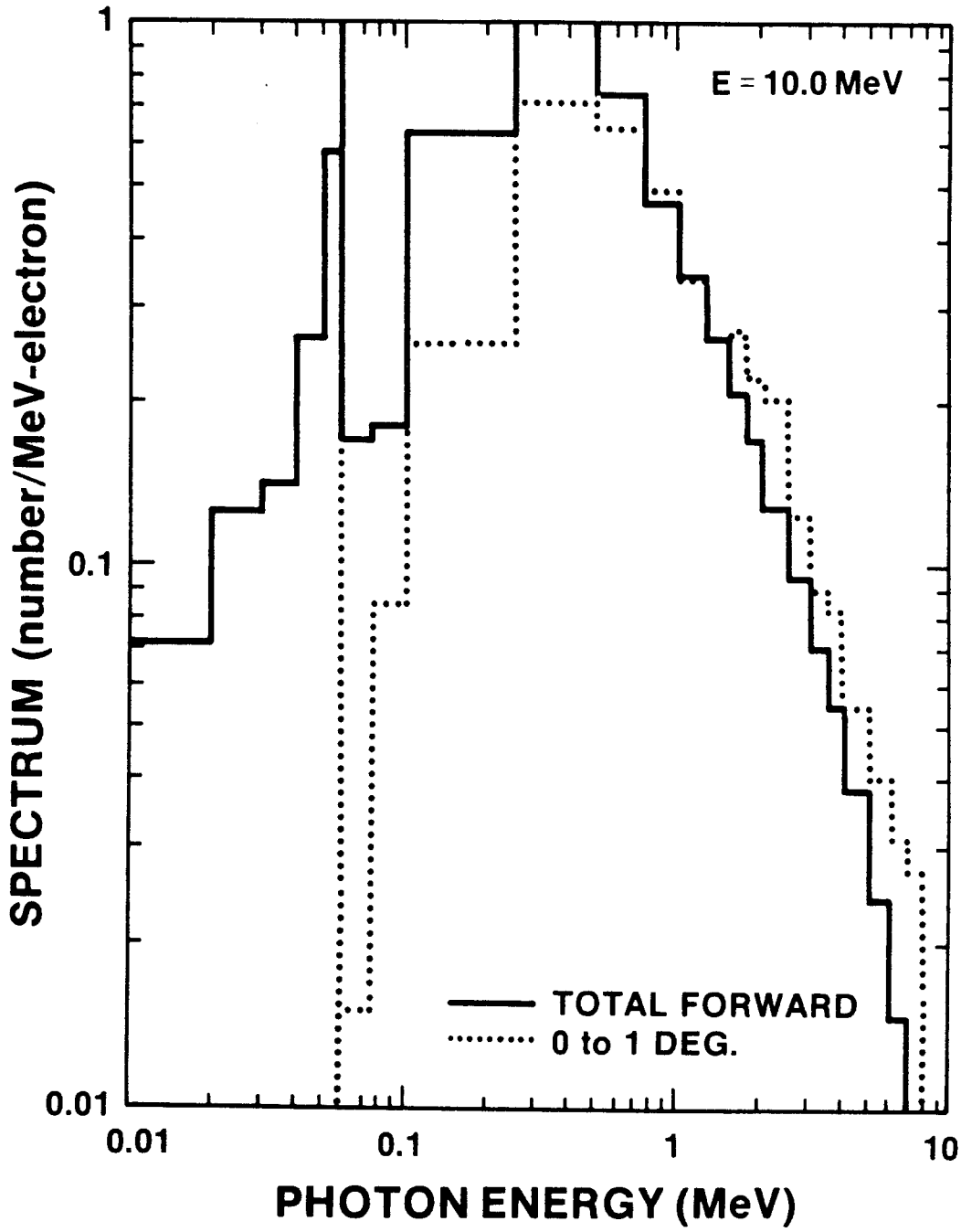

(e) 10.0 MeV

Figure 9. (Continued)

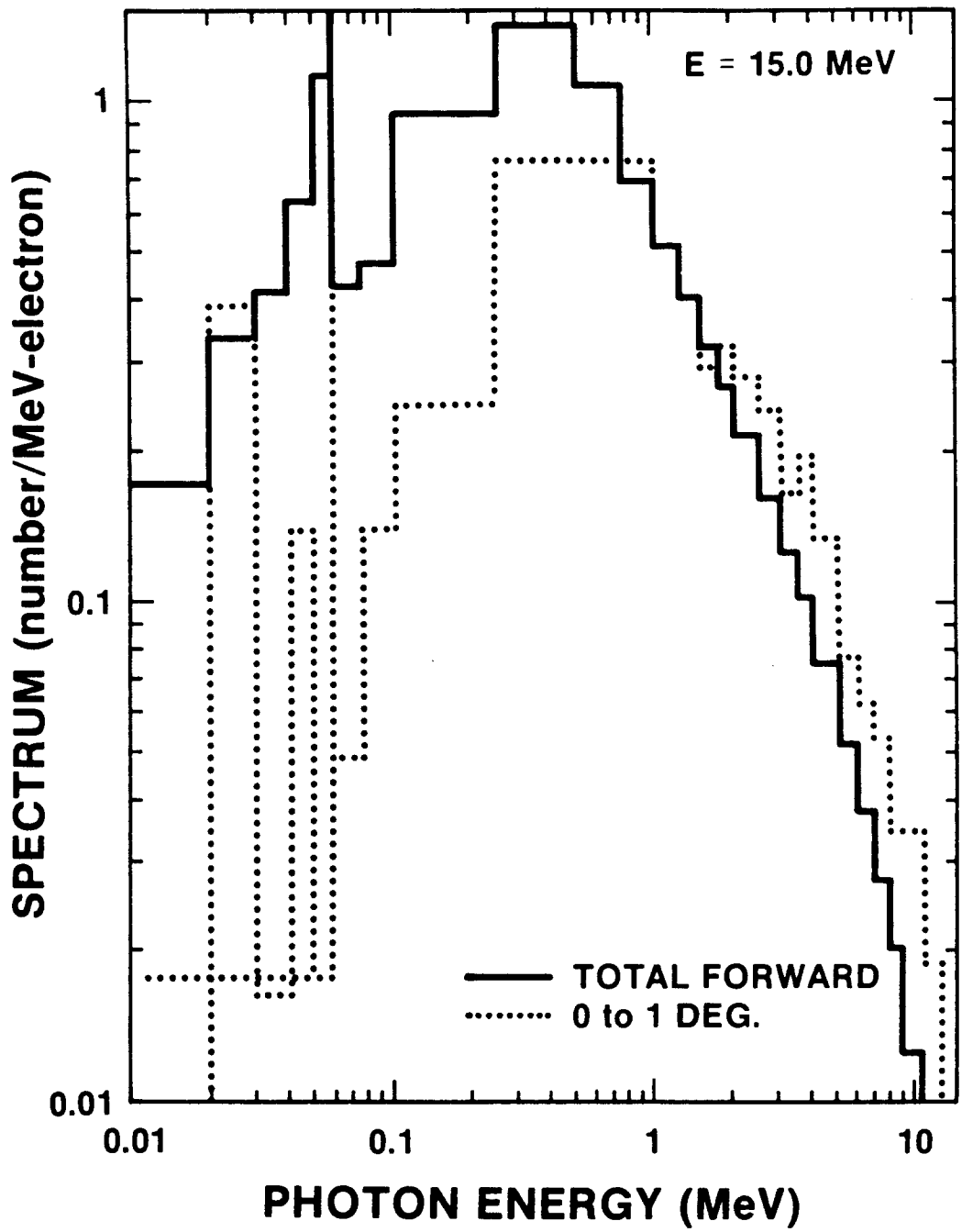

(f) 15.0 MeV

Figure 9. (Concluded)

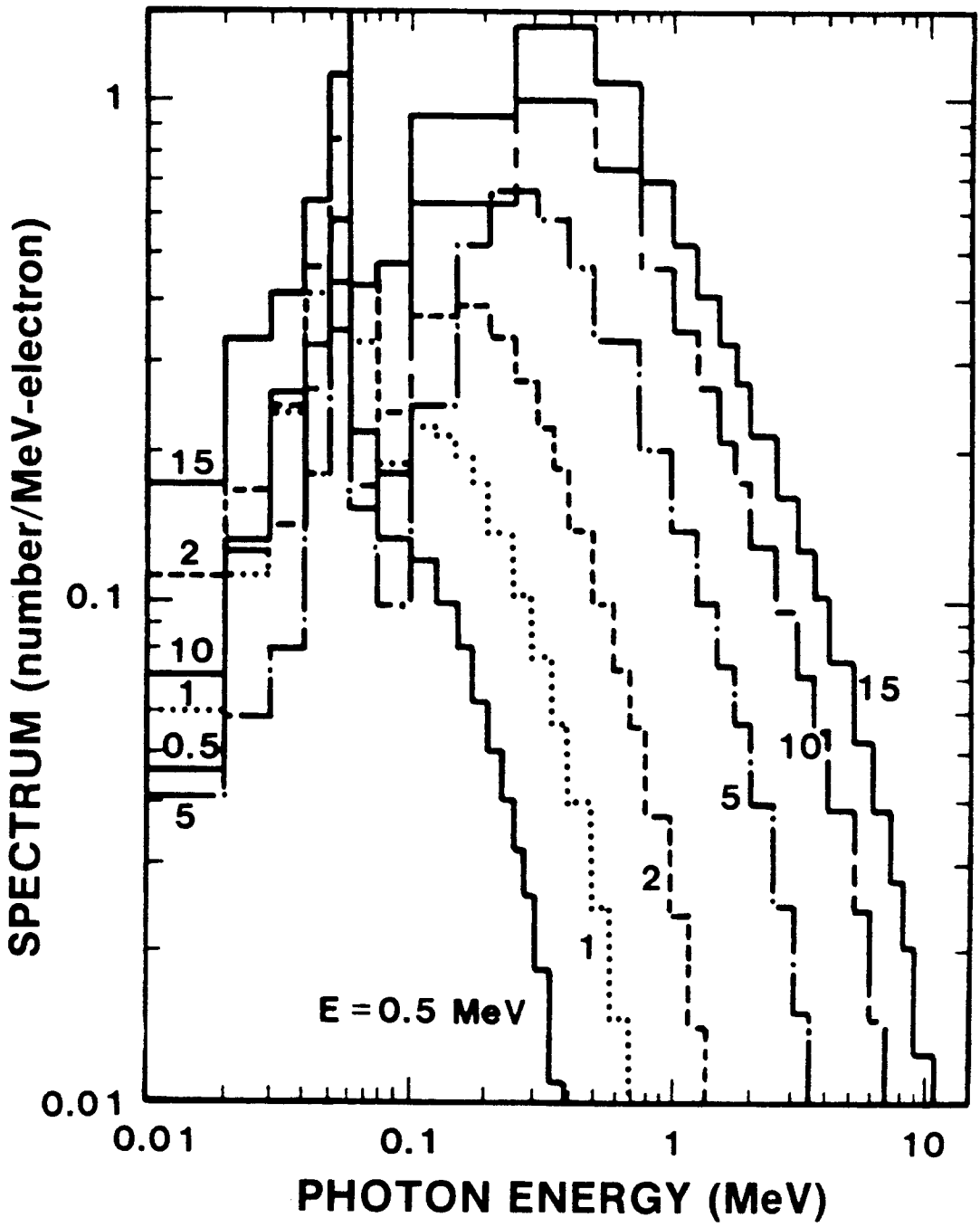

Figure 10. Comparison of the Total Forward Photon Spectra for the Six Source Electron Energies

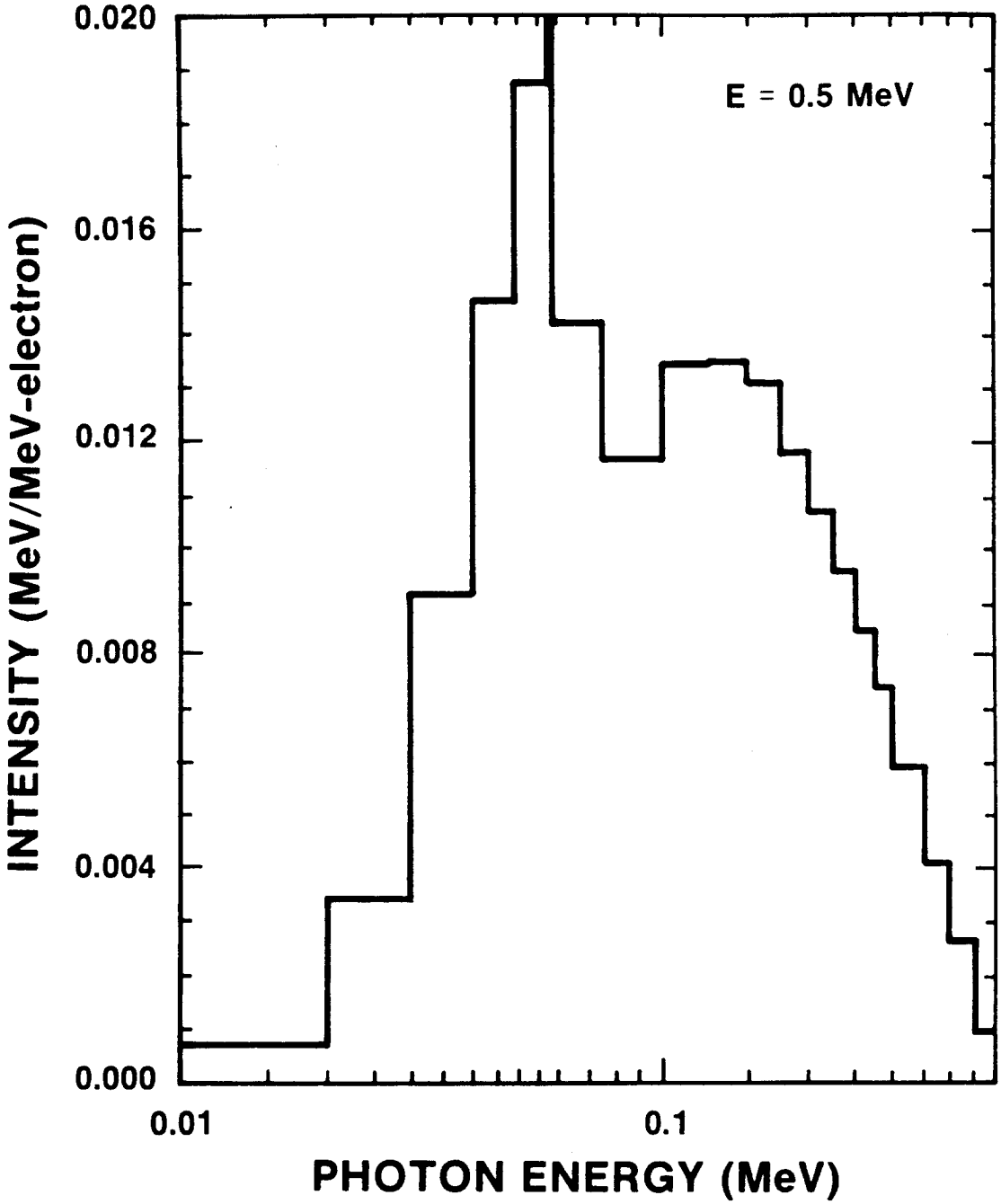

(a) 0.5 MeV

Figure 11. The Total Forward Photon Intensity Spectra at Each Source Electron Energy (a) 0.5 MeV, (b) 1.0 MeV, (c) 2.0 MeV, (d) 5.0 MeV, (e) 10.0 MeV, and (f) 15.0 MeV

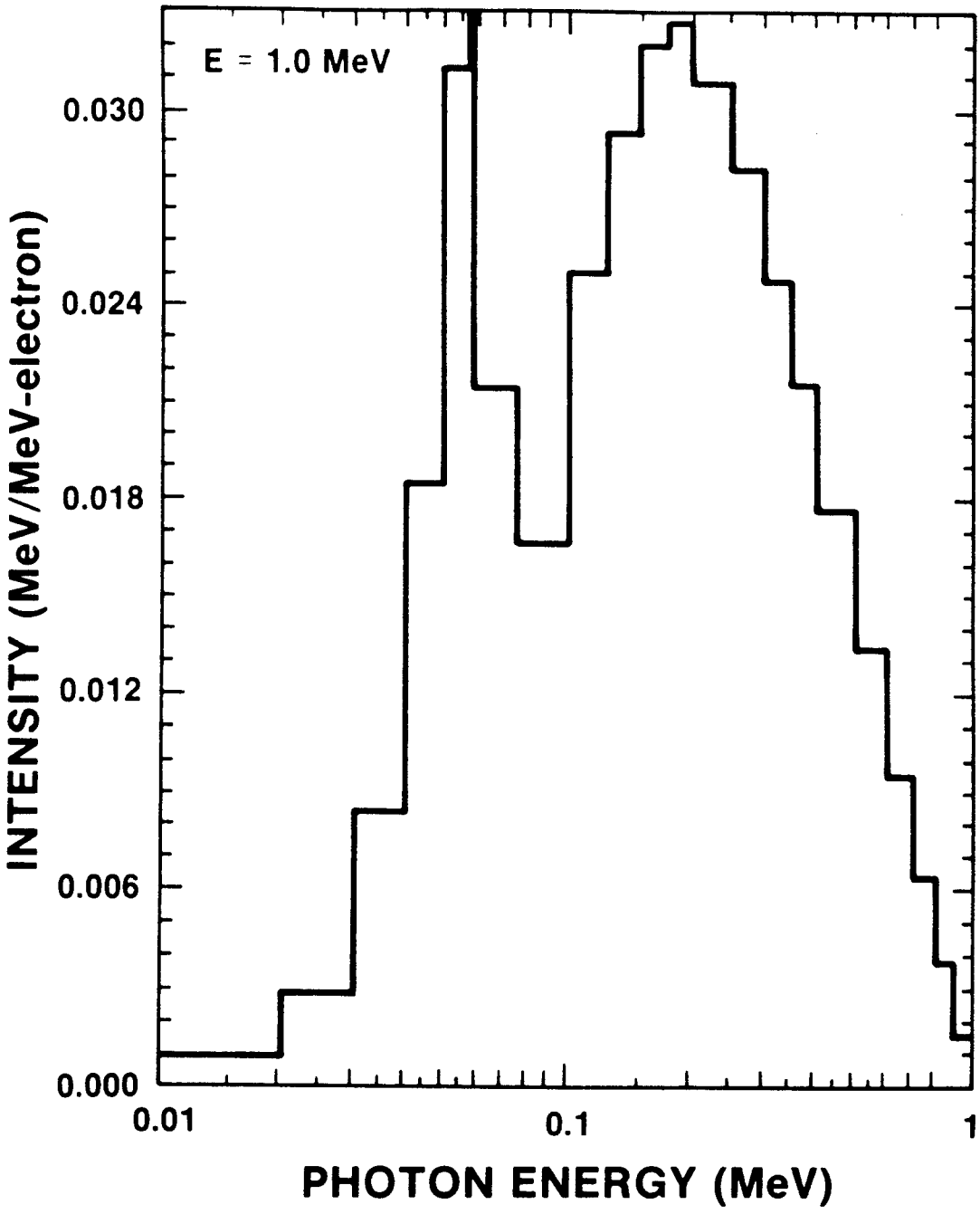

(b) 1.0 MeV

Figure 11. (Continued)

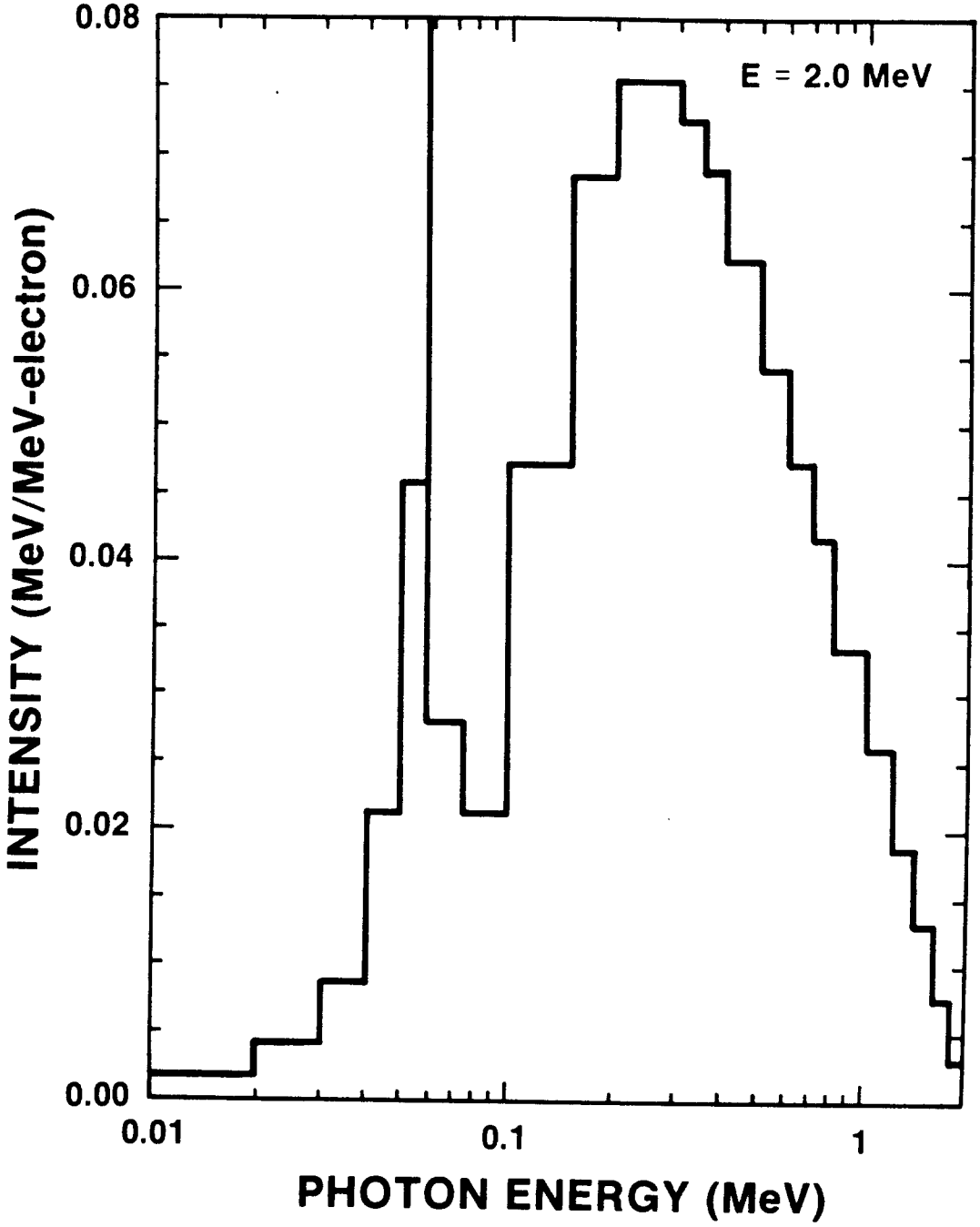

(c) 2.0 MeV

Figure 11. (Continued)

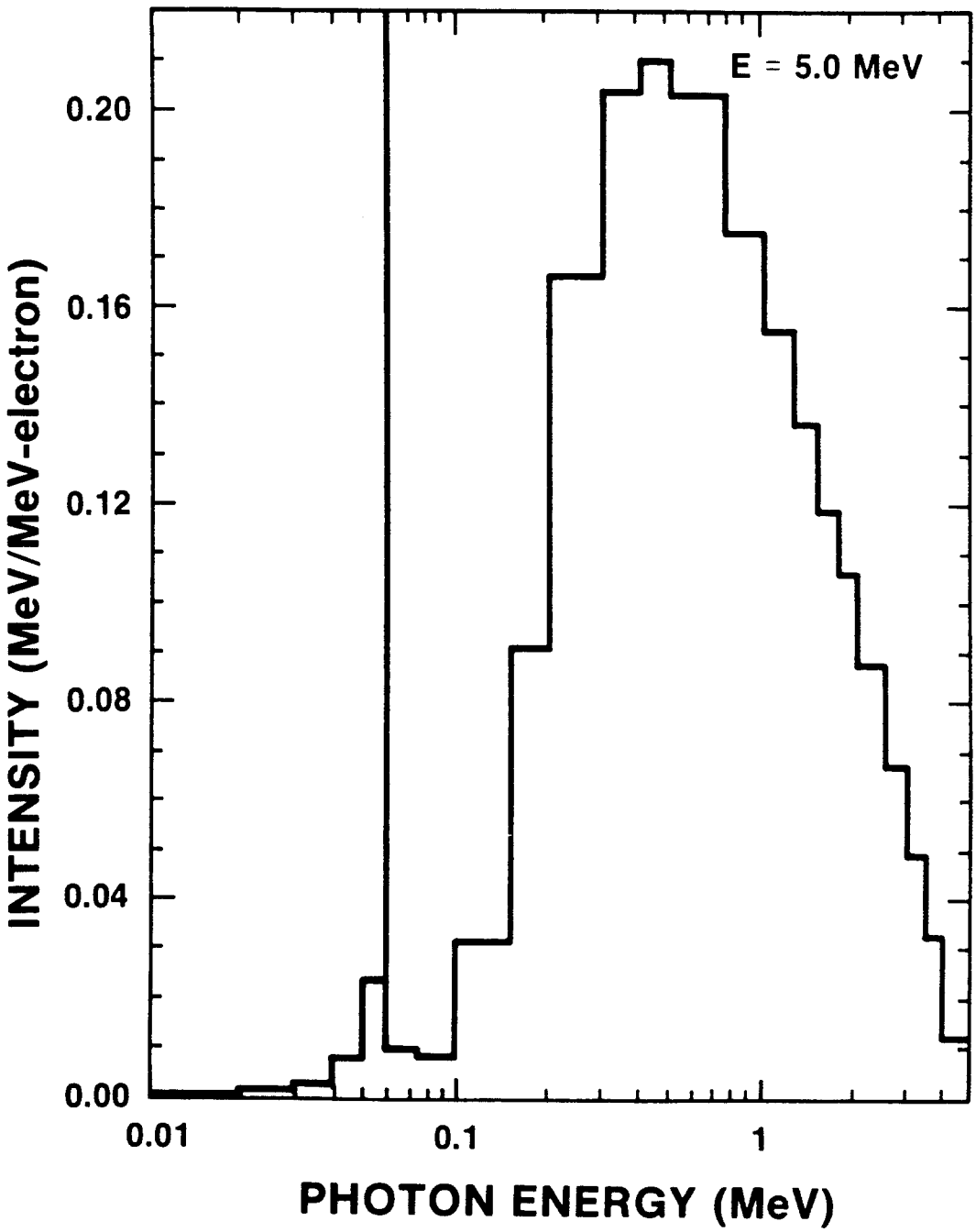

(d) 5.0 MeV

Figure 11. (Continued)

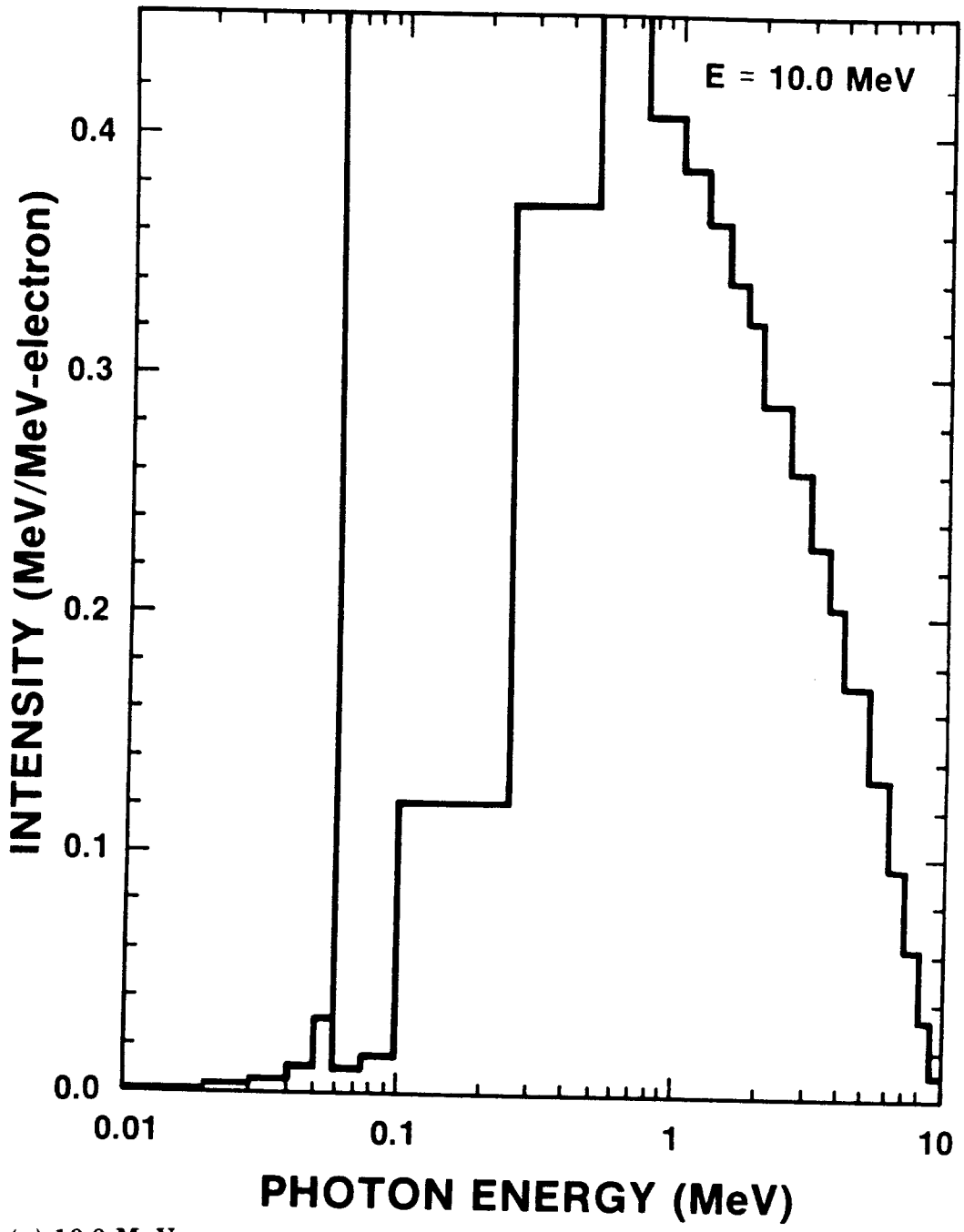

(e) 10.0 MeV

Figure 11. (Continued)

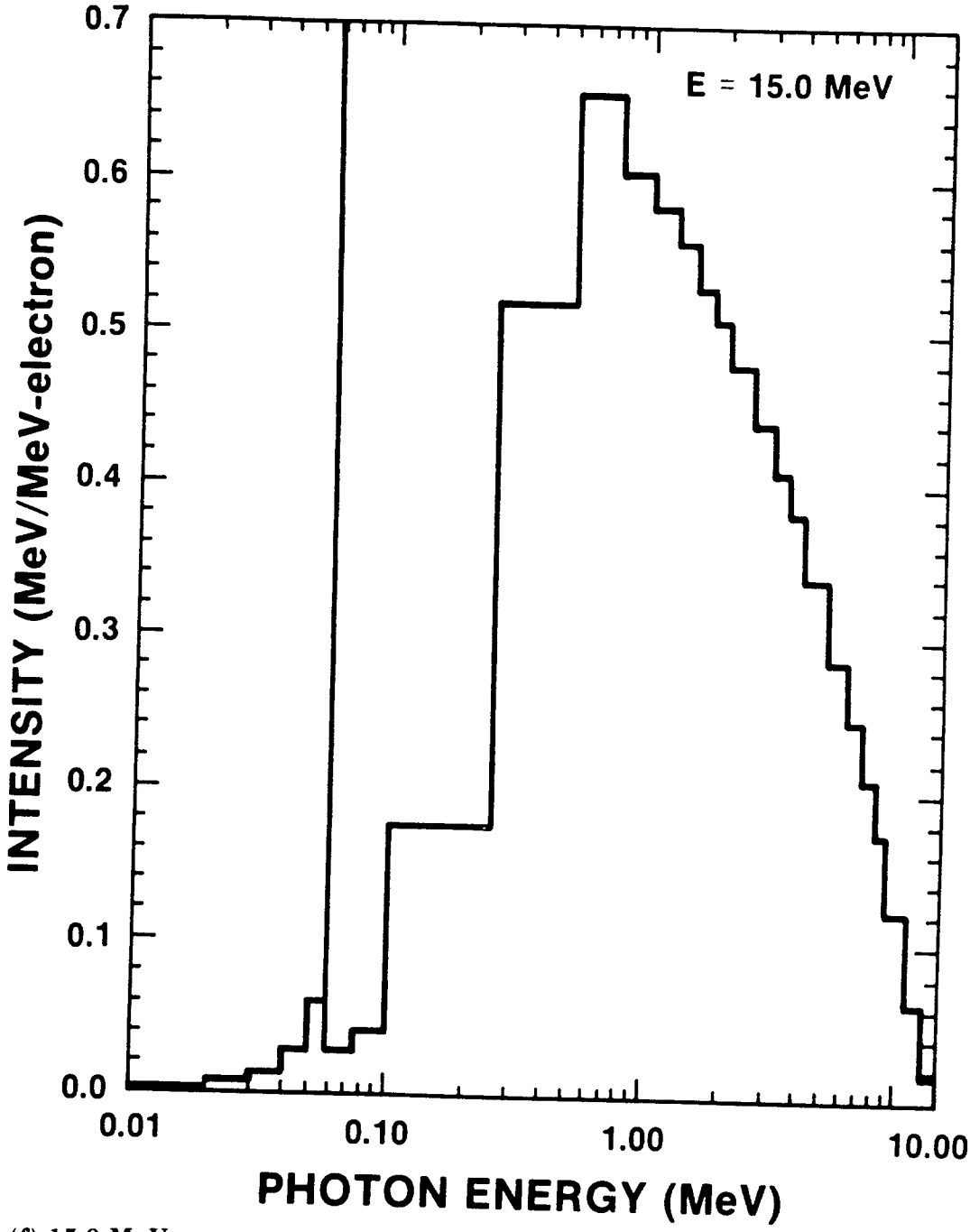

(f) 15.0 MeV

Figure 11. (Concluded)

4.3 X-Ray Angular Distributions

Angular distributions are useful to the experimenter for determining to what extent different parts of his experimental package see different radiation environments, or for estimating the change in the environment caused by relocating part or all of the package. Fig. 12 is a plot of the normalized angular distributions of the x rays emitted over the forward 2π solid angle. The absolute number of photons emitted per steradian per incident electron were normalized to a peak value of 1.0. The normalization factors are 89.6, 35.7, 11.7, 2.56, 0.588, and 0.238 for source-electron energies of 0.5, 1.0, 2.0, 5.0, 10.0, and 15.0 MeV, respectively. The estimated SD's are usually about 2% and never more than 4%. Although any method for determining the FWHM (full width half maximum) of a distribution from histogram data is ambiguous at best, we see qualitatively that the FWHM of the x-ray angular distribution is a strongly decreasing function of the source-electron kinetic energy.

In Figs. 13a through 13f we have plotted the average photon energy as a function of emission angle for the three converter configurations at each of the six source-electron energies. Estimated statistical uncertainties are usually about 3%, but are about twice that for the small forward-angle bins at the high source energies. The results are consistent with Fig. 9. At high source energies, the thick-target distributions exhibit the behavior of the production cross section in that the spectra soften with increasing emission angle. At low source energies, slant-thickness absorption dominates, and the spectra become harder with increasing emission angle. The dependence on the type of configuration is more difficult to understand. At low emission angles, there is no significant dependence. However, at high angles, the Ta/C spectra are softer than the Ta spectra, and the Ta/C/DS spectra are softer still. One possible explanation is that incoherent scattering in the low-Z absorber and debris shield leads to a buildup of low-energy photons, and that this buildup is exaggerated by the large slant thicknesses at the large emission angles.

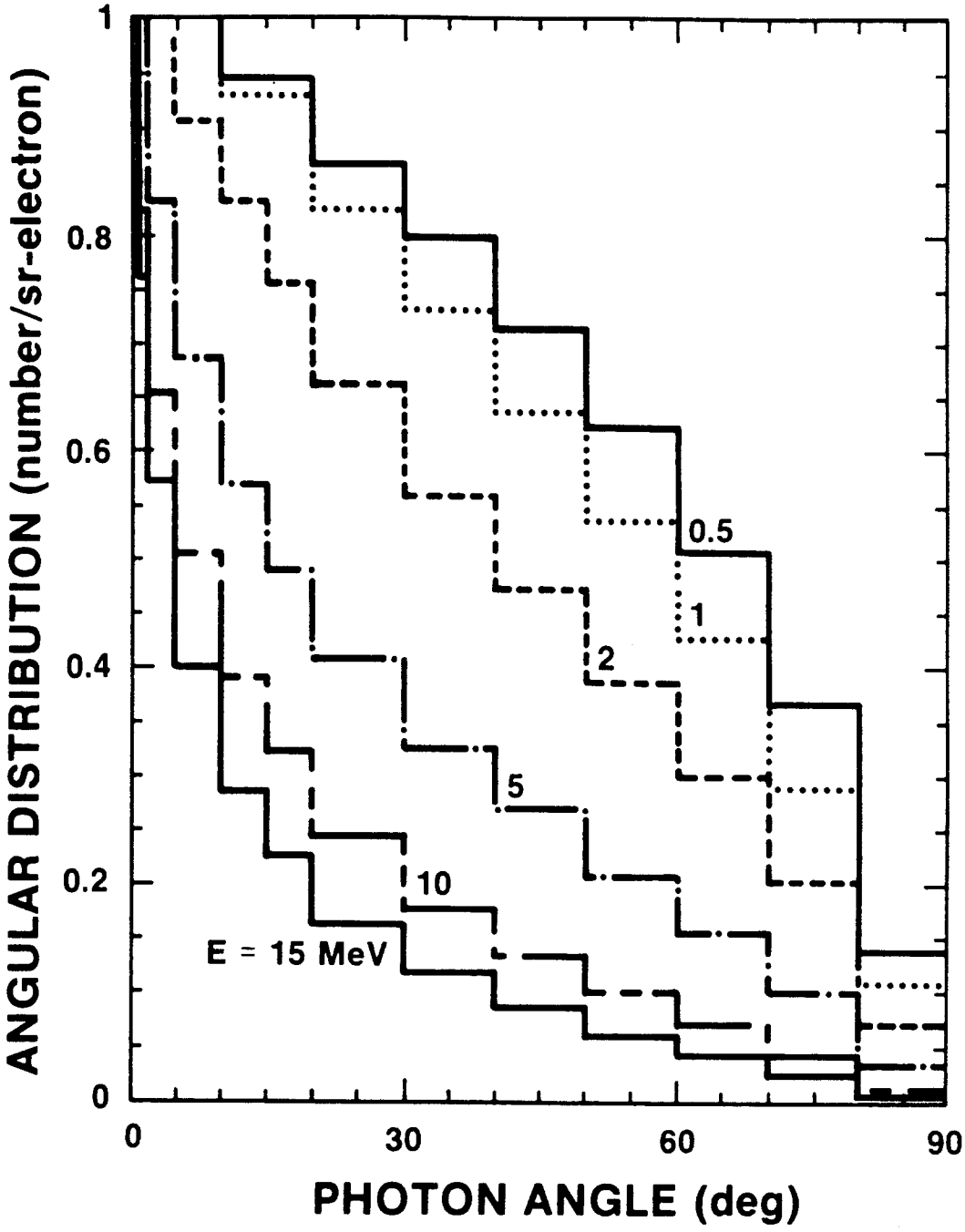

Figure 12. Normalized Angular Distributions of the Forward-Directed Photons for the Six Source Electron Energies

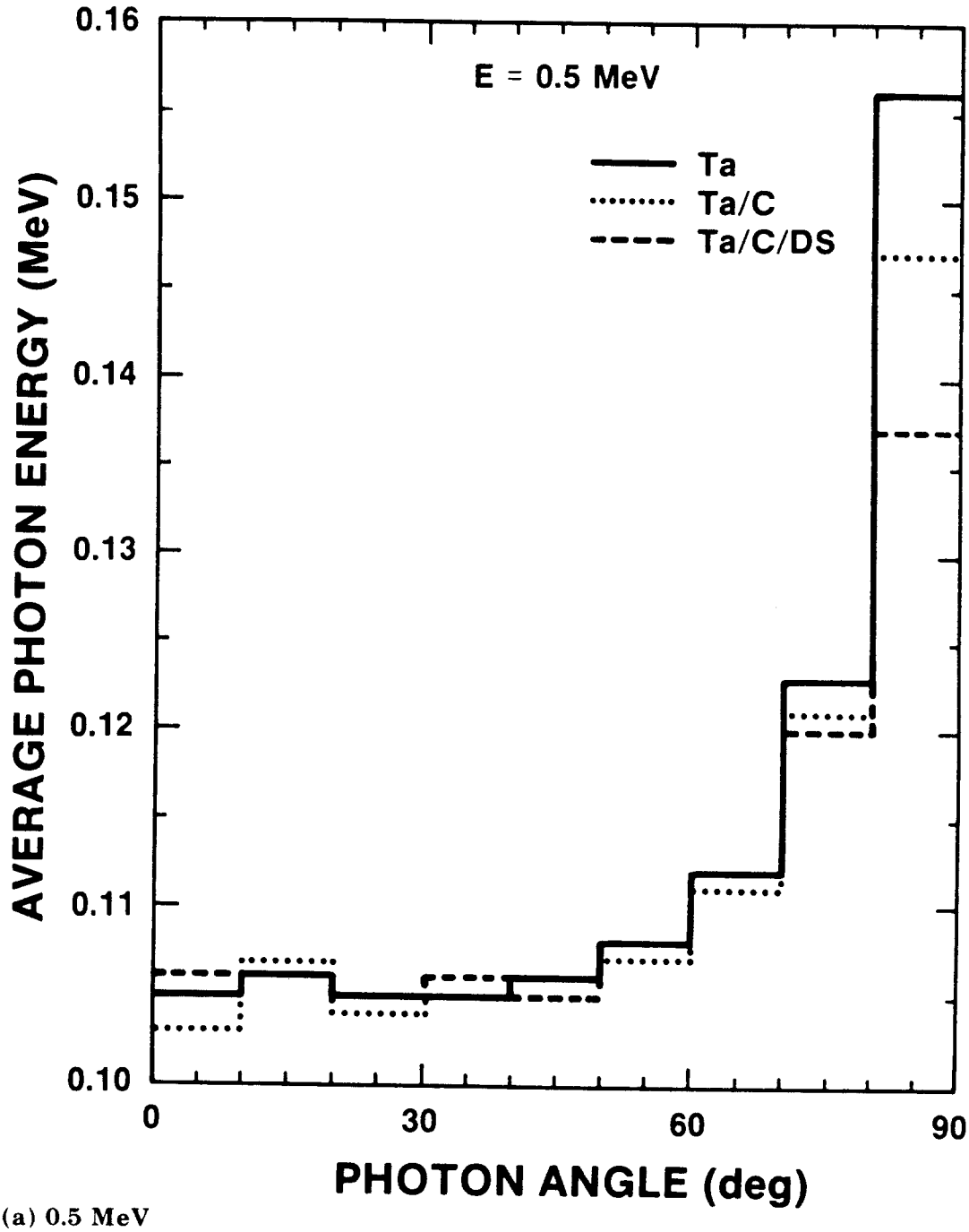

(a) 0.5 MeV

Figure 13. Average Photon Energy as a Function of X-Ray Emission Angle for the Three Converter Configurations and at Each Source Electron Energy (a) 0.5 MeV, (b) 1.0 MeV, (c) 2.0 MeV, (d) 5.0 MeV, (e) 10.0 MeV, and (f) 15.0 MeV

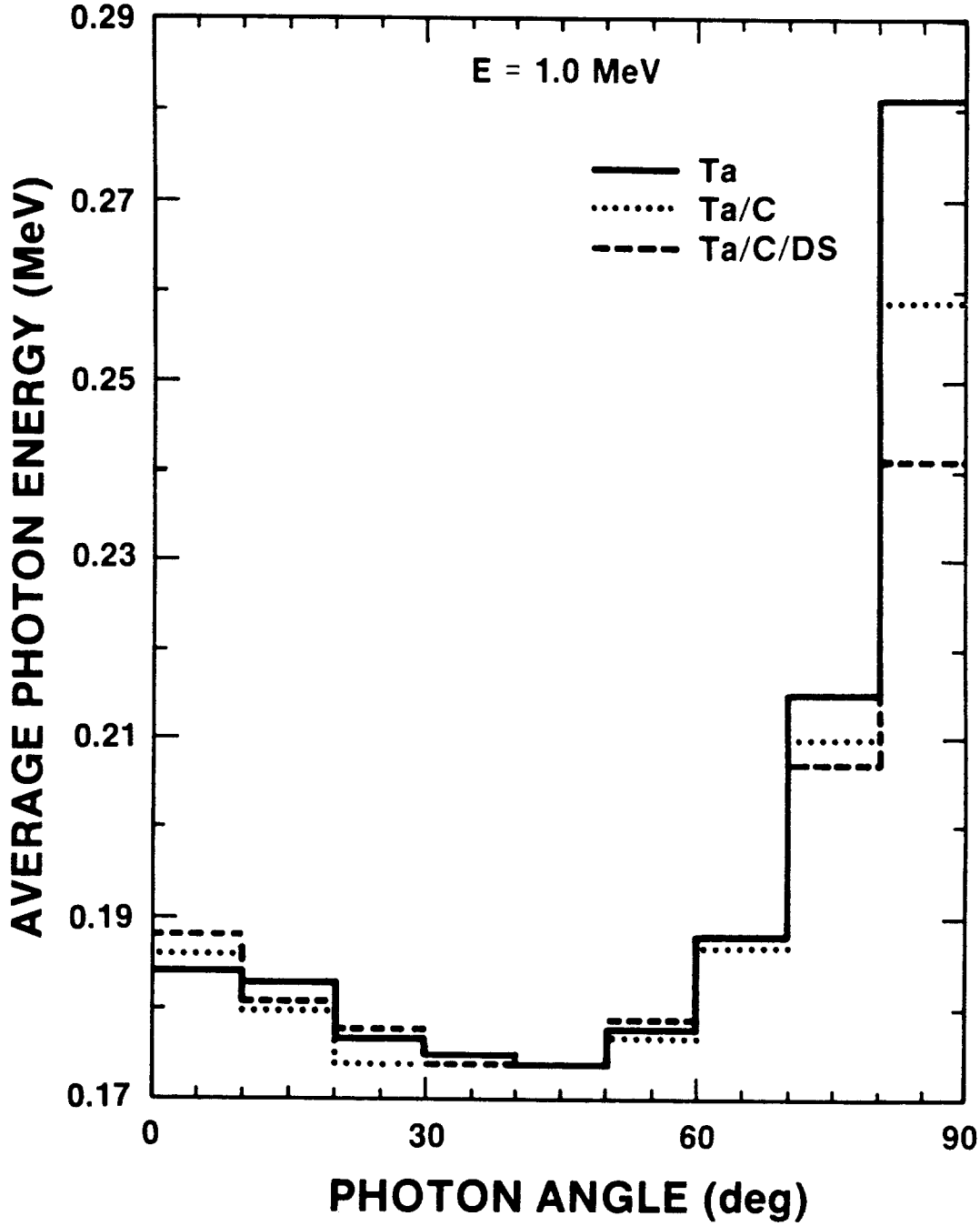

(b) 1.0 MeV

Figure 13. (Continued)

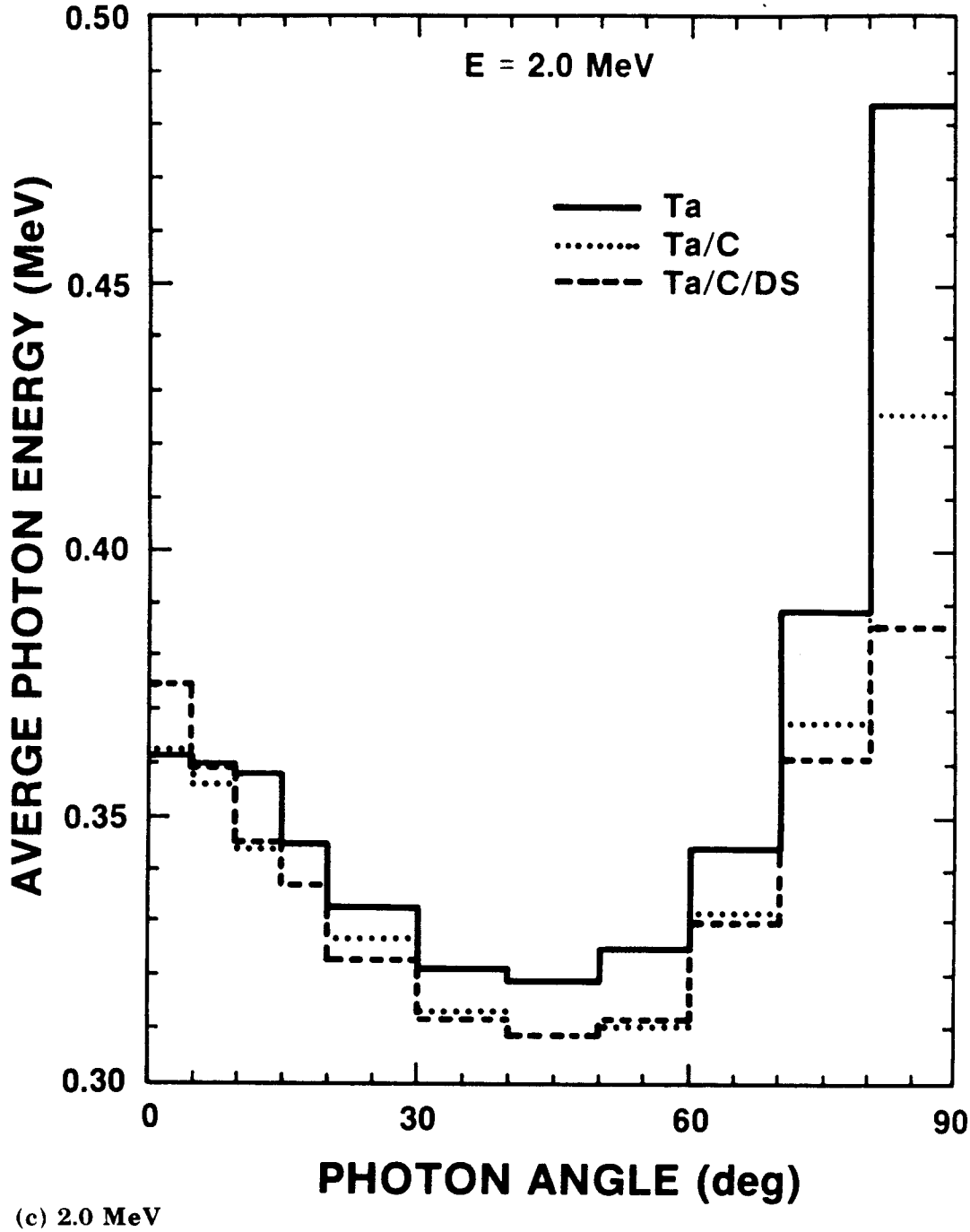

(c) 2.0 MeV

Figure 13. (Continued)

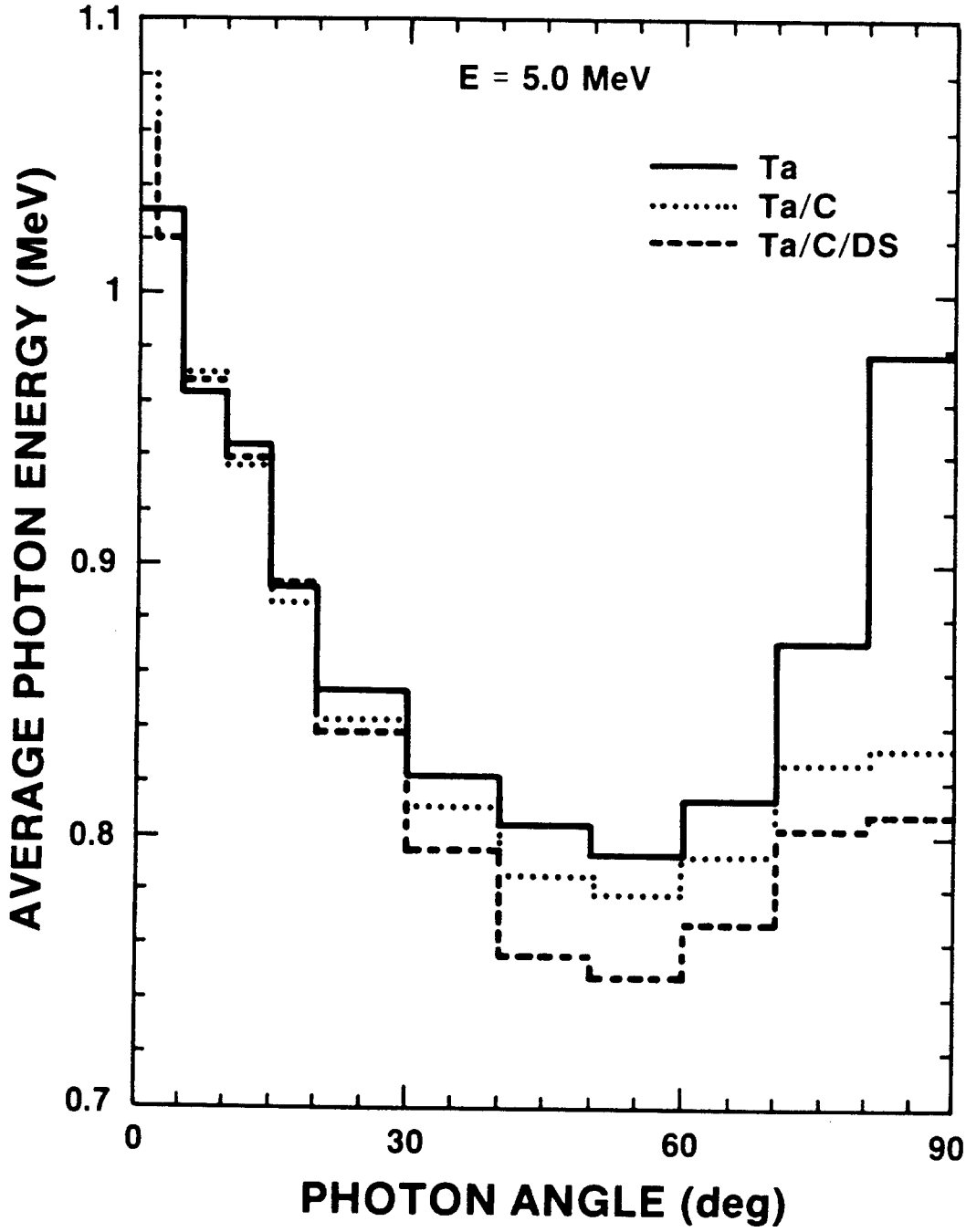

(d) 5.0 MeV

Figure 13. (Continued)

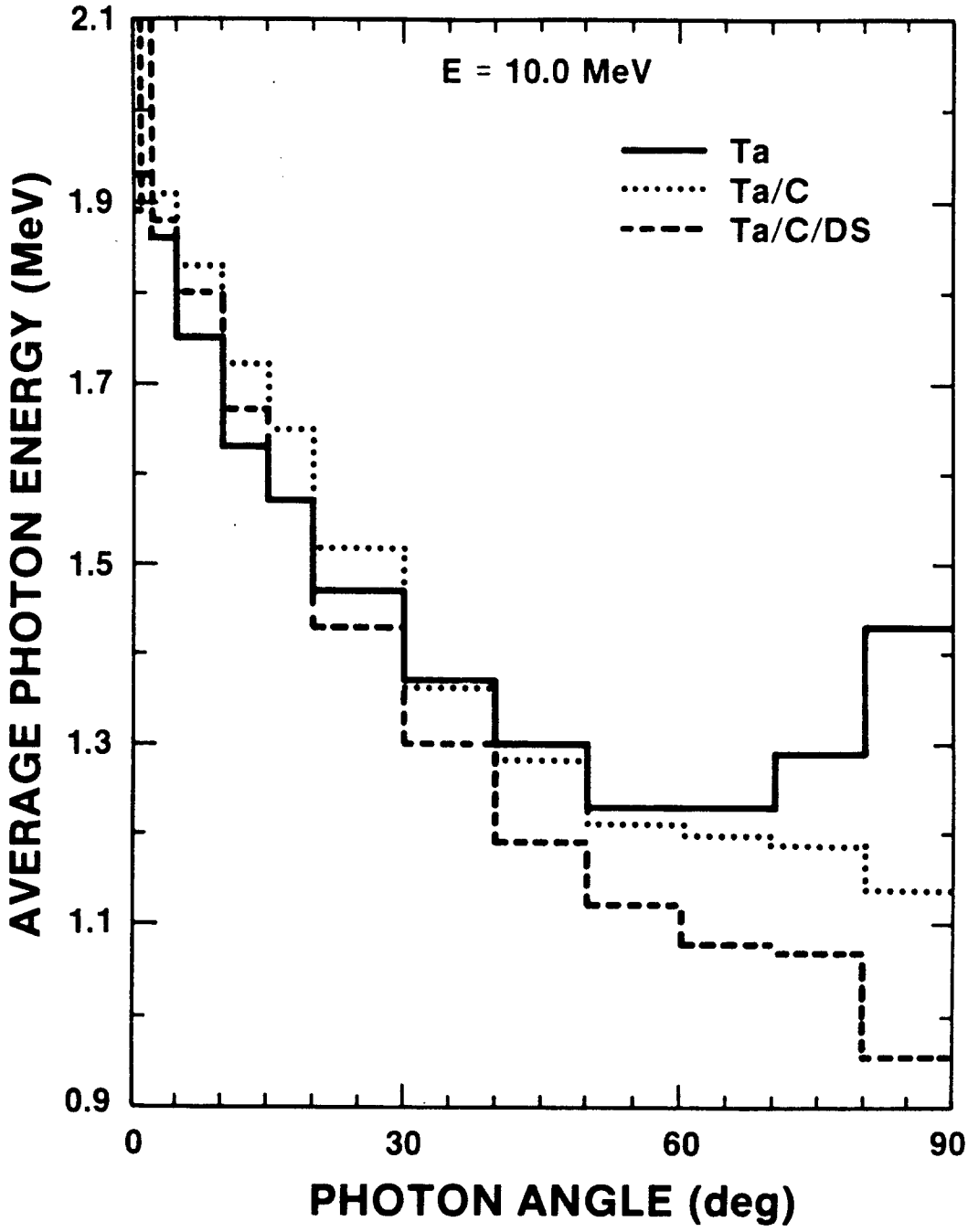

(e) 10.0 MeV

Figure 13. (Continued)

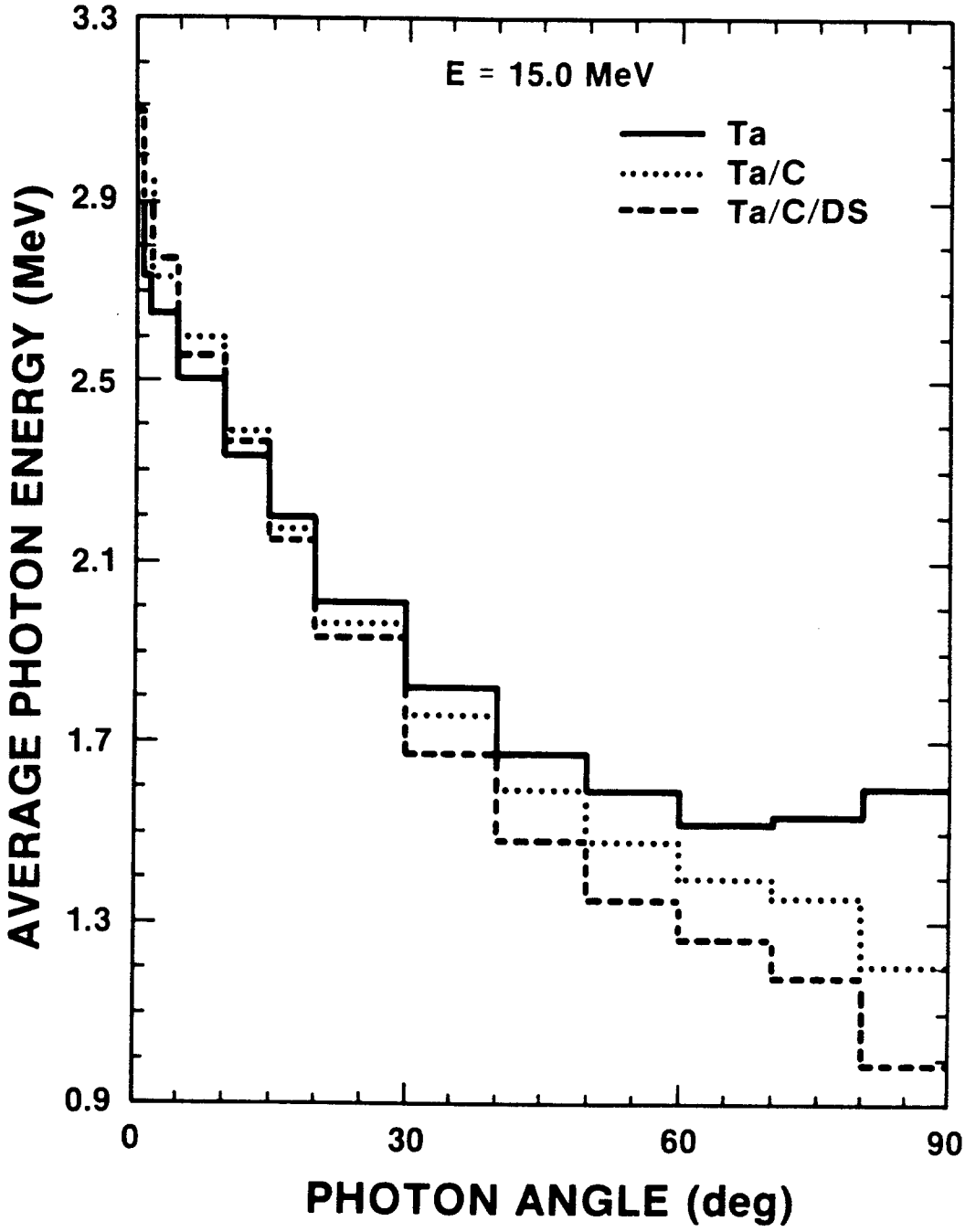

(f) 15.0 MeV

Figure 13. (Concluded)

5. Energy Deposition-μ_{eff}

Although a detailed specification of the radiation field constitutes the most complete description of the radiation environment, dosimetry information is often of immediate practical value. One problem with dosimetry is that it may be too limited. Of particular importance is the necessity of having this information for a variety of materials covering a broad range of atomic numbers. Because experiments are likely to subtend a broad range of solid angles at the converter, spatial information is desirable. We have used the estimators defined by Eqs. (1) through (4) to systematically generate a base of x-ray dosimetry data for the six source-electron energies.

Except where specifically noted, the thicknesses of the optimum Ta converter foils and the graphite electron absorbers are those given in Table 2. In all cases, the combined thickness of these two elements is equal to one CSDA range. For simplicity, the debris shield is simulated by 0.6 g/cm^2 of graphite. However, including the debris shield reduces the forward 2π x-ray energy by no more than 10% and changes the average energy of the x rays by no more than 2%. Consequently, the debris shield is ignored in many calculations.

Table 2. Ta and C Thickness Used in the Standard Optimized Converter*

Electron Energy	Thicknesses*			
	Ta		C	
MeV	r_o	g/cm^2	r_o	g/cm^2
0.5	0.3	0.098	0.7	0.138
1.0	0.3	0.229	0.7	0.342
2.0	0.3	0.480	0.7	0.770
5.0	0.45	1.65	0.55	1.57
10.0	0.6	3.72	0.4	2.24
15.0	0.6	4.86	0.4	3.26

*Note that the sum of Ta plus C is always taken to be one CSDA electron range.

5.1 Deposition on Axis

We have seen from Eq. (3) that the dose in a given material is simply proportional to μ_{eff}, the effective absorption coefficient, for a given photon fluence:

$$D = \mu_{eff} F \ . \tag{5}$$

Accordingly, in the remainder of this section, our energy deposition results will be quoted in terms of μ_{eff}. The utility of μ_{eff} is easily seen. If the dose D_{TLD} is measured in a TLD (thermoluminescence detector), for example, then the dose D_X in any other material X exposed to the same photon fluence can be easily estimated by simply multiplying the TLD dose by the appropriate ratio of effective absorption coefficients:

$$D_X = \frac{\mu_X}{\mu_{TLD}} D_{TLD} \tag{6}$$

The μ_{eff} for radiation in the most forward angle bins is tabulated in Table 3 and plotted in Fig. 14 as a function of source-electron energy for four materials: TLD (CaF_2), air, silicon, and gold. The SD's for the fluences are about 3%. The SD's for the effective absorption coefficients should be much less because Eqs. (1) and (4) show that the dose and fluence are correlated. The CaF_2 material is included because it is the most common TLD dosimeter used in FXR environments. Air was included because doses are often quoted in roengten units, which are defined as 83.8 ergs absorbed per gram of air. This unit is used, for example, in the empirical formula of Martin,[10,11] which gives the on-axis dose in roengtens 1 meter downstream of an optimized converter per coulomb of beam charge Q as:

$$\frac{D}{Q} = 1700\ E^{2.65}\ \text{[roentgens/coulomb]} \tag{7}$$

Here, E is the machine voltage in MV or, equivalently, the kinetic energy of the beam electrons measured in MeV. The other two materials are important for radiation effects work. No debris shield was included in these calculations because its effect is small, as we shall see.

Table 3. Effective Absorption Coefficient μ_{eff} in Units of cm^2/g for Silicon, TLD, Air, and Gold; and the Ratios of μ_{eff} to μ_{eff} for Silicon as a Function of Electron Energy E*

Electron Energy	Angle Interval	Photon Fluence	μ_{eff}				μ_{eff}/μ_{eff} –Silicon		
			Silicon	TLD	Air	Gold	TLD	Air	Gold
MeV	deg	MeV/Str Per Electron	cm^2/g	cm^2/g	cm^2/g	cm^2/g			
0.5	0-10	1.16×10^{-3}	0.132	0.216	0.036	3.61	1.62	0.27	27.2
1.0	0-10	5.25×10^{-3}	0.059	0.083	0.030	1.40	1.42	0.52	23.8
2.0	0-5	3.23×10^{-2}	0.039	0.047	0.029	0.50	1.21	0.74	12.8
5.0	0-2	3.85×10^{-1}	0.026	0.026	0.025	0.080	0.99	0.07	3.1
10.0	0-1	3.34×10^{0}	0.023	0.023	0.022	0.043	0.99	0.94	1.9
15.0	0-1	1.18×10^{1}	0.022	0.022	0.019	0.042	0.99	0.89	1.9

*All coefficients correspond to the total fluence and average dose calculated for the forward angular bin indicated in the second column. No debris shield is assumed.

Above 5.0 MeV, the μ_{eff} for gold approaches 0.04 cm^2/g and that of the other three materials approaches 0.02 cm^2/g (Fig. 14). The μ_{eff} or equivalently the dose in the other three materials relative to that in silicon are tabulated in Table 3 and are plotted in Fig. 15. We see that the doses in silicon, air, and TLD are equivalent to one another to better than 10% for source electrons with energies in excess of 5.0 MeV.

The magnitude of μ_{eff} can be intuitively understood by noting the value of the absorption coefficient at the corresponding average photon energy. In silicon, for example, the ratio of μ_{eff} to the absorption coefficient at the average photon energy (see Fig. 6) is plotted in Fig. 16. At a source energy of 1.0 MeV, μ_{eff} is twice the value of the absorption coefficient at the average photon energy. Above a source energy of 3.0 MeV, where also the bulk of the photons generated are in an energy region where Compton scattering dominates over the photon-electric cross sections, the two coefficients agree to better than 10%.

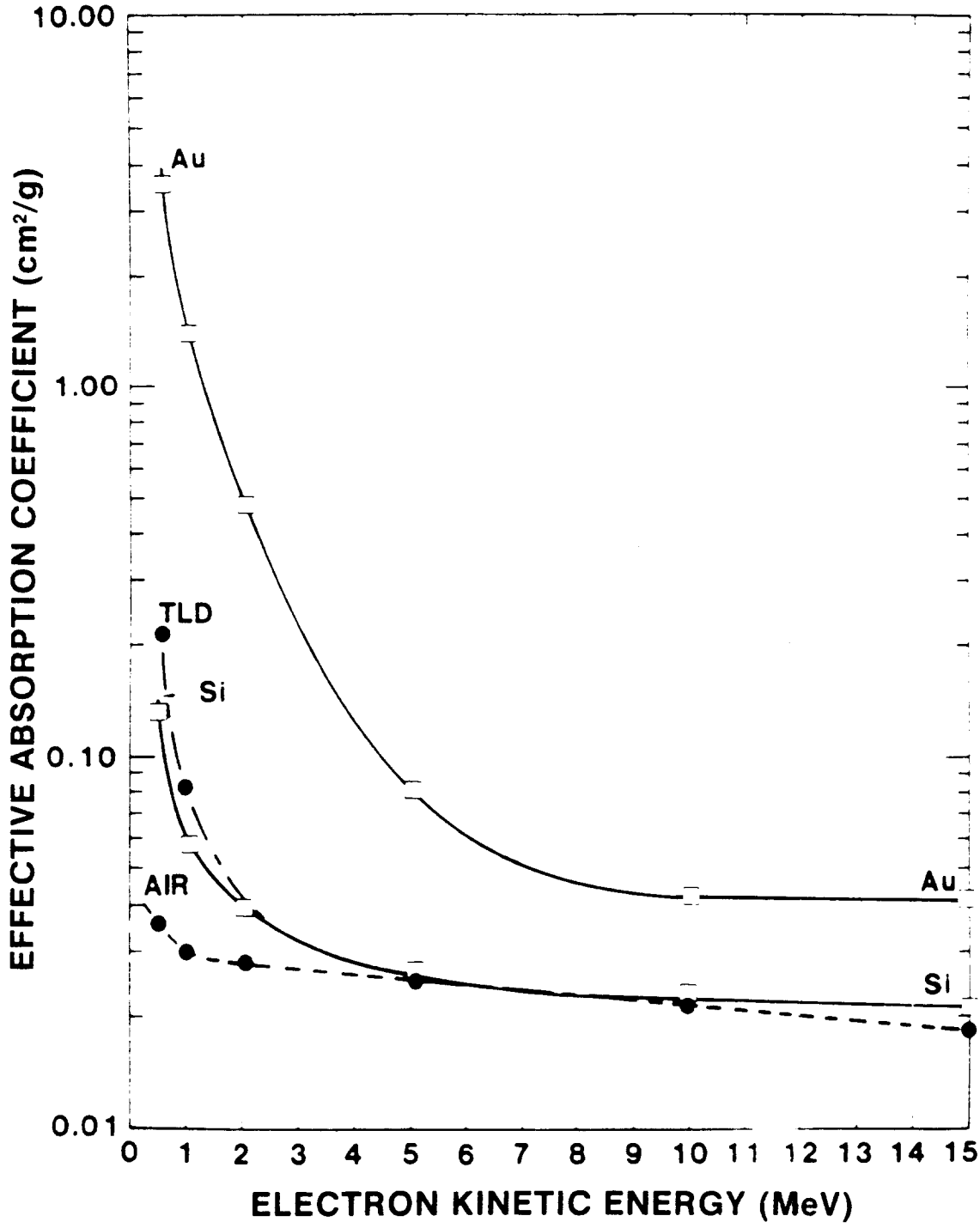

Figure 14. Effective Absorption Coefficient as a Function of Incident Electron Energy for Four Materials – No Debris Shield

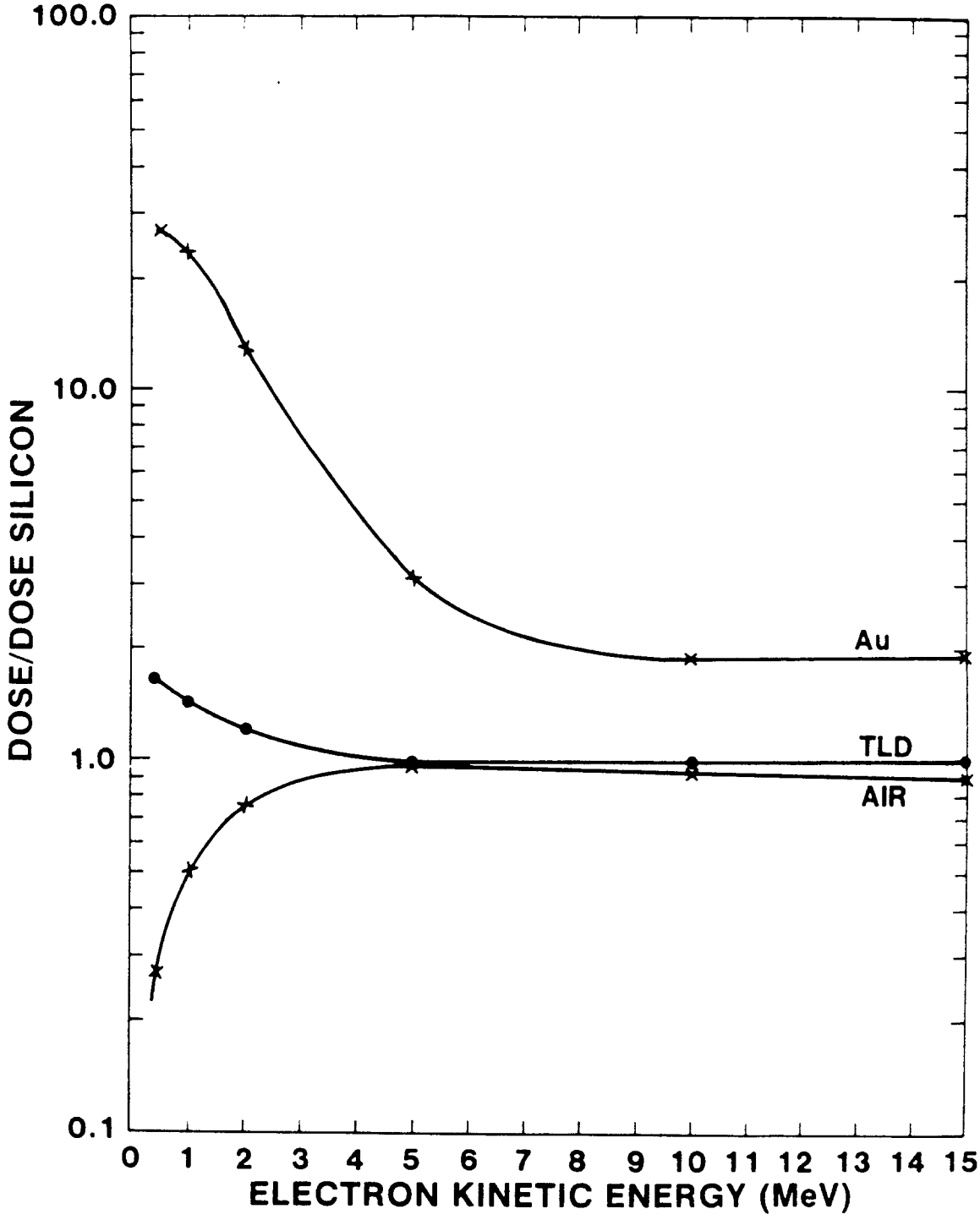

Figure 15. Ratio of Doses in Three Materials to Dose in Silicon as a Function of Incident Electron Energy – No Debris Shield

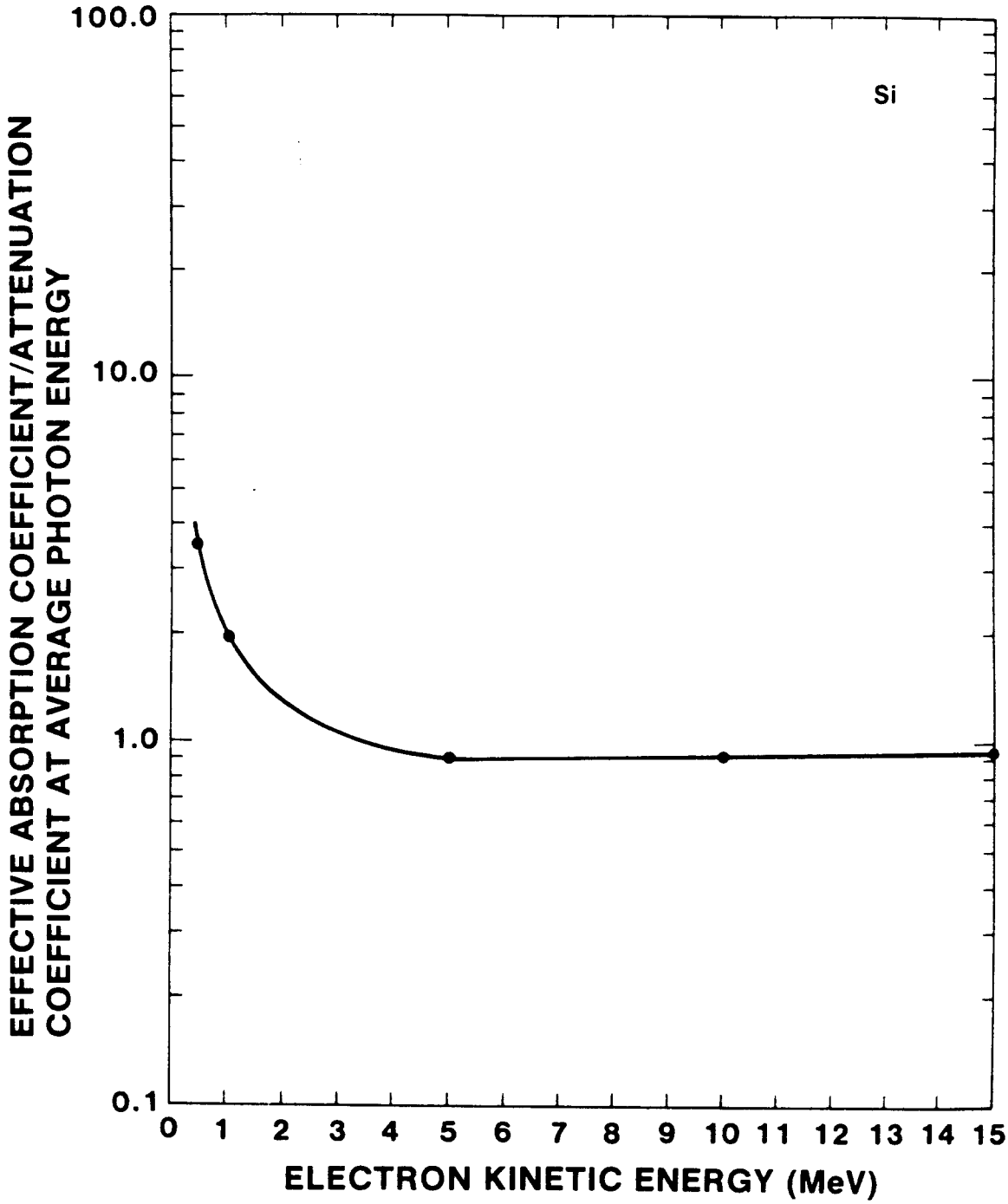

Figure 16. Ratio of the Effective Absorption Coefficient to the Absorption Coefficient at the Average Photon Energy for Silicon as a Function of Incident Electron Energy – No Debris Shield

For Silicon, below 5.0 MeV the effect on μ_{eff} of adding the debris shield is to reduce μ_{eff} by less than 8%; above 5.0 MeV, the effect is to reduce μ_{eff} 2%. Below 5.0 MeV, the effect of adding the shield on the ratio μ_{eff} (gold)/μ_{eff} (silicon) is to increase the ratio by less than 13%; above 5.0 MeV, the effect is to increase the ratio by less than 0.5%.

As an example of the utility of μ_{eff}, let us use Eq. (5) to estimate the expected on-axis dose in air 1 meter from an optimized converter for 1 coulomb of charge incident at 1 MeV and 10 MeV, and compare our result with that expected from the Martin relation, Eq. (7). From Column 3 of Table 3, or from Fig. 26, we see that the approximate on-axis fluence at 1 MeV is 5.24 x 10^{-3} MeV/Str/electron, or 5.24 $\times$ 10^6 ergs/cm^2/C at 1 meter.

Now, from Column 6 of Table 3, μ_{eff} in air at 1 MeV is 0.30 cm^2/gm. Thus, the approximate on-axis dose at 1 meter is

$$D = 0.030\ [cm^2/g] \times 5.24 \times 10^6\ [ergs/cm^2\text{-}C] = 1.6 \times 10^5\ [ergs/g\text{-}C]\ .$$

In roentgen units, the dose is

$$D = 1.6 \times 10^5\ [ergs/g\text{-}C] \times \frac{1}{83.8}\ [R\text{-}g/ergs] = 1.9 \times 10^3\ [R/C]\ .$$

The dose expected from the Martin equation is

$$D = 1700 \times 1^{2.65} = 1.7 \times 10^3\ [R/C]\ ,$$

which is only 10% lower than our calculation. Repeating the same process at 10 MeV, the calculated dose is 8.77 $\times$ 10^5 R/C, and that expected from the Martin equation is 7.59 $\times$ 10^5 R/C. Again, the Martin result is slightly (13%) lower than our calculation.

At 10 MeV, there is little difference between μ_{eff} for the low-Z materials (Fig. 14), so that we see that our calculated on-axis dose for air also agrees with that shown in Fig. 32 for silicon. Finally, this example illustrates not only how μ_{eff} can be used in evaluating a dose once the fluence is known, but also that the calculations are in reasonable agreement with previous experimental results.

5.2 Deposition as a Function of X-Ray Emission Angle

The angular dependence of the μ_{eff} in silicon is shown in Fig. 17 for the four of the six source energies. μ_{eff} remains relatively independent of emission angle up to the angle of half height at which angle the photon fluence has decreased to half its zero-degree value. At larger angles, μ_{eff} decreases rapidly for low source-electron energies. The corresponding data for gold is shown in Fig. 18. In contrast to the silicon results, the gold coefficients increase with emission angle at small angles and especially at high energy. Thus, the ratio of the dose to gold to that in silicon shows a variation with emission angle similar to that of μ_{eff} in gold. This ratio is plotted in Fig. 19. At a given electron energy the maximum value for angles less than the angle at half height is no more than 30% greater than the value at zero degrees.

The variation of μ_{eff} with emission angle arises from the variation in photon spectrum with angle and the fact that μ_{eff} depends inversely on photon energy. For example, Figs. 13b and 13e are plots of the average photon energy as a function of emission angle for 1.0 and 10.0 MeV, respectively. The broad peak in μ_{eff} for gold at 1.0 MeV occurs at about the same angle as the minimum average photon energy in Fig. 13b. The steep rise in μ_{eff} for gold at 10.0 MeV corresponds to the steep fall in the average photon energy in Fig. 13e.

As discussed in Sec. 4.3, the dependence of the average photon energy on angle is not easily understood. We know from the production cross section that the average energy of the photon spectrum decreases with production angle. However, x rays emitted from thick targets at large angles must traverse a relatively large slant thickness compared with more forward emission. Except for the highest energy sources, the spectra at these high emission angles are hardened due to absorption of low-energy photons (compare Fig. 13a with Fig. 13f). At the highest source energies and especially for configurations involving the low-Z electron absorbers and debris shields, the emission spectra at high emission angles appear to be softened due to buildup of scattered photons (Fig. 13f).

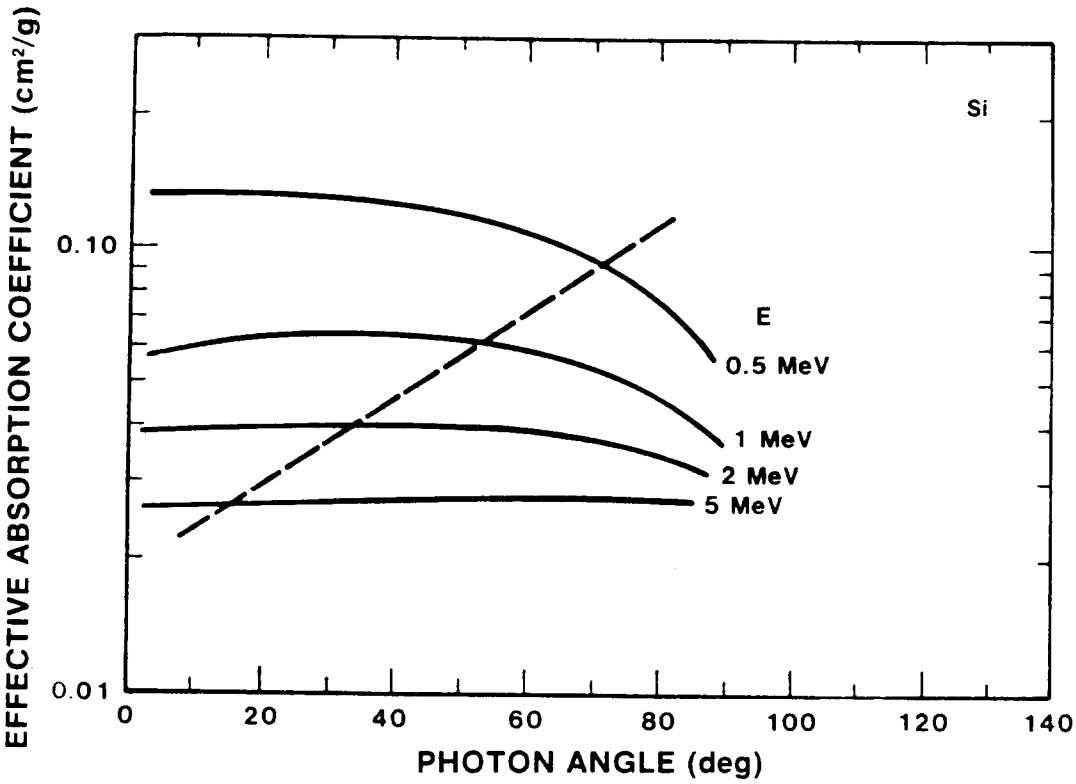

Figure 17. Effective Absorption Coefficient for Silicon vs Angle of X-Ray Emission for Four Electron Energies – No Debris Shield (Dashed line denotes the approximate half angle of the fluence distribution)

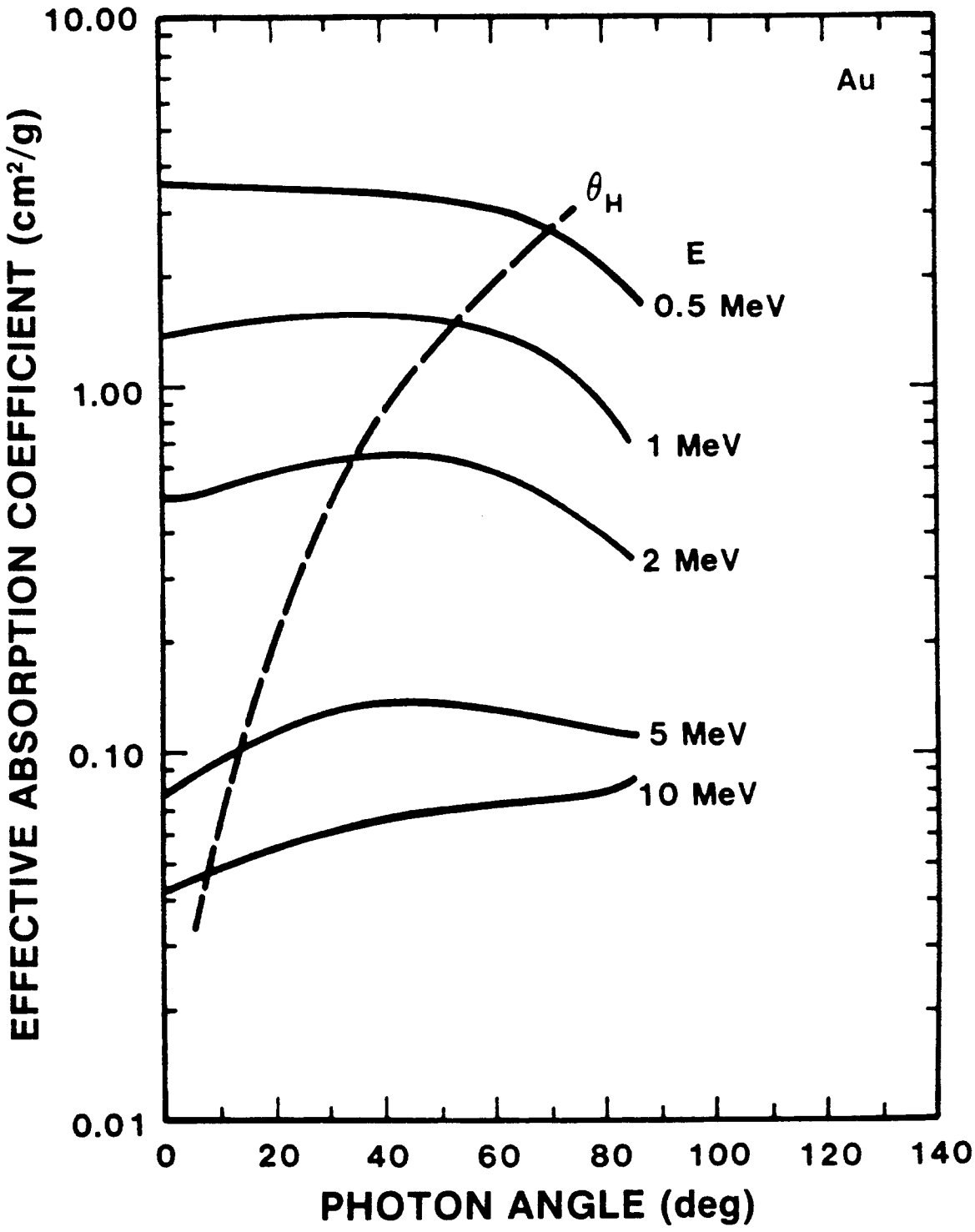

Figure 18. Effective Absorption Coefficient for Gold vs Angle of X-Ray Emission for Five Electron Energies – No Debris Shield (Dashed line denotes the approximate half angle of the fluence distribution)

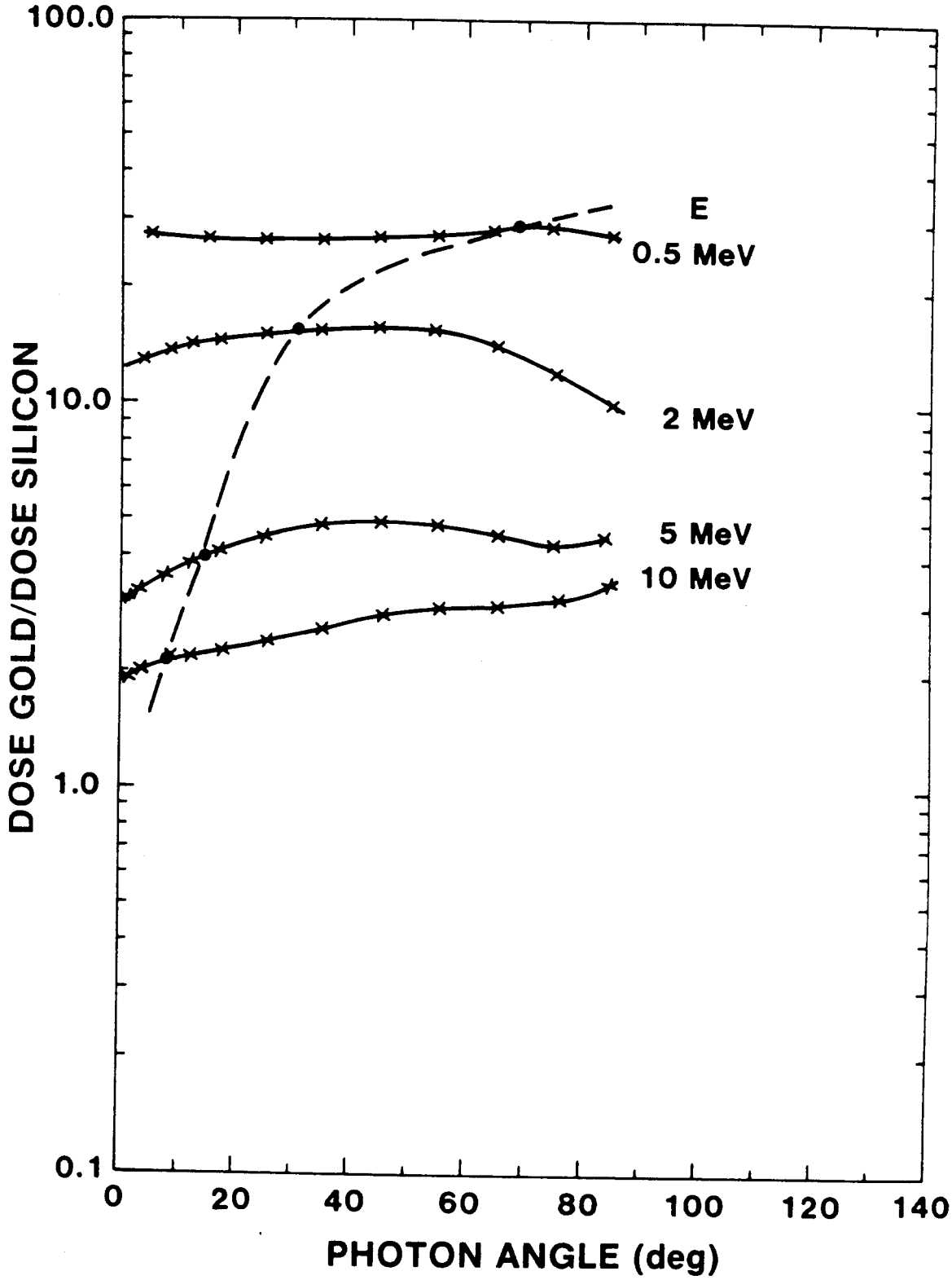

Figure 19. Ratio of Dose-to-Gold to Dose-to-Silicon as a Function of Angle of X-Ray Emission for Four Electron Energies – No Debris Shield (Dashed line denotes the approximate half angle of the fluence distribution)

5.3 Dose Optimization

In silicon, for the radiation in the forwardmost angle bin, the dependence of μ_{eff} on the fraction of the tantalum in the Ta/C converter is shown in Fig. 20. The source electron energies are 1.0 and 10.0 MeV. At 1.0 MeV, the coefficient increases with decreasing fraction. This trend is expected because as the tantalum fraction decreases, low-energy photons can more easily escape from the converter. A 30% change in the foil thickness at the optimum value of 0.3 r_0 results in a 30% change in the silicon coefficient; the corrresponding change in the ratio of the gold coefficient to the silicon coefficient is less than 5% as can be seen in Fig. 21. At 10.0 MeV, Fig. 20 shows that there is little change in the silicon coefficient over a large range of tantalum fractions.

The relatively strong dependence of the silicon coefficient on tantalum fraction at 1.0 MeV and the lack of that dependence at 10.0 MeV are easily understood by examining the average photon energy as a function of tantalum fraction. In Fig. 22, we see that this energy decreases from 0.183 to 0.099 MeV as the foil thickness decreases from 0.3 to 0.001 r_0 for a source energy of 1.0 MeV. At this source energy a significant fraction of the photons *generated* have energies in the highly absorptive photoelectric region where the absorption coefficient has a strong inverse dependence on photon energy. At 10.0 MeV, on the other hand, Fig. 22 shows that even though the average energy decreases from 1.4 to 0.63 MeV as the tantalum thickness decreases from 0.6 to 0.001 r_0, the bulk of the photon energy generated falls in an energy range where incoherent scattering dominates. Energy absorption coefficients are relatively constant over this energy range.

The strong dependence of μ_{eff} on the thickness of the tantalum fraction at a source energy of 1.0 MeV means that the fraction that maximizes energy fluence may not be the same fraction that maximizes the energy deposition. For example, Figs. 23 and 24 show that the total forward fluence and the fluence in selected emission angle intervals within the forward 2π solid angle for a source energy of 1.0 MeV are maximized for a tantalum thickness of 0.3 r_0. However, the silicon dose curves in Fig. 25 indicate that the maximum dose occurs for thinner foils. This effect is more pronounced at forward angles. It is demonstrated further in Figs. 26 and 27. In Fig. 26, we see that the photon fluence is significantly reduced over almost all emission angles for a foil thickness of 0.05 r_0 as compared with the fluence for the optimum thickness. In Fig. 27, on the other hand, we see that the silicon dose for the smaller foil thickness is higher at all emission angles less than 70° than that obtained for the thickness that maximizes the fluence. The large difference between the optimum thicknesses for fluence and dose at low source energies arises from the fact that the absorption is a strongly decreasing function of photon energy for these low-energy spectra. At the higher source energies, Figs. 28 through 32 show that dose and fluence are maximized by approximately the same tantalum fractions.

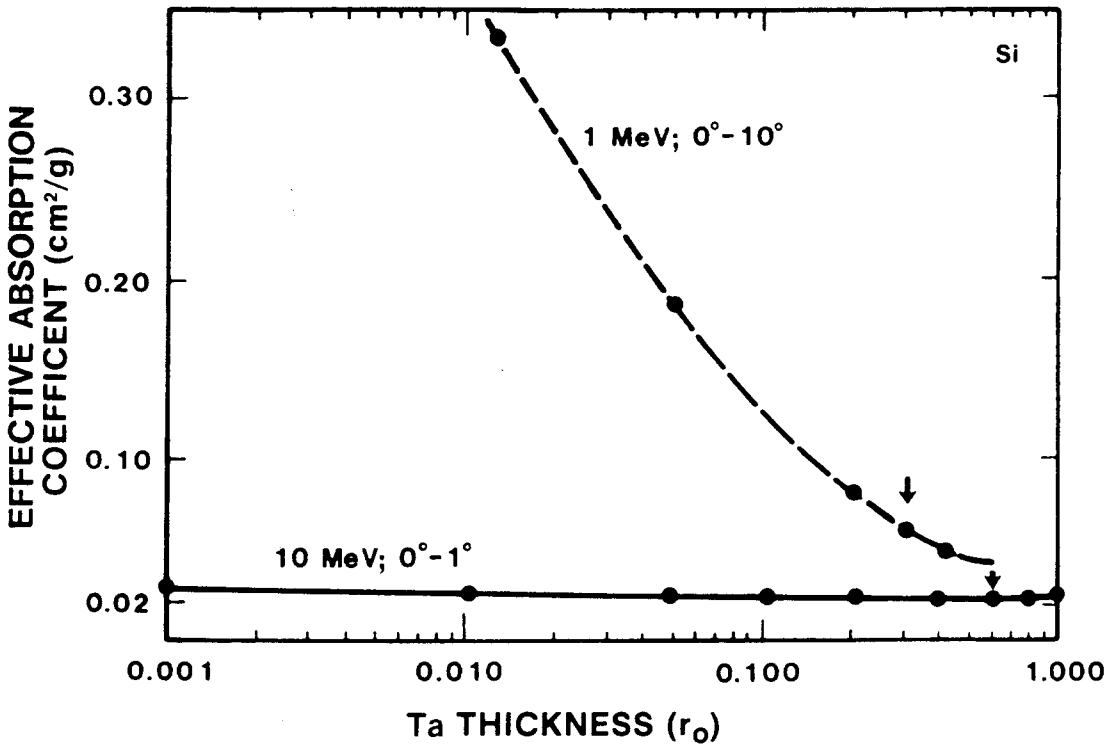

Figure 20. Effective Absorption Coefficient in Silicon for Forward-Directed Radiation as a Function of the Thickness of the Tantalum Converter Foil for 1.0 and 10.0 MeV Electron Energies

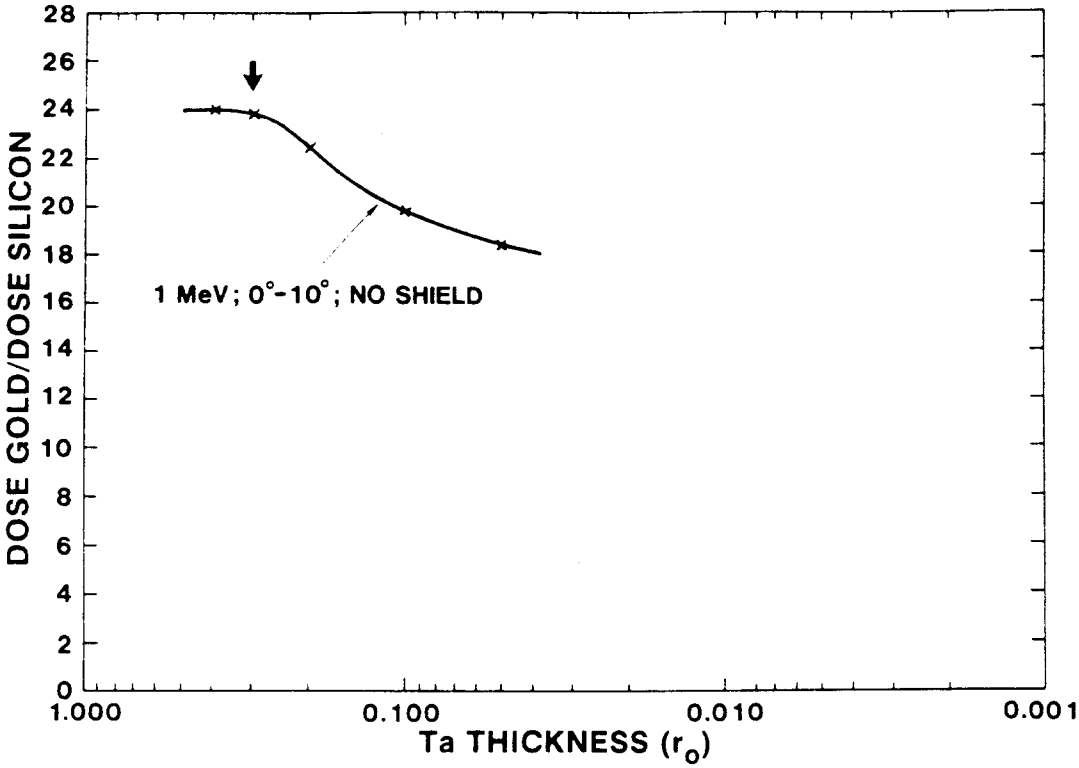

Figure 21. Ratio of Dose-to-Gold to Dose-to-Silicon for Forward-Directed Radiation as a Function of the Thickness of the Tantalum Converter Foil for 1.0 MeV Electron Energies

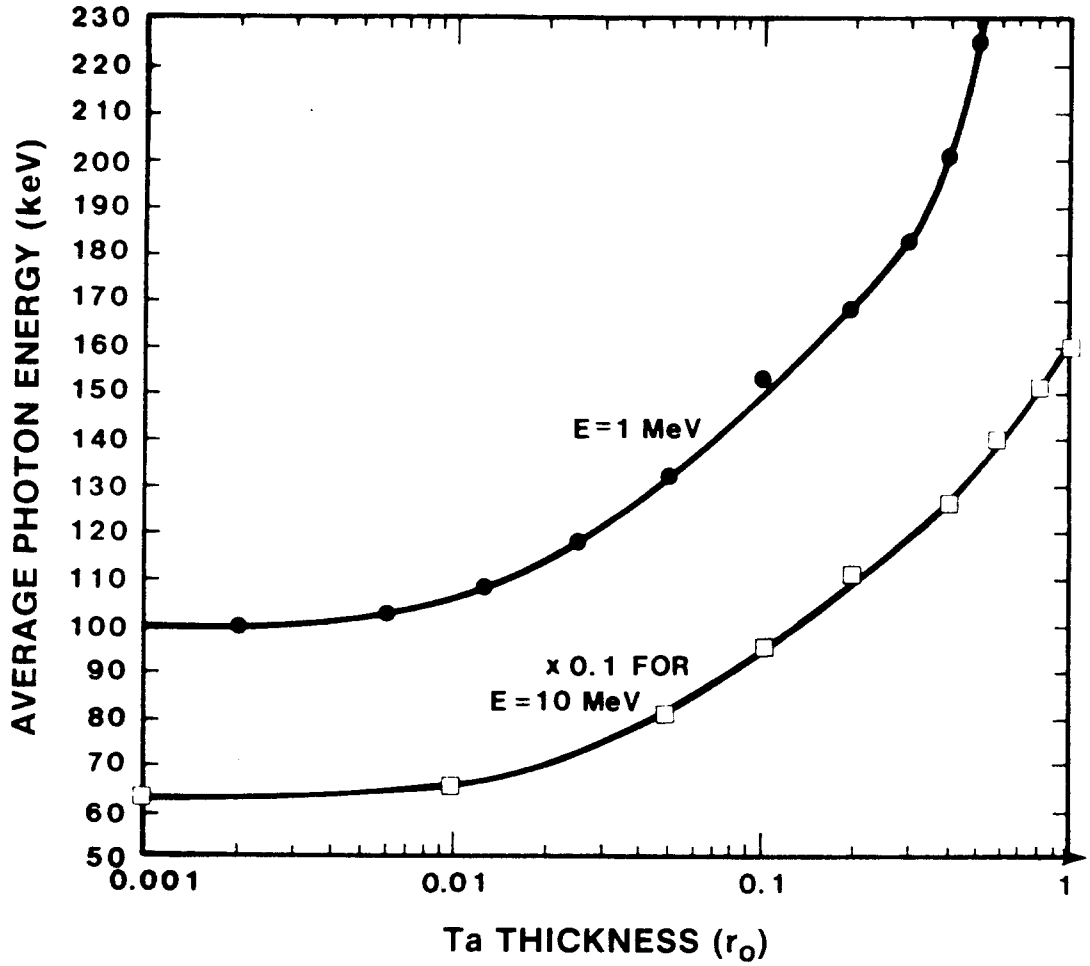

Figure 22. Average Photon Energy for Forward-Directed Radiation as a Function of the Thickness of the Tantalum Converter Foil for 1.0 and 10.0 MeV Electron Energies – 0.17 in. Kevlar Debris Shield

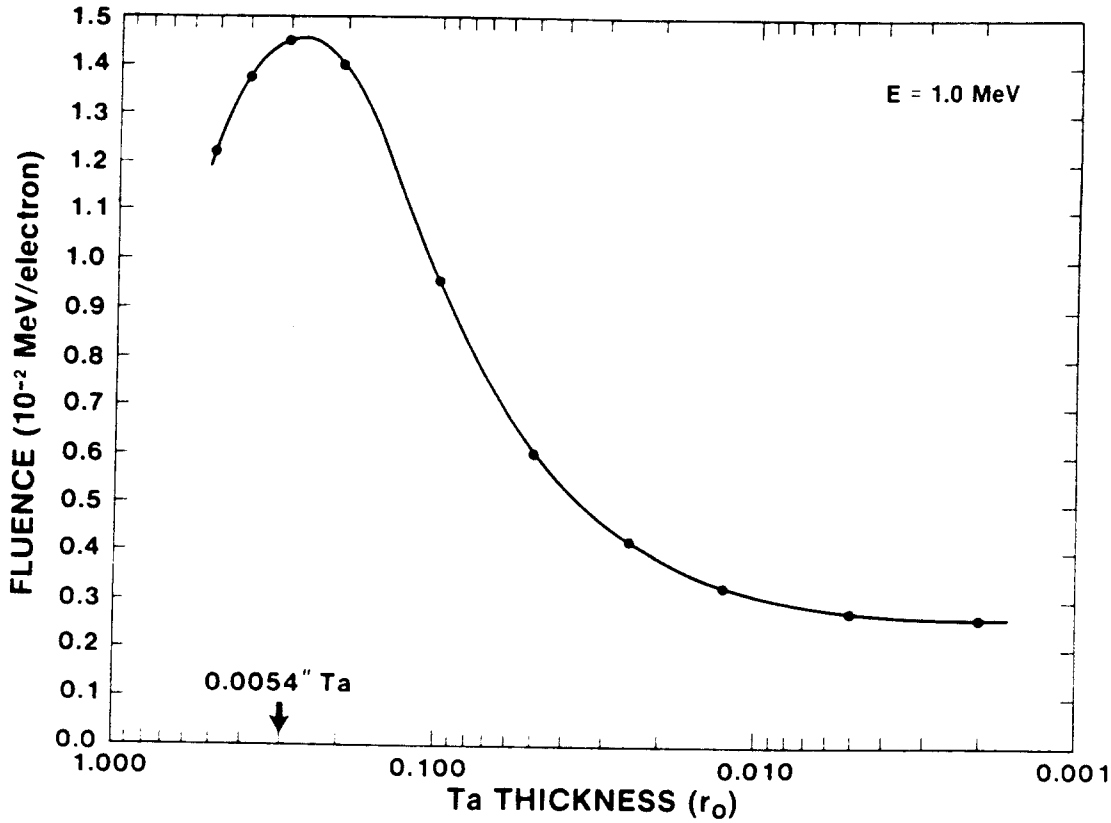

Figure 23. Total Fluence of Forward-Directed Radiation as a Function of the Thickness of the Tantalum Converter Foil for 1.0 MeV Electron Energies – 0.17 in. Kevlar Debris Shield

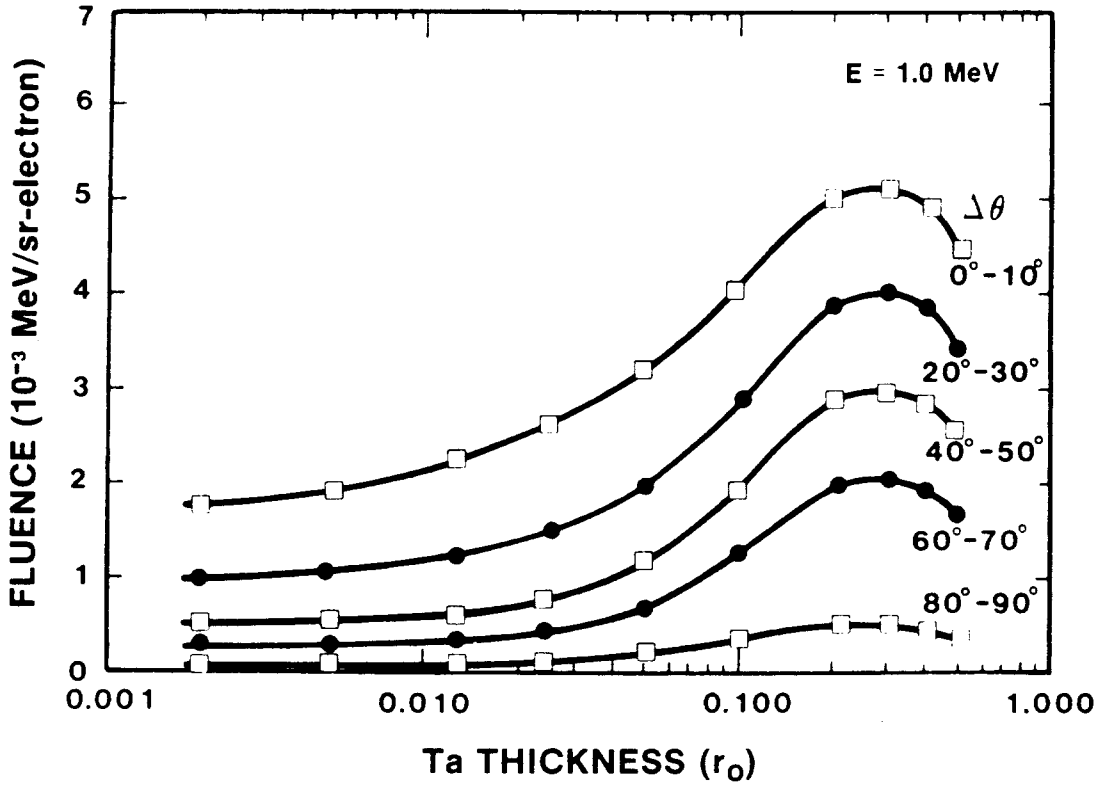

Figure 24. Fluence in Selected Angle Bins as a Function of the Thickness of the Tantalum Converter Foil for 1.0 MeV Electron Energies – 0.17 in. Kevlar Debris Shield

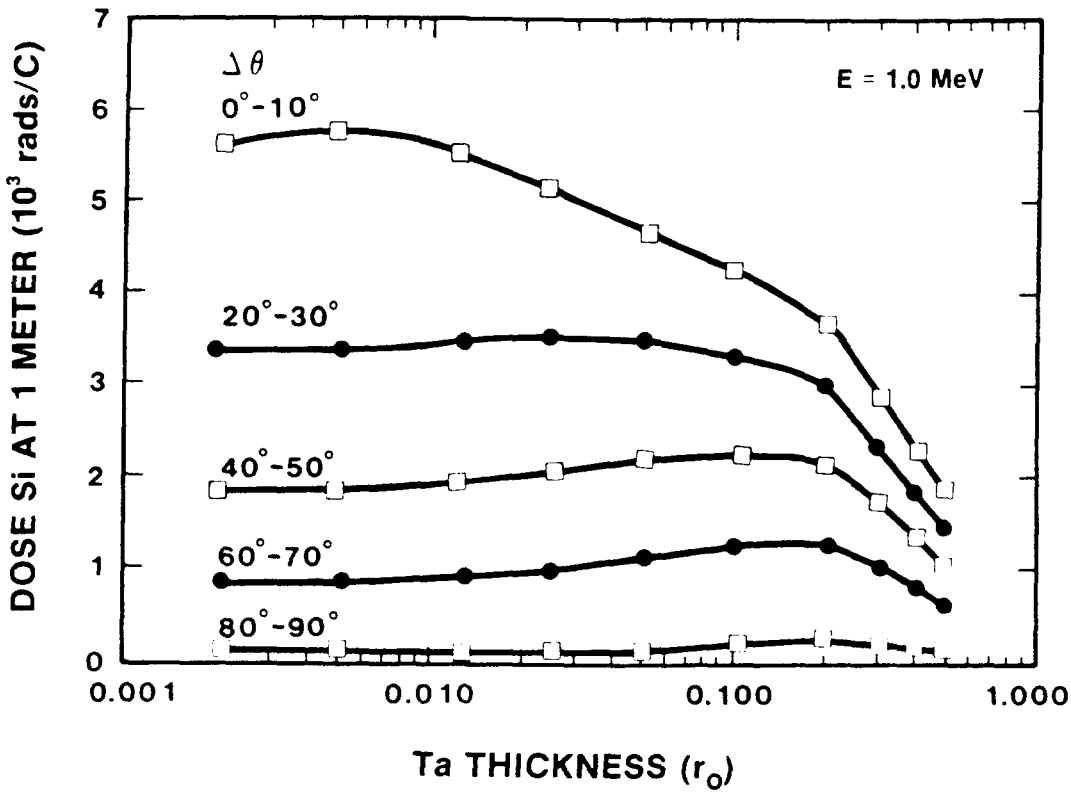

Figure 25. Dose-to-Silicon in Selected Angle Bins at a Distance of 1-Meter from the Converter as a Function of the Thickness of the Tantalum Converter Foil for 1.0 MeV Electron Energies – 0.17 in. Kevlar Debris Shield

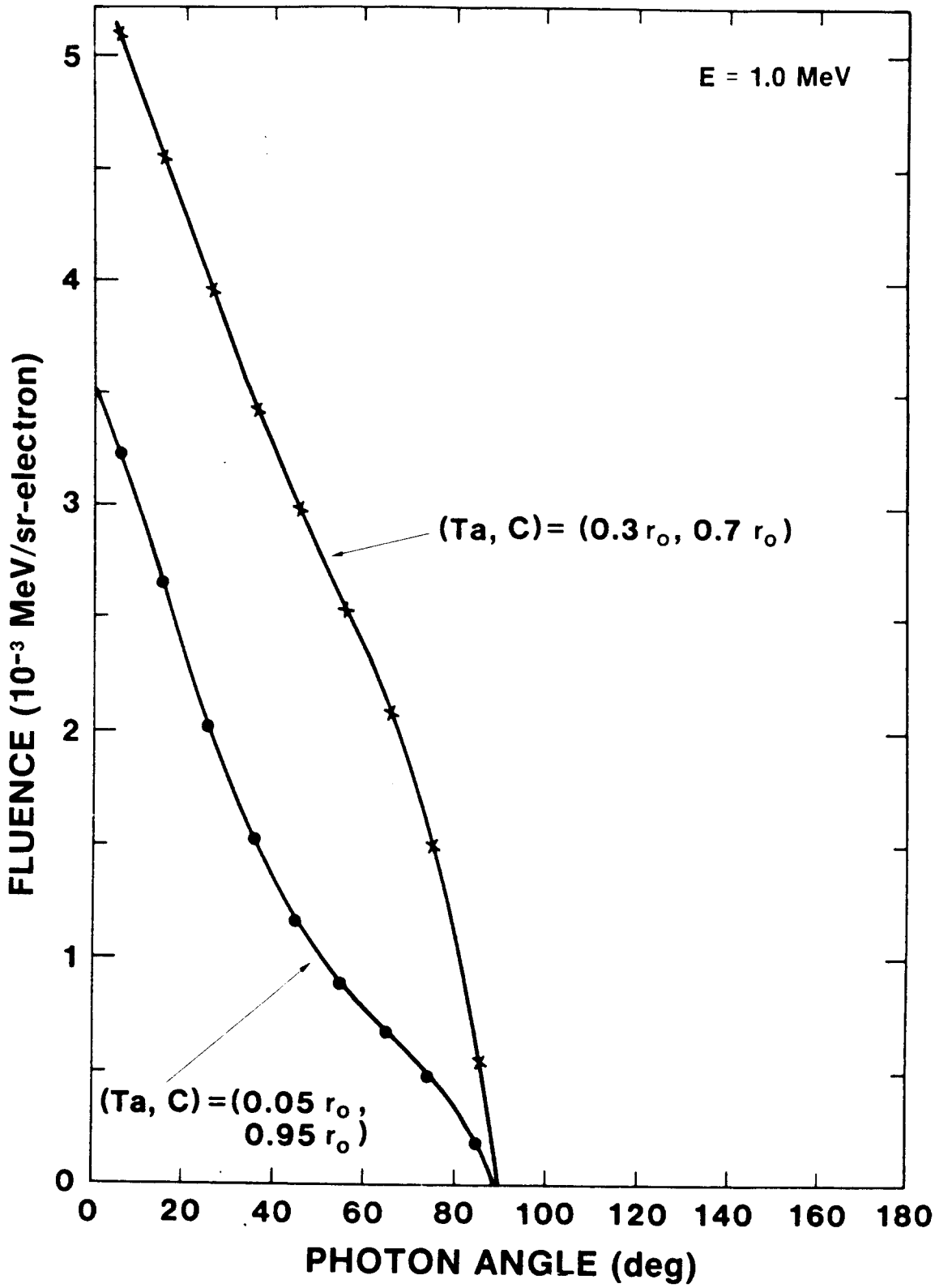

Figure 26. Energy Fluence as a Function of X-Ray Emission Angle for Two Converter Configurations and for 1.0 MeV Electrons – 0.17 in. Kevlar Debris Shield

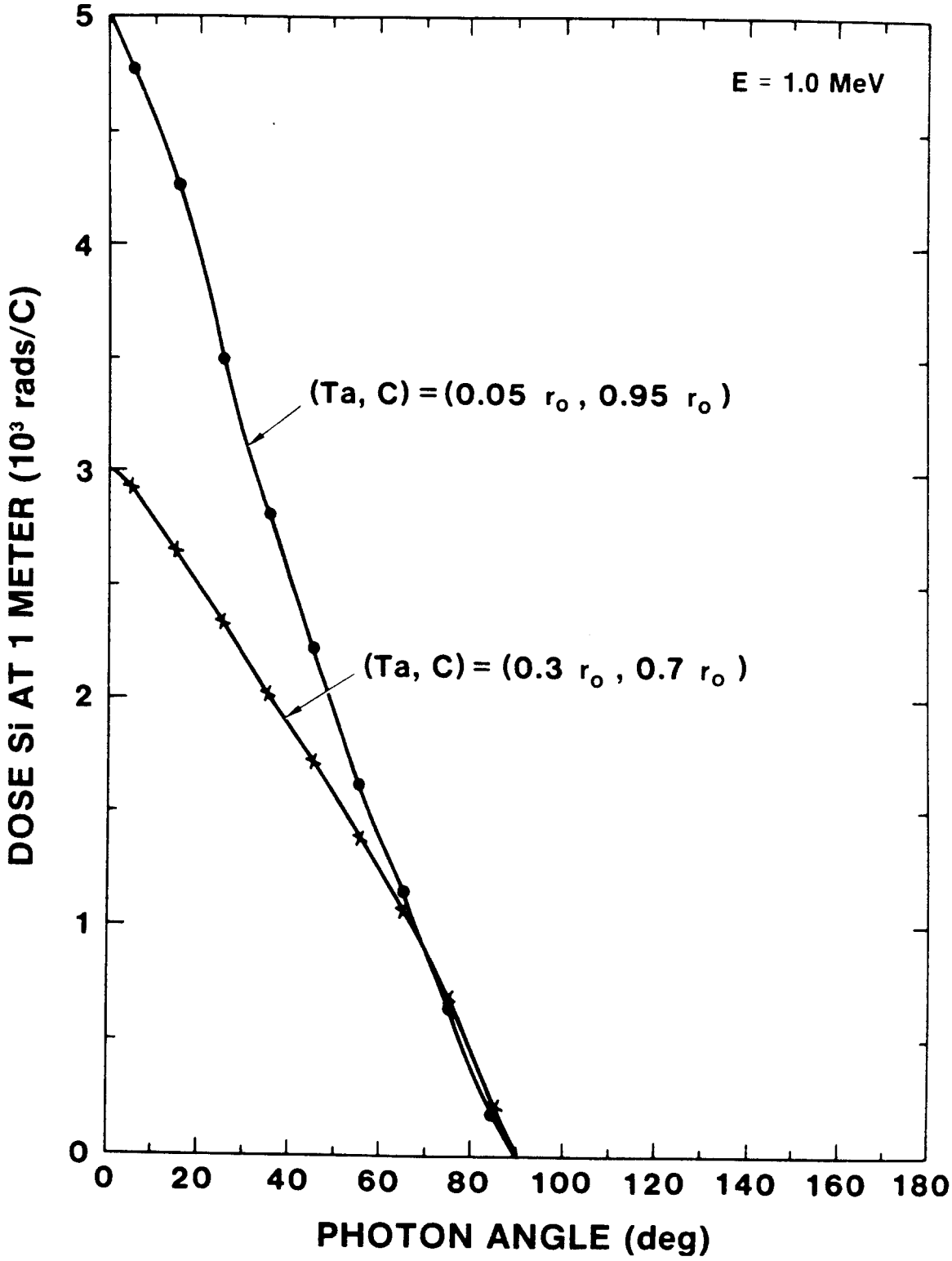

Figure 27. Dose-to-Silicon at a Distance of 1-Meter From the Converter as a Function of X-Ray Emission Angle for Two Converter Configurations and for 1.0 MeV Electrons – 0.17 in. Kevlar Debris Shield

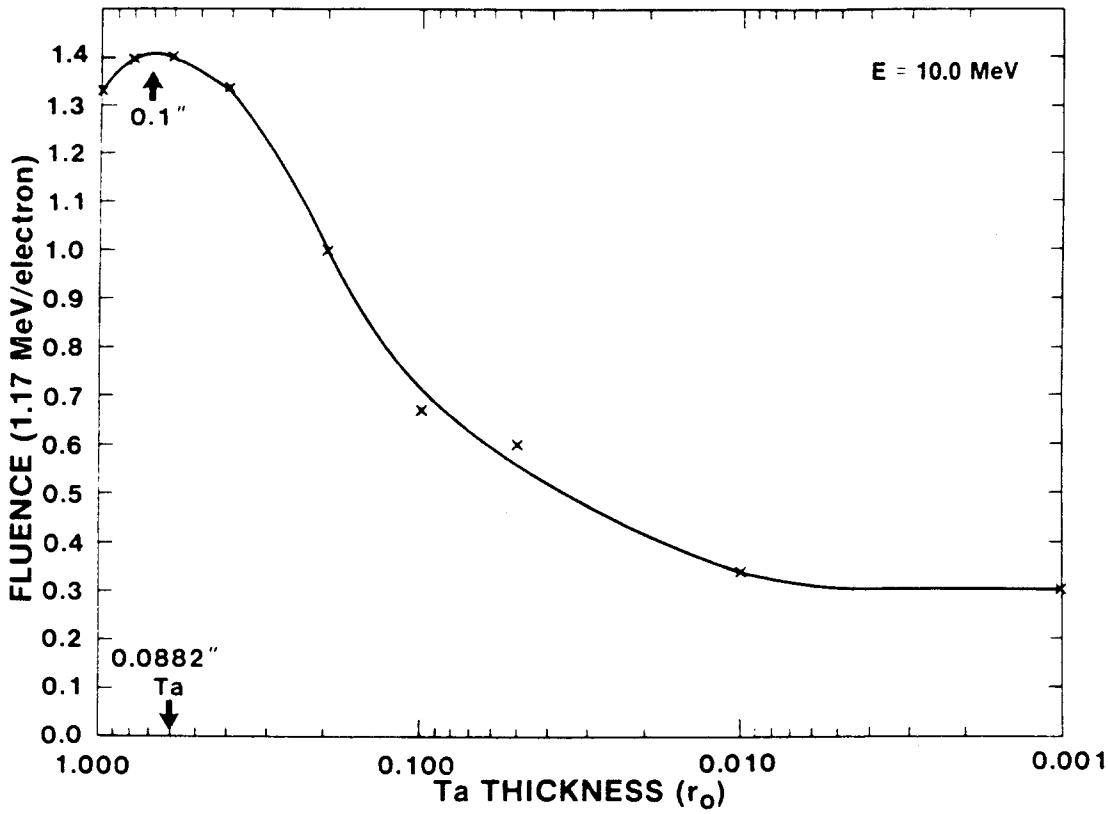

Figure 28. Total Fluence of Forward-Directed Radiation as a Function of the Thickness of the Tantalum Converter Foil for 10.0 MeV Electron Energies – 0.17 in. Kevlar Debris Shield

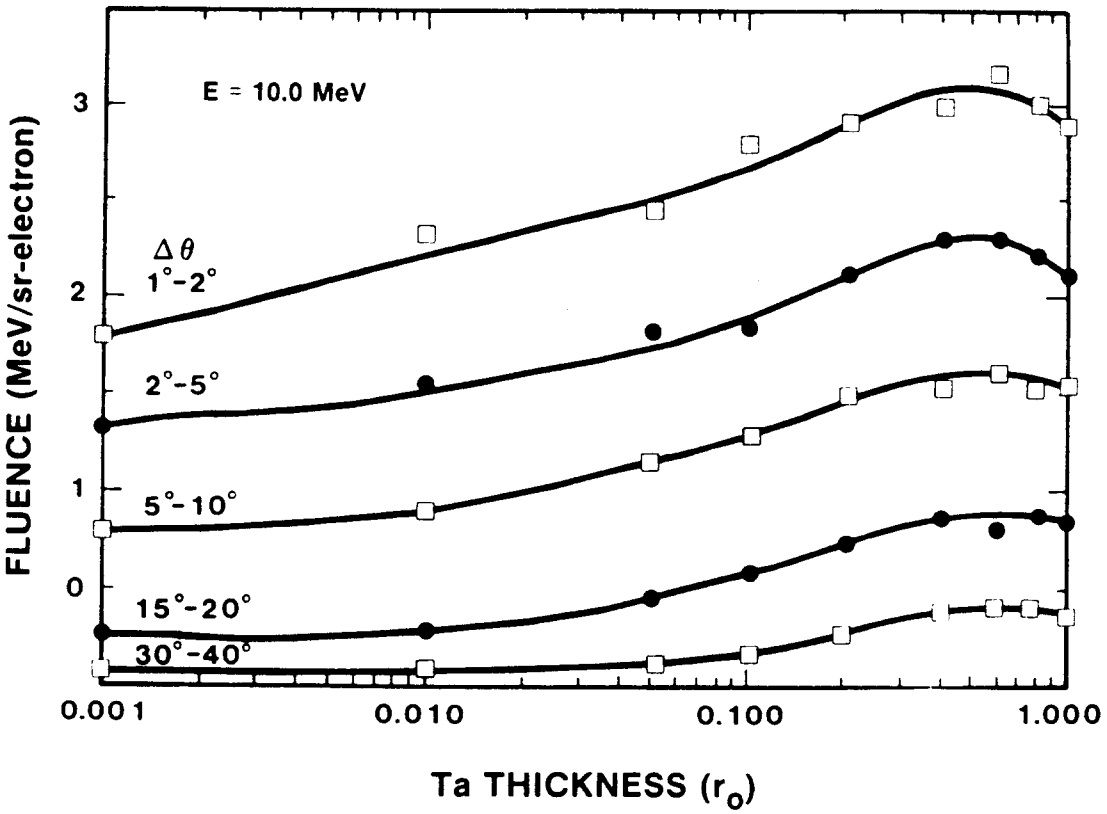

Figure 29. Fluence in Selected Angle Bins as a Function of the Thickness of the Tantalum Converter Foil for 10.0 MeV Electron Energies – 0.17 in. Kevlar Debris Shield

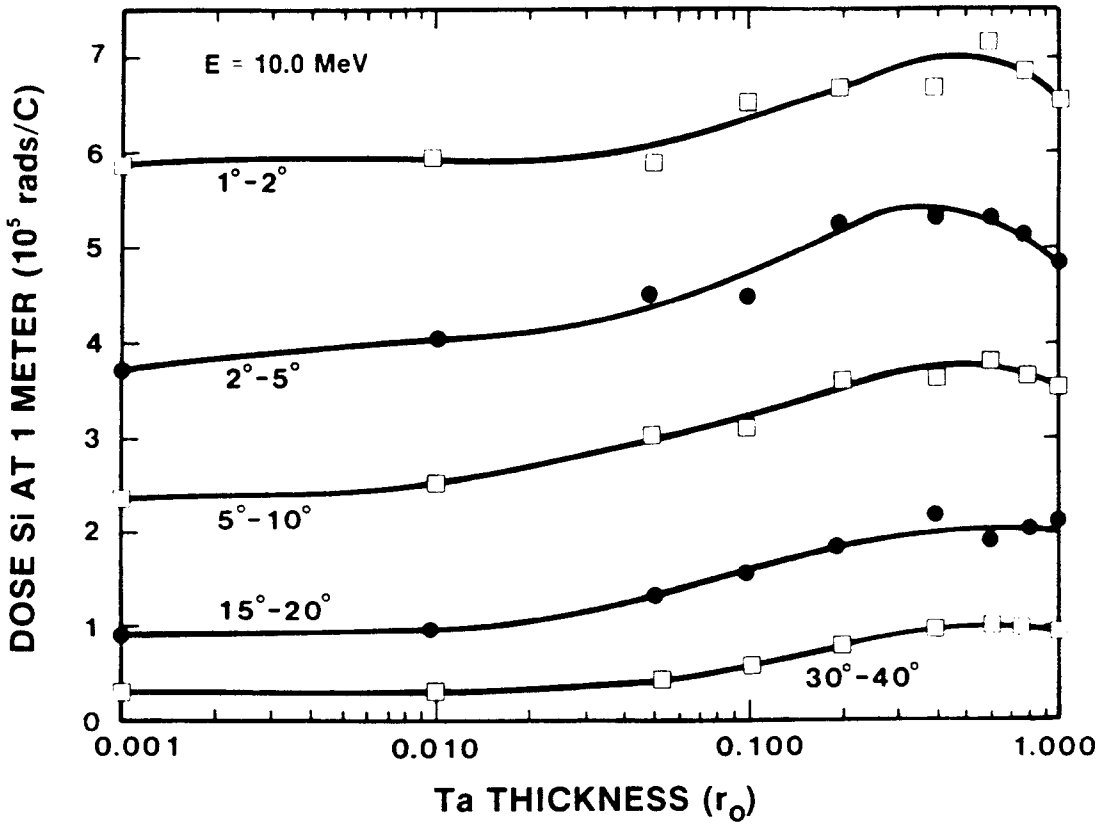

Figure 30. Dose-to-Silicon in Selected Angle Bins at a Distance of 1-Meter from the Converter as a Function of the Thickness of the Tantalum Converter Foil for 10.0 MeV Electron Energies – 0.17 in. Kevlar Debris Shield

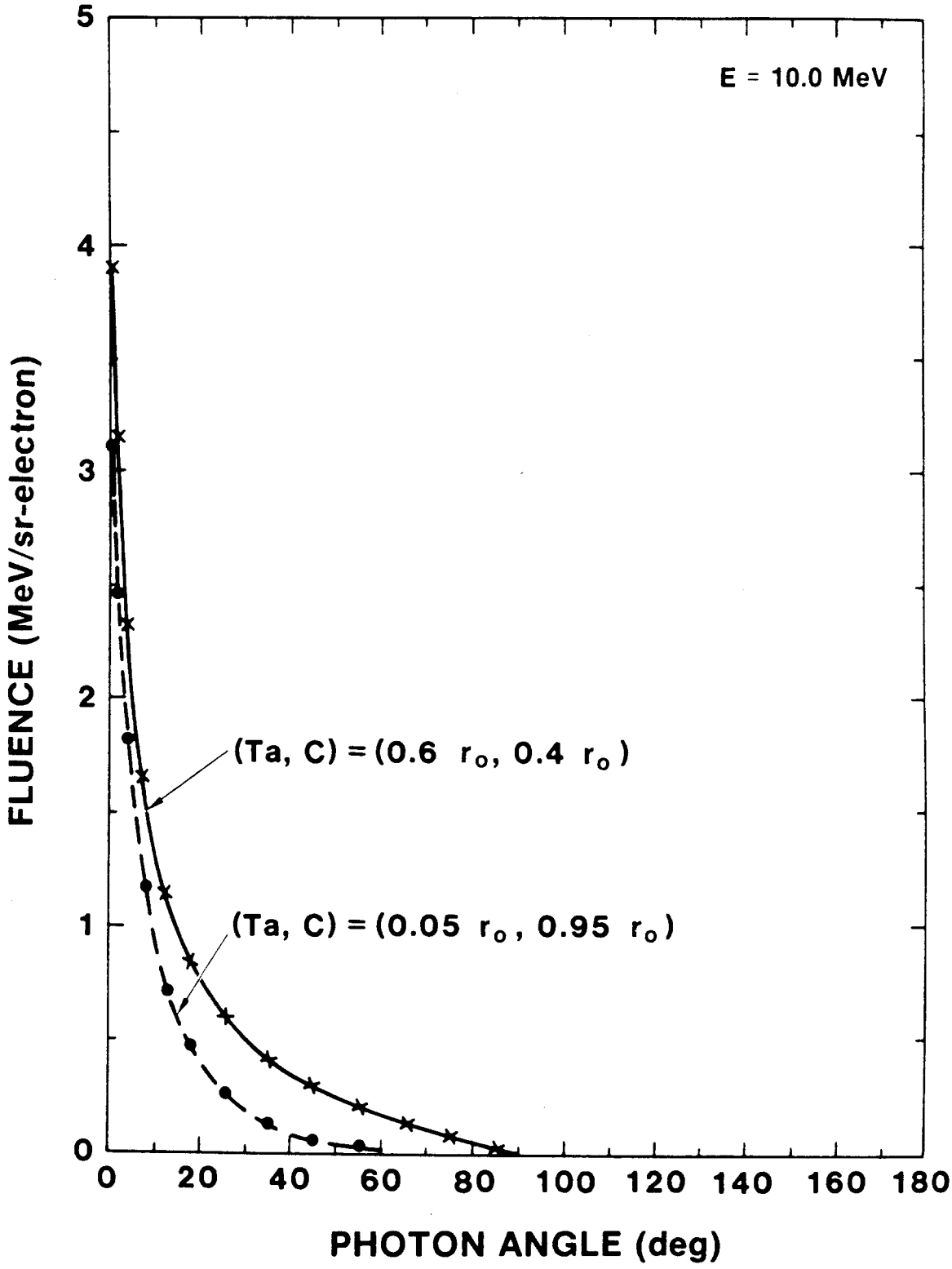

Figure 31. Energy Fluence as a Function of X-Ray Emission Angle for Two Converter Configurations and for 10.0 MeV Electrons – 0.17 in. Kevlar Debris Shield

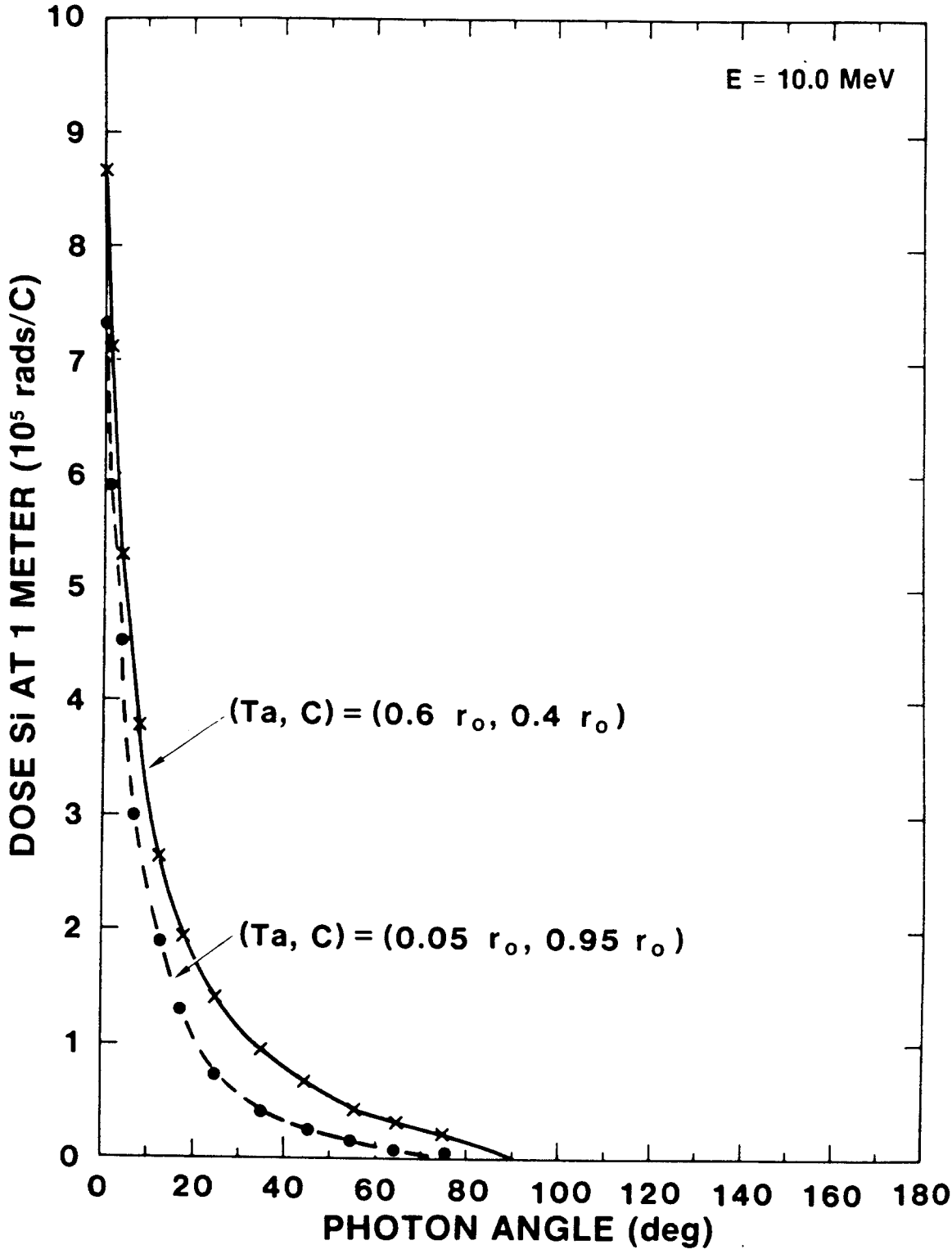

Figure 32. Dose-to-Silicon at a Distance of 1-Meter from the Converter as a Function of X-Ray Emission Angle for Two Converter Configurations and for 10.0 MeV Electrons – 0.17 in. Kevlar Debris Shield

6. Summary and Conclusions

Using a sophisticated Monte Carlo transport model, we have carried out systematic predictions of the radiation fields produced by three standard converter configurations at source-electron energies ranging from 0.5 to 15.0 MeV. Coupling the Monte Carlo model with a quasi-analytic dose estimator, we have also obtained systematic predictions of the energy deposition in materials commonly encountered in x-ray diagnostics and radiation effects experiments.

Our conclusions are summarized as follows:

Radiation Fields

(1) The maximum difference in the peak x-ray extraction efficiencies over the forward 2π solid angle for the three standard converter configurations, consisting of Ta converter foils with or without electron absorbers or debris shields, is about 20%.

(2) The thickness that maximizes the 2π efficiency increases from 0.3 to 0.5 or 0.6 times the CSDA range as the source kinetic energy increases from 0.5 to 15.0 MeV.

(3) The 2π efficiency is a slightly superlinear function of source-electron kinetic energy.

(4) At 0.5 MeV almost 10% of the 2π extracted x-ray energy is line radiation, whereas at 3.0 MeV the line radiation has decreased to less than 1%.

(5) Expressed as a percent of the source-electron kinetic energy, the average photon energy of the 2π extracted x rays decreases from just over 20% at 0.5 MeV to just over 10% at 15.0 MeV.

(6) The three primary effects that prevent the 2π forward extraction efficiency from approaching the radiation yield (production in an infinite medium of Ta) are (a) electron reflection, (b) photon reflection, and (c) photon absorption. Electron backscattering is an especially large loss mechanism at low source-electron kinetic energies.

(7) The x-ray spectra at small forward angles are softer than the 2π forward spectra at low electron energies because of the dominance of slant-thickness absorption of the relatively low-energy photons in the converter at the high emission angles. At high electron energies the small-angle spectra are harder than the 2π spectra because (1) the basic photon production cross section favors high energy forward production, and (2) slant-thickness absorption is less important for the higher energy photons.

(8) At high photon energies where self-absorption by the converter is unimportant, the spectra decrease monotonically with increasing photon energy, reflecting the approximate $(h\nu)^{-1}$ dependence of the photon production cross section.[2] At low photon energies the photoelectric interaction in the high-Z converter foil leads to a more complex energy dependence.

(9) The full width at half maximum of the x-ray angular distribution is a strongly decreasing function of the source-electron kinetic energy.

(10) There are significant differences in the average photon energy as a function of emission angle for the three standard converter configurations.

Radiation Dosimetry

(1) Dosimetry in four materials commonly encountered in effects or diagnostics experiments is characterized in terms of effective mass energy absorption coefficients, μ_{eff}.

(2) Above 5.0 MeV, μ_{eff} for gold approaches 0.04 cm^2/g, and that for Si, air, and CaF_2 (TLD) approaches 0.02 cm^2/g. The doses in silicon, air, and TLD are equivalent to one another to better than 10% for source electrons with energies in excess of 5.0 MeV.

(3) At a source energy of 1.0 MeV in Si, μ_{eff} is twice the value of the absorption coefficient at the average photon energy. Above a source energy of 3.0 MeV, where also the bulk of the photons generated are in an energy region where Compton scattering dominates over the photon-electric cross sections, the two coefficients agree to better than 10%.

(4) For a given fluence, μ_{eff} can be used to predict dose. The prediction of on-axis dose is in reasonable agreement with previous experimental results.

(5) In silicon, μ_{eff} remains relatively independent of emission angle up to the angle at which the photon fluence has decreased to half its zero-degree value. At larger angles, μ_{eff} decreases rapidly for low source-electron energies. In contrast to the silicon results, the gold coefficients increase with emission angle at small angles and especially at high energy.

(6) The μ_{eff} show a relatively strong dependence on the thickness of the tantalum converter foil at 1.0 MeV as compared with a relatively weak dependence at 10.0 MeV.

(7) By choosing a converter foil thickness that maximizes Si dose at low source-electron energies, the dose in Si can be increased by as much as 70% over that obtained from a foil thickness chosen to maximize x-ray fluence. The large difference between the thicknesses for maximizing fluence and dose at low source energies arises from the fact that photon absorption is a strongly decreasing function of photon energy for these low-energy spectra. At the higher source energies, dose and fluence are maximized by approximately the same tantalum thicknesses.

References

[1]J. A. Halbleib, *Parametric Study of Pulsed Electron Beam Environments*, SC-RR-72 0435 (Albuquerque, NM: Sandia National Laboratories, September, 1972).

[2]W. Heitler, *The Quantum Theory of Radiation*, Third Edition, Oxford University Press, 1954 p. 242.

[3]J. A. Halbleib and W. H. Vandevender, *Nucl. Sci. Eng.* 57, 94 (1975). J. A. Halbleib and T. A. Mehlhorn, *ITS: The Integrated TIGER Series of Coupled Electron/Photon Monte Carlo Transport Codes*, SAND84-0573 (Albuquerque, NM: Sandia National Laboratories, November, 1984).

[4]M. J. Berger and S. M. Seltzer, *Electron and Photon Transport Programs I., Introduction and Notes on Program DATAPAC 4*, NBS Report 9836 (U. S. Department of Commerce, National Bureau of Standards, June, 1968).

[5]J. H. Hubbell, *Photon Cross Sections, Attenuation Coefficients, and Energy Absorption Coefficients from 10 keV to 100 GeV*, Report NSRDS-NBS 29 (Washington, DC: U. S. National Bureau of Standards, August 1969), p. 9.

[6]A. L. Pregenzer and J. A. Halbleib, *IEEE Trans. Nucl. Sci. Vol. NS-32*, to be published.

[7]T. W. L. Sanford and J. A. Halbleib, *IEEE Trans. Nucl. Sci.*, Vol. NS-31, No. 6, 1095 (1984).

[8]J. A. Halbleib, G. J. Lockwood, and G. H. Miller, *IEEE Trans. Nucl. Sci.*, Vol. NS-23, No. 6, 1881 (1976).

[9]A. H. Wapstra, G. J. Nijgh, and R. Van Lieshout, *Nuclear Spectroscopy Tables*, (New York: International Publishers, Inc., 1959) p. 81.

[10]T. H. Martin, *Determination of Bremsstrahlung Production Efficiencies from Data Obtained on Phermex at 27 MeV*, SC-DR-69-240 (Albuquerque, NM: Sandia National Laboratories, May 1969).

[11]HWH/JCM, "Re-Evaluation of the Bremsstrahlung Production Efficiency for Optimum Targets," AWRE Internal Memo, August, 1982.

DISTRIBUTION:

DOE/TIC-4500, Rev. 74, UC-28 (102)

Anders Brahme
Dept. of Radiation Physics
Karolinska Institute
Fack
S-104 01 Stockholm
SWEDEN

Andree Dutreix
Institut Gustave Roussy
94 800 Villejuif
FRANCE

Dietrich Harder
Institut fur Medizinische Physik
und Biophysik
D 3400 Gottingen
Gosslerstr. 10
WEST GERMANY

Mr. & Mrs. Hanz Leetz
Institut t. Biophysik
Univ. Kliniken
D-6650 Homberg 3
WEST GERMANY

Andre Wambersie
Unite de Radiotherapie et de Neutrontherapie
Centre des Tumerus UCL 54.69
av. Hippocrate, 54
B. 1200 Bruxelles
BELGIUM

Office of the Secretary of Defense
Strategic Defense Initiatives Org.
Attn: Dr. G. Yonas, Chief Scientist
Washington, DC 20301

Fulmer Research Institute, Ltd.
Attn: A. Holmes-Siedle
Stoke Poges
Slough SL2 4QD
UNITED KINGDOM

University of Umea (2)
Radiation Physics Dept.
Attn: A. Nahum
H. Svensson
S-901 85 Umea
SWEDEN

The Ontario Cancer Institute
Attn: M. K. Woo
500 Sherbourne St
Toranto
CANADA M4X 1K9

Naval Surface Weapons Center (3)
Attn: M. Eha
O. Goktepe
D. Rule
Code R-41
Silver Spring, MD 20910

Thomas Jefferson University Hospital
Dept. Rad. Therapy and Nuclear Med.
Attn: K. Ayyangar
10th & Walnut St
Philadelphia, PA 19107

US Naval Research Laboratory
Attn: G. Herling
Code 6651
Washington, DC 20375

National Research Council of Canada
Division of Physics
Attn: D. W. O. Rogers
Ottawa
CANADA KIA OR6

Grumman Aerospace Corporation (2)
Attn: M. L. Rossi
M. Stauber
A01-026
Bethpage, NY 11714

Science Applications, Inc.
Attn: M. Merker
1200 Prospect Street
La Jolla, CA 92037

Orlando Technologies, Inc. (2)
Attn: J. Prentiss
D. Matuska
1651 University NE
Albuquerque, NM 87102

Air Force Weapons Laboratory (3)
Attn: J. F. Janni, DYC
J. Clifford
J. Mullis
Kirtland Air Force Base
Albuquerque, NM 87115

DISTRIBUTION: (Continued)

University of California
Lawrence Livermore National Laboratory (4)
Attn: E. F. Plechaty, L298
P. Meeker
H. Cabayan, L156
D. Fromme, L15
PO Box 808
Livermore, CA 94550

Science Applications, Inc. (6)
Attn: W. L. Chadsey
D. Frederick
R. Weitz
J. E. Tigner
A. A. Mondelli
D. Bacon
1651 Old Meadow Rd
McLean, VA 22101

Science Research Corp.
Attn: J. H. Jacob
1010 Memorial Drive
Cambridge, MA 02138

ARCON Corporation
Attn: S. Woolf
260 Bear Hill Rd
Waltham, MA 02154

California Institute of Technology
Space Radiation Laboratory
Attn: C. Chen
Pasadena, CA 91125

US Department of Commerce (4)
National Bureau of Standards
Attn: M. J. Berger
S. M. Seltzer
L. V. Spencer
G. Barnea, 533
Washington, DC 20234

Harry Diamond Laboratories (5)
Aurora Facility
Attn: J. Klebers
J. Agee
S. Graybill
K. Karas
D. Whittaker
2800 Powder Mill Rd
Adelphi, MD 20783

Los Alamos National Laboratory (5)
Attn: J. Mack
J. E. Morel
H. G. Hughes
M. Jain
H. H. Hsu
PO Box 1663
Los Alamos, NM 87544

Pulse Sciences, Inc. (4)
Attn: V. Bailey
S. Putnam
I. Smith
P. Spence
14796 Wicks Blvd.
San Leandro, CA 94577

SPIRE Corporation
Attn: R. Little
Patriots Park
Bedford, MA 01730

McDonnell Douglas (2)
Astronautics Company-East
Attn: G. W. Davis
R. L. Kloster
St. Louis, MO 63166

Lockheed Missiles & Spac. Co.
Attn: M. D. Castillo
Bldg. 253
3251 Hanover St
Palo Alto, CA 94304

Kaman Sciences Corp. (2)
Attn: T. Connolly
D. P. McLemore
PO Box 7463
Colorado Springs, CO 80933

Science Applications, Inc.
Attn: W. H. Scott, Jr.
PO Box 2351
1250 Prospect St
La Jolla, CA 92037

Mission Research Corporation
Attn: C. L. Longmire
735 State St
Santa Barbara, CA 93101

DISTRIBUTION: (Continued)

M. D. Anderson Hospital
Texas Medical Center
Physics Department
Attn: P. Almond
Houston, TX 77030

Berkeley Research Associates
Attn: N. R. Pereira
PO Box 852
Springfield, VA 22150

Air Force Cambridge Research Laboratory (4)
Attn: E. A. Burke
J. C. Garth
A. R. Frederickson
J. N. Bradford
L. G. Hanscom Field
Bedford, MA 01730

Experimental & Mathematical Physics Consultants
Attn: T. M. Jordan
PO Box 3191
Gaithersburg, MD 20878

EMA
Attn: E. Mann
1025 Hermosa SE
Albuquerque, NM 87106

NASA Langley Research Center
Attn: C. K. Chang, 160
Hampton, VA 23665

Titan Systems Inc. (2)
Attn: K. Billman
L. Buchanan
Suite 370
39510 Paseo Padre Pkwy.
Fremont, CA 94538

Boeing Aerospace Co. (2)
Attn: I. Arimura, M. S. 2R-00
A. Johnston
PO Box 3999
Seattle, WA 98124

0314 B. F. Johnson
Attn: Staff
0314 S. A. Dupree
1000 W. F. Brinkman
1200 J. P. VanDevender
1230 J. E. Powell
1231 T. P. Wright
Attn: Staff
1231 J. A. Halbleib (20)
1231 A. L. Pregenzer
1231 L. J. Lorence
1232 W. Beezhold
1232 G. T. Baldwin
1232 M. A. Hedemann
1232 J. R. Lee
1232 C. R. McClenahan
1232 T. W. L. Sanford (20)
1233 L. M. Choate
1234 J. Chang
Attn: Staff
1234 R. J. Leeper
1235 J. M. Hoffman
1240 K. R. Prestwich
1241 J. R. Freeman
Attn: Staff
1241 J. W. Poukey
1245 D. E. Hasti
1245 J. J. Ramirez
1248 M. T. Buttram
1260 D. L. Cook
1261 D. H. McDaniel
1263 J. N. Olsen
1263 J. E. Maenchen
1264 P. A. Miller
1264 L. P. Mix
1265 J. P. Quintenz
Attn: Staff
1265 T. A. Mehlhorn
1265 M. A. Sweeney
1270 R. B. Miller
1271 M. J. Clauser
Attn: Staff
1271 R. J. Lipinski
1272 C. A. Ekdahl
1272 P. D. Coleman
1272 M. G. Mazarakis

DISTRIBUTION: (Continued)

1273 M. K. Matzen
Attn: Staff
1500 W. Herrmann
1512 D. A. Benson
1522 E. D. Reedy, Jr.
1533 S. T. Montgomery
1600 R. G. Clem
1601 G. W. Kuswa
1601 M. M. Widner
1800 R. L. Schwoebel
2300 J. L. Wirth
2320 J. H. Renken
2321 J. J. Hohlfelder
2321 D. C. McKeon
2321 W. G. Perkins
Attn: Staff
2321 L. D. Posey
2322 G. J. Scrivner
Attn: Staff
2322 C. N. Vittitoe
6423 D. A. McArthur
6425 J. E. Kelly
6446 W. H. Buckalew
6446 F. J. Wyant
6452 D. W. Vehar
7110 J. D. Plimpton
7112 C. R. Mehl
Attn: Staff
7112 J. Harris
7112 T. J. Tanaka
8230 W. D. Wilson
8233 A. J. Webb
8341 A. J. Antolak
8348 K. W. Battleson
8024 M. A. Pound
3141 C. M. Ostrander (5)
3151 W. L. Garner (3)